Optical Emission Spectroscopy of Highly Charged Ions for a $Cf^{15+/17+}$ Ion Clock

Dissertation
zur Erlangung des akademischen Grades
doctor rerum naturalium
(Dr. rer. nat.)
im Fach Physik
Spezialisierung: Experimentalphysik
eingereicht an der Mathematisch-Naturwissenschaftlichen Fakultät
Humboldt-Universität zu Berlin

Eingereicht von

M.Sc. Lakshmi Priya Kozhiparambil Sajith

Präsidentin der Humboldt-Universität zu Berlin:
Prof. Dr. Julia von Blumenthal

Dekan der Mathematisch-Naturwissenschaftlichen Fakultät:
Prof. Dr. Emil List-Kratochvil

Gutachter:

1. Prof. Dr. Steven Worm
2. Prof. Dr. Markus Krutzik
3. Priv.-Doz. Dr. Wolfgang Quint

Tag der mündlichen Prüfung: 30.06.2026

Abstract: Optical Emission Spectroscopy of Highly Charged Ions for a $Cf^{15+/17+}$ Ion Clock

Searches for physics beyond the Standard Model can be pursued through high-precision measurements of atomic systems that are sensitive to variations in fundamental constants. In this thesis, highly charged ions (HCI) are investigated as promising candidates for optical clocks to probe new physics. Particular emphasis is placed on highly charged californium (Cf) ions, which exhibit transitions in the optical region arising from level crossings that are highly sensitive to variations in the fine-structure constant. To facilitate the investigation of these transitions, the Heidelberg electron beam ion trap (HD-EBIT) is described, followed by the development of a compact clock setup that integrates a miniature EBIT, ion extraction beam line, and Paul trap as a step toward precision spectroscopy and clock operation with HCIs. The design and implementation of a dedicated injection system for rare and radioactive elements in the HD-EBIT (such as Cf) is described, focusing on the technical challenges associated with the construction of the apparatus. As a proof-of-principle study for Cf, optical spectroscopy of highly charged nickel ions is carried out, motivated by the two optical clock transitions present in Ni^{12+}. The optical emission spectroscopy performed at the HD-EBIT provides essential benchmark data for wavelength determination of prospective clock transitions, thereby laying the foundation for subsequent precision spectroscopy experiments. The wavelength of the Ni^{12+} M1 transition is measured with a fractional uncertainty in the order of 10^{-7}. Atomic structure calculations of highly charged Cf and Ni ions are presented. The experimental nickel results agree with the calculations, confirming the reliability of the theoretical method for line identification and supporting its application to californium spectroscopy.

Zusammenfassung: Optische Emissionsspektroskopie hochgeladener Ionen für eine $Cf^{15+/17+}$-Ionen-Uhr

Die Suche nach Physik jenseits des Standardmodells kann durch hochpräzise Messungen von atomaren Systemen erfolgen, die empfindlich auf Schwankungen der Fundamentalkonstanten reagieren. In dieser Dissertation werden hochgeladene Ionen (Highly Charged Ions, HCIs) als vielversprechende Kandidaten für optische Uhren zur Entdeckung neuer physikalischer Effekte untersucht. Ein besonderer Schwerpunkt liegt auf hochgeladenen Californium-Ionen (Cf), die aufgrund von Level-crossings Übergänge im optischen Spektralbereich aufweisen, die eine hohe Sensitivität gegenüber Variationen der Feinstrukturkonstanten besitzen. Zur Untersuchung dieser Übergänge wird zunächst die Heidelberger Elektronenstrahl-Ionenfalle (HD-EBIT) beschrieben, gefolgt von der Entwicklung eines kompakten Uhrenaufbaus, der eine Miniatur-EBIT, eine Ionenextraktionsstrahllinie und eine Paulfalle integriert, als Schritt hin zur Präzisionsspektroskopie und zum Uhrenbetrieb mit HCIs. Das Design und die Umsetzung eines speziellen Injektionssystems für seltene und radioaktive Elemente wie Cf in der HD-EBIT wird beschrieben, wobei der Schwerpunkt auf den technischen Herausforderungen liegt, die mit dem Aufbau der Apparatur verbunden sind. Als Proof-of-Principle-Studie für Cf wird die optische Spektroskopie hochgeladener Nickel-Ionen durchgeführt, motiviert durch die zwei optischen Uhrenübergänge in Ni^{12+}. Die am HD-EBIT durchgeführte optische Emissionsspektroskopie stellt wesentliche Referenzdaten für die Wellenlängenbestimmung potenzieller Uhrübergänge bereit und bildet somit die Grundlage für weiterführende Experimente zur Präzisionsspektroskopie. Die Wellenlänge des Ni^{12+}-M1-Übergangs wird mit einer relativen Unsicherheit in der Größenordnung von 10^{-7} gemessen. Die Atomstrukturrechnungen für hochgeladene Cf- und Ni-Ionen werden präsentiert. Die experimentellen Nickelergebnisse stimmen mit den Berechnungen überein, was die Zuverlässigkeit der theoretischen Methode zur Linienidentifikation bestätigt und ihre Anwendung auf die Californium-Spektroskopie unterstützt.

Contents

Acronyms

BESSY Berliner Elektronenspeicherring-Gesellschaft für Synchrotronstrahlung

CCD charge-coupled device

CI Configuration Interaction

DESY Deutsches Elektronen-Synchrotron

DoD Drop on Demand

DTs drift tubes

E1 electric dipole

E2 electric quadrupole

EBIS electron beam ion source

EBIT electron beam ion trap

EII electron impact ionization

EUV extreme ultra violet

FAC Flexible Atomic Code

GFK Glasfaserverstärkter Kunststoff

HC-EBIT Heidelberg Compact EBIT

HCIs Highly charged ions

HD-EBIT Heidelberg EBIT

M1 magnetic dipole

MBPT Many-Body Perturbation Theory

MPIK Max Planck Institute for Nuclear Physics

MCPs microchannel plates

NIST National Institute of Standards and Technology

PDTs pulsed drift tubes

PEEK polyether ether ketone

PT Paul trap

PTB Physikalisch-Technische Bundesanstalt

RR radiative recombination

SM Standard Model

VUV vacuum ultraviolet

List of Figures

List of Tables

1 Introduction

A precise understanding of the fundamental particles and interactions described by the Standard Model (SM) of particle physics is essential for advancing our knowledge of the universe. In addition, highly sensitive probes are needed to test the predictions of the Standard Model and to detect any possible deviations from it. While the Standard Model has proven remarkably successful, it leaves several key questions unresolved including the nature of dark matter and dark energy, origin of matter-antimatter asymmetry and neutrino mass. Addressing these open question demands not only theoretical exploration beyond the Standard Model but also experimental techniques with extraordinary levels of accuracy.

Measurements of atomic transition frequencies at very high precision allow sensitive tests of fundamental physics and effects beyond Standard Model [1]. Comparisons of very stable frequencies in different atomic systems can be used to probe possible variations of fundamental constants, such as the fine-structure constant [2]. Highly charged ions (HCIs) are especially promising for these studies. In HCIs, the large nuclear charge leads to tightly bound electrons so that relativistic effects play a dominant role in determining the atomic energy levels. As a result, certain transitions in HCIs show an enhanced sensitivity to variations of fundamental constants, while at the same time being less sensitive to external perturbations [3]. This makes HCIs attractive candidates for future optical clocks and for laboratory searches for new physics [4, 5]. Experiments with HCIs require advanced methods for ion production, trapping, and spectroscopy as well as accurate theoretical calculations of atomic structure and transition properties.

This thesis contributes to the development of HCI-based precision measurements by combining theoretical atomic structure calculations with experimental work on electron beam ion traps and optical spectroscopy. Chapter 1 of the thesis introduces the Standard Model and its limitations, motivates searches for variations of fine-structure constant and dark matter using atomic clocks, and discusses the role of HCIs and clock networks. The relevant atomic physics considerations, including scaling laws in HCIs, transition probabilities, Zeeman effects and level crossings in californium, are presented in Chapter 2 together with a brief description of numerical methods for atomic struc-

ture calculations.

The experimental infrastructure relevant in this work is described in Chapters 3-5. Chapter 3 details the Heidelberg electron beam ion trap and the optical spectroscopy setup used to observe and characterize trapped ions while Chapter 4 introduces the miniature electron beam ion trap, beam line and Paul trap for clock-related applications. Chapter 5 focuses on the development of an injection system for rare, radioactive elements, including the implementation of a californium target and a laser-desorption setup. Chapter 6 presents atomic structure and transition calculations for highly charged nickel and californium ions using different computational approaches and compares their predictions. Chapter 7 reports on optical spectroscopy measurements of highly charged nickel ions, including data analysis procedures, calibration methods, and a comparison between measured and calculated transition energies. The thesis concludes in Chapter 8 with a summary of the main results and an outlook on future developments toward highly charged Cf ion clocks.

1.1 Standard Model and Beyond

The Standard Model is the most successful theory to date for describing elementary particles and three of the four fundamental forces. The SM is based on the gauge symmetry group $SU(3)_{\mathrm{c}} \times SU(2)_{\mathrm{L}} \times U(1)_{\mathrm{Y}}$, which accounts for the strong, weak, and electromagnetic forces, respectively. Matter particles (fermions) include quarks and leptons, while interaction-mediating particles (bosons) include the photon, gluons, and the W and Z bosons. Figure 1.1.1 shows the elementary particles that make up the Standard Model. The SM has been tested to high precision but remains incomplete [6, 7].

Key open questions in physics beyond the Standard Model fall into three categories: the origin of mass (e.g., the role of Higgs Boson and the question of why particle masses are small), unification (whether all forces can be described within a Grand Unified Theory), and flavour (why multiple generations of quarks and leptons exist and mix as they do). These challenges have motivated the development of various theoretical frameworks that go beyond the Standard Model. One prominent example is supersymmetry, which proposes a symmetry between fermions and bosons and offers solutions to several of these puzzles [9]. Supersymmetry often appears in more ambitious frameworks such as Theory of Everything that seeks to incorporate gravity into a quantum framework, unify it with the other fundamental interactions, and explain the structure of space-time [10].

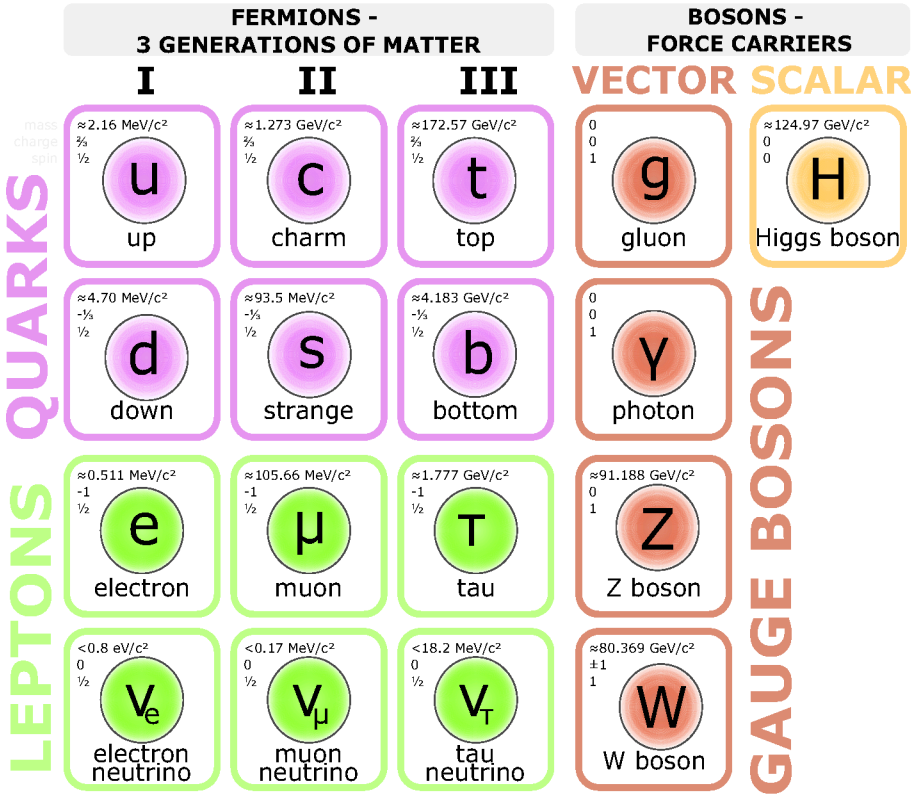

Figure 1.1.1: The Standard Model of particles. Figure adapted from [8].

Some approaches to physics beyond the Standard Model predict that fundamental constants such as the fine-structure constant, the speed of light, or Newton's gravitational constant, may not be truly constant. These models propose that such constants could vary over time or space, potentially as a result of coupling to new scalar fields or dynamics in higher dimensional theories. In unified models, different fundamental constants are linked, so their variations would be correlated [11]. Investigating the variation of fundamental constants opens a window into physics beyond the Standard Model and may provide empirical clues toward a deeper understanding of the underlying laws of nature [12].

1.2 Variation in Fine-structure Constant and Dark Matter

The fine-structure constant, commonly denoted by α, is a dimensionless physical constant that characterizes the strength of the electromagnetic interaction between ele-

mentary charged particles. It is defined as

$$\alpha = \frac{e^2}{4\pi\varepsilon_0\hbar c} \approx \frac{1}{137} \tag{1.1}$$

This expression combines several fundamental constants: the elementary charge e, Planck's reduced constant $\hbar$, the vacuum permittivity ε_0, and the speed of light c, making α a cornerstone of quantum electrodynamics (QED) and one of the most important constants in physics [13]. Historically, α was introduced by Sommerfeld (1916) [14] in his extension of Bohr's model to explain the fine-structure observed in hydrogen atomic spectra. Today, it is known to govern a wide range of electromagnetic processes, including atomic energy levels, transition rates, and scattering amplitudes. Because it is dimensionless, its numerical value is independent of the unit system, making it particularly useful for probing fundamental physics across different regimes.

Precision measurements of α come from a variety of sources, such as the anomalous magnetic moment of the electron, atomic recoil experiments, and the quantum Hall effect [15–17]. The current best estimate based on atom-recoil measurements using matter-wave interferometry yields

$$\alpha^{-1} = 137.035999084(21)$$

with an uncertainty on the order of one part in 10^{10} [13].

Early theoretical work, such as the model proposed by Bekenstein, introduced the idea that the fine-structure constant α could vary dynamically [18]. More recent models have explored how such variation could arise from scalar fields that also play a role in dark matter physics [19]. Dark matter is a non-luminous component of the universe that reveals itself only through its gravitational influence. It constitutes about 27% of the universe's energy budget, as inferred from observations such as galaxy rotation curves, gravitational lensing, and cosmic microwave background anisotropies [20].

While the nature of dark matter remains unknown, a variety of theoretical models have been proposed, including weakly interacting massive particles (WIMPs), axions, and ultralight scalar fields. Among these, scalar field dark matter is particularly compelling in the context of fundamental constant variation, as such fields can naturally couple to Standard Model particles, and induce oscillations or drifts in constants like α [21, 22].

The relevant sector of the Standard Model Lagrangian is given by [21]:

$$\mathcal{L}_{\mathrm{SM}} = -\sum_f m_f \overline{f} f \; - \frac{F_{\mu\nu}F^{\mu\nu}}{4} + \sum_V \frac{M_V^2}{2} V_\nu V^\nu \tag{1.2}$$

The indices f and V denote SM fermions and massive vector bosons, respectively, while m_f and M_V are their corresponding masses. The terms involving $F_{\mu\nu}$ and V^ν represent couplings to the electromagnetic field and weak vector bosons. A non-relativistic, scalar field ϕ, which may constitute dark matter, can interact with Standard Model fields via linear couplings. Following Damour-Donoghue [23] and Arnavitaki et. al. [24], the effective interaction Lagrangian where ϕ interacts linearly with the electromagnetic term can be expressed as:

$$\mathcal{L}_{int} = \kappa\phi\frac{d_e}{4e^2}F_{\mu\nu}F^{\mu\nu} \tag{1.3}$$

where κ is the gravitational coupling, d_e is a dimensionless coefficient that parametrizes the strength of the linear coupling of ϕ to the electromagnetic field, and the scalar field ϕ is defined as:

$$\phi = \phi_0 cos(\omega t)$$

where ϕ_0 is the amplitude of the ultra light dark matter and the frequency of the oscillating field ω is given by,

$$\omega = \frac{m_\phi c^2}{\hbar}$$

Combining the $\mathcal{L}_{\text{int}}$ (Equation 1.3) with the Standard Model Lagrangian (Equation 1.2) illustrates how the scalar field modifies effective electromagnetic coupling. The modified electromagnetic field in the combined Lagrangian is [23]:

$$\begin{aligned}\mathcal{L}_{\text{EM}} &= -\frac{1 - d_e\kappa\phi}{4e^2}F_{\mu\nu}F^{\mu\nu} \\ &\simeq -\frac{1}{4(1 + d_e\kappa\phi)e^2}F_{\mu\nu}F^{\mu\nu}\end{aligned} \tag{1.4}$$

Since the fine-structure constant is defined as $\alpha = e^2/4\pi$, this coupling leads to an effective, time-varying fine-structure constant [23]:

$$\alpha_{eff} = (1 + d_e\kappa\phi)\alpha \tag{1.5}$$

Equation 1.5 indicates that the coupling of an oscillating dark matter field $\phi = \phi_0 cos(\omega t)$ to the electromagnetic sector results in temporal oscillations of the fine-structure constant α.

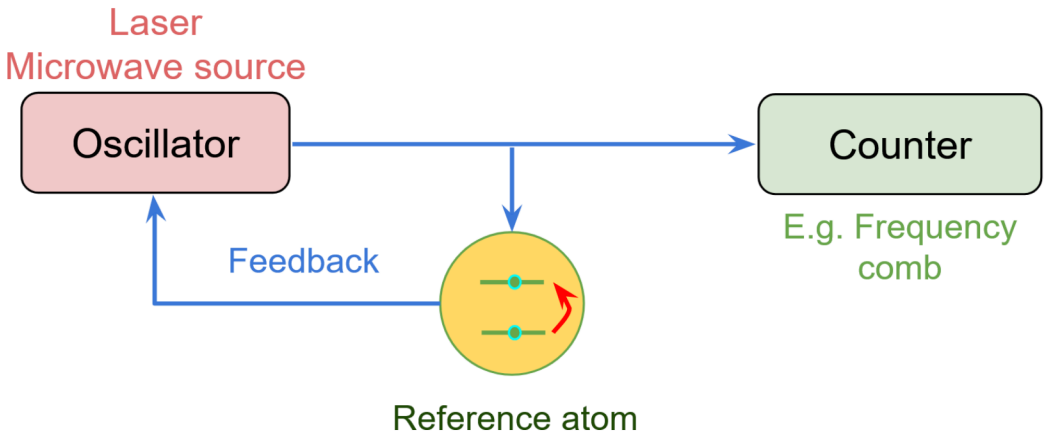

Figure 1.3.1: Diagram showing a local oscillator locked to an atomic transition via a feedback loop. The stabilized oscillator frequency is measured using a counter (e.g. a frequency comb). Modified from [29].

1.3 Astrophysical Observation to Laboratory Measurements

Quasar absorption lines arise when light from distant quasars (extremely luminous active galactic nuclei) passes through interstellar or intergalactic gas clouds which absorb specific wavelengths along the line of sight. Observation of these absorption systems with high-resolution spectrographs such as Keck/HIRES and VLT/UVES, allow researchers to examine the value of α in the distant past [25]. Techniques like the many-multiplet method have revealed tentative evidence for both temporal and spatial variations in α [26, 27]. These results, however, remain contentious due to several systematic uncertainties, including instrumental calibration errors, unknown isotopic abundances that affect line positions, and overlapping absorption features (like line blending) [28].

While astrophysical observations provide insight into possible variation of α over cosmological timescales and distances, they are subject to significant systematic uncertainties and model assumptions. To complement these approaches, laboratory-based measurements, especially those using atomic clocks, offer an extremely precise and controlled method to test for any present-day temporal drift in the fine-structure constant [1].

Atomic clocks operate by locking a laser to the frequency of a specific electronic transition in an atom or ion [30]. The frequency of such transitions is governed by quantum electrodynamics and depends on the value of α, especially in systems with large nuclear charge such as heavy HCIs, where relativistic corrections are significant. By compar-

ing the ticking rates of two clocks based on different atomic species, each with distinct α-dependencies, researchers can detect or constrain tiny drifts in α over time.

A good optical clock transition must fulfill several essential requirements [30]. It should possess narrow linewidth, typically provided by a long-lived or forbidden transition, in order to enable high spectral resolution and long interrogation times. The transition should lie in the optical frequency range, where precise and stable laser sources are available, and it must be sufficiently insensitive to external perturbations so that systematic shifts can be well controlled. These properties together enable a high quality factor and excellent frequency stability. For tests of fundamental physics, additional considerations apply: transitions with a strong dependence on the fine-structure constant α, characterized by a large sensitivity coefficient K, are particularly valuable, as they enhance the ability of optical clocks to probe potential variations of fundamental constants.

The sensitivity coefficient K is obtained from atomic structure calculations that determine how an energy level changes when the value of α is varied [5]. The energy level dependence on α is written as

$$E(\alpha) = E_0 + q\left[\left(\frac{\alpha}{\alpha_0}\right)^2 - 1\right] \tag{1.6}$$

where the parameter q is determined numerically from

$$q = \frac{E(+\delta) - E(-\delta)}{2\delta}. \tag{1.7}$$

This relates changes in the transition frequency to changes in α through

$$\frac{\delta\nu}{\nu} = \frac{2q}{E_0}\frac{\delta\alpha}{\alpha} \equiv K\frac{\delta\alpha}{\alpha}, \tag{1.8}$$

so that the dimensionless sensitivity coefficient is

$$K = \frac{2q}{\nu} \tag{1.9}$$

where q is a parameter that has the dimension of energy [31].

Experimental measurements of the stability between two optical clock frequencies are described by

$$\frac{\Delta(\nu_2/\nu_1)}{(\nu_2/\nu_1)} = (K_2 - K_1)\frac{\Delta\alpha}{\alpha} \tag{1.10}$$

where K_1 and K_2 are the sensitivity coefficients of clock 1 and 2, respectively. Different atomic clock species exhibit different sensitivity coefficients (K) to variations in the

Clock system	Wavelength	K
Sr	698 nm	0.06
Yb^+	467 nm	−5.95
Yb^+	578 nm	0.31
Ca^+	729 nm	0.15
Ni^{12+}	498 nm	1.49
Ar^{13+}	441 nm	1.95
Ir^{17+}	1978 nm	145
Ir^{17+}	283 nm	−21.84
Pr^{9+}	494 nm	4.23
Nd^{9+}	485 nm	6.52
Cf^{15+}	618 nm	59
Cf^{17+}	485 nm	−48

Table 1.3.1: Clock transitions in various atomic and highly charged ion systems, along with their corresponding wavelengths and sensitivity coefficients (K) to variations in the fine-structure constant α. The K value quantifies how strongly a given clock transition would shift in response to a potential variation in α (see Eq. 1.8), making certain systems, particularly highly charged ions like Cf^{15+} and Cf^{17+}, promising candidates for fundamental physics tests. Data are compiled from both theoretical calculations and experimental measurements [3, 32–35].

fine-structure constant α making some clocks particularly valuable for probing potential drifts. Since the parameter K quantifies how strongly a clock's transition frequency depends on α, comparisons between clocks with large differences in K ($|K_1 - K_2|$) enhance the sensitivity to temporal or spatial variation. Table 1.3.1 lists representative K values for various atomic clock transitions across different species.

A landmark experimental result was reported by Rosenband et al. (2008) [36], who compared Al^+ and Hg^+ ion optical clocks, which are two systems with significantly different sensitivities to α. Their comparison yielded a model-independent constraint on the present-day drift of the fine-structure constant:

$$\frac{1}{\alpha}\frac{d\alpha}{\alpha} = (-1.6 \pm 2.3) \times 10^{-17}\ \text{yr}^{-1} \tag{1.11}$$

This result stood for over a decade as the most stringent experimental limit on variation in α.

More recently, Filzinger et al. (2023) [37] reinterpreted atomic clock data in the context of scalar field dark matter models that allow for couplings between dark matter and photons. In such models, the scalar field can induce slow temporal variations or

oscillations in fundamental constants. By translating clock stability measurements into bounds on the photon coupling strength, they derived a model-dependent constraint on the present-day variation in α:

$$\frac{1}{\alpha}\frac{d\alpha}{dt} = (1.8 \pm 2.5) \times 10^{-19}\ \mathrm{yr}^{-1}$$

In recent years, several atomic clocks have achieved exceptional fractional frequency accuracy, reaching levels as low as 10^{-18} and even approaching 10^{-19} [38–41]. These advances not only allow tighter constraints on the possible temporal drift of the fine-structure constant α but also open powerful new avenues for testing physics beyond the Standard Model. In particular, atomic clocks are being used to search for couplings to ultralight dark matter fields, which could induce transient or oscillatory variations in fundamental constants. Their extreme precision has enabled applications beyond fundamental physics including relativistic geodesy, atomic timekeeping, satellite-based navigation, and the development of global clock networks for gravitational wave detection [5, 42–44].

1.3.1 Highly Charged Ions

Highly charged ions (HCIs) are ions formed when atoms lose many of their electrons, resulting in positively charged species with only a few remaining electrons. These ions retain the same atomic nucleus but exhibit significantly different atomic properties from those of neutral atoms due to the strong Coulomb field produced by the high charge state. HCIs are found abundantly in extreme astrophysical environments such as stellar coronae, active galactic nuclei, and supernova remnants, where high temperatures and intense radiation fields strip atoms of many of their electrons. Earlier measurements of HCIs were first identified through the observation of optical emission lines in the solar corona [45]. The prevalence of HCIs in these hot, ionized regions makes them essential for interpreting a wide range of astronomical observations and for probing the underlying physical processes in these environments [46]. HCIs are also valuable tools for diagnosing conditions in fusion and laboratory plasmas [47, 48], testing quantum electrodynamics under extreme electromagnetic fields [49–51], and investigating potential signatures of new physics beyond the Standard Model [5].

HCIs present compelling advantages for next-generation atomic clocks and fundamental physics tests. One of their key strengths lies in their significantly reduced sensitivity to external perturbations, such as blackbody radiation shifts and electric field gradients, compared to neutral atoms or singly charged ions [35]. Theoretical studies have shown

that some HCI transitions can exhibit fractional systematic uncertainties at the level of $< 10^{-19}$, making them highly promising candidates for ultra-precise timekeeping [4].

Despite their highly ionized nature, several HCI species possess transitions in the optical frequency range [52, 53]. This primarily arises from level crossings and configuration reordering that occur along isoelectronic sequences as the charge state increases, bringing certain electronic transitions from ultraviolet or x-ray domain into the optical range. These transitions are experimentally accessible through direct optical laser interrogation and simultaneously exhibit pronounced sensitivity to variations in the fine-structure constant. This sensitivity arises because the two levels forming the transition generally experience different relativistic energy shifts, which scale approximately with $(Z_{\text{eff}}\alpha^2)$ (see Section 2.1.3) [54]. For instance, the clock transition in californium ion Cf^{15+} and Cf^{17+} exhibit a significantly larger K compared to conventional neutral atoms or singly charged ions as shown in Table 1.3.1. The high sensitivity towards α make the HCIs valuable for detecting oscillations or sudden jumps in α caused by topological defects [55]. Additionally, they can be used to probe potential cosmological evolution associated with dark matter [21].

While highly charged ions are naturally abundant in extreme astrophysical environments, reproducing and controlling them on Earth poses significant experimental challenges due to the high energies required to strip so many electrons. Advances in ion-trapping techniques, such as the electron beam ion trap (EBIT) [56] and electron cyclotron resonance (ECR) ion sources [57], have made it possible to generate and confine HCIs under laboratory conditions with high precision and stability, enabling detailed studies of their properties under controlled conditions. EBITs have enabled the precise spectroscopic measurement of HCIs across a broad range of wavelengths, extending from the optical [58] to the extreme ultra violet (EUV) [59] and even soft x-ray regions [60–62].

Although EBITs are highly effective for generating and spectroscopically probing HCIs, the typical plasma temperatures within these traps are on the order of several million kelvin, which pose significant limitations for high-precision measurements due to Doppler broadening and collisional effects. To overcome these constraints, HCIs are typically extracted from the EBIT and subsequently transferred to colder, high-precision trapping environments, such as Penning traps or radio-frequency (Paul) traps. A brief overview of the ion extraction and trapping process is provided in Chapter 4. A pioneering demonstration of this method was achieved by Schneider et al. (1994) [63], who successfully recaptured Xe^{44+} and $Th^{68+,72+}$ ions from an EBIT into a cryogenic Penning trap. Building on this, a significant advancement was made by Schmöger et

al. (2015) [64], who demonstrated the first re-trapping of an HCI, specifically Ar^{13+} into a cryogenic linear Paul trap. There, the ion was embedded in a laser-cooled Be^{+} Coulomb crystal, enabling sympathetic cooling. These systems enable significantly improved control over the ions' motional and internal states, facilitating high-resolution spectroscopy and clock applications.

1.3.2 HCI Clock Candidates

In this thesis, two elements, nickel (Ni) and californium (Cf), are investigated, with a particular focus on the highly charged ion clock candidates Ni^{12+}, Cf^{15+} and Cf^{17+}. As part of this work, Ni^{12+} was experimentally measured, along with other charge states, serving as a proof-of-principle for future measurements involving californium. The spectroscopy of highly charged californium ions presents substantial technical challenges, requiring the development of dedicated experimental techniques and infrastructure. While a full measurement campaign on californium has not yet been carried out, the results and developments presented here provide the foundation for experiments that are planned as part of future research.

Nickel

Nickel (Ni), with an atomic number of 28, is a silvery-white transition metal. Nickel was used unknowingly in ancient alloys as early as 3500 BCE. It was officially identified in 1751 by Swedish chemist Axel Fredrik Cronstedt, who isolated it from an ore once called Kupfernickel "devil's copper" by German miners [65]. The most abundant isotope of Ni is ^{58}Ni.

Nickel is commonly found in many astrophysical environments [67], which makes it a useful element for comparing data from astronomical observations with results from atomic clock experiments. Such comparisons can help explore whether the fine-structure constant has changed over time [68].

Ni^{12+} has 16 electrons and is a promising highly charged ion for optical clock development due to its narrow forbidden transitions in the visible range. The ground state configuration of Ni^{12+} is $1s^2 2s^2 2p^6 3s^2 3p^4$. It features two forbidden clock transitions in the optical range: $3s^2 3p^4\ {}^3P_2 \rightarrow 3s^2 3p^4\ {}^3P_1$ a magnetic dipole (M1) line at 511 nm and $3s^2 3p^4\ {}^3P_2 \rightarrow 3s^2 3p^4\ {}^3P_0$ an electric quadrupole (E2) line at 498 nm, see figure 1.3.2. The M1 transition is also usable for state detection in quantum logic spectroscopy (QLS), thus that transition is highly desirable to be detected [66].

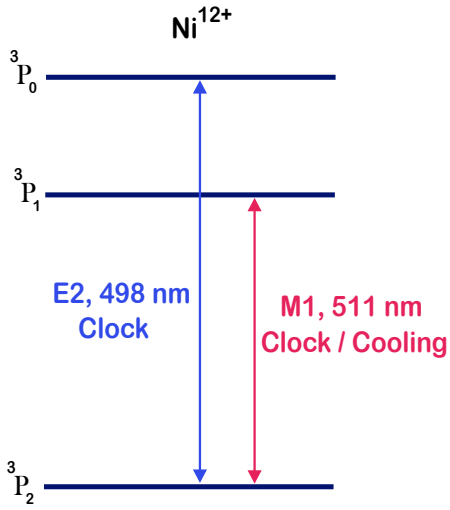

Figure 1.3.2: The two clock transitions in Ni^{12+} at 498 nm and 511 nm are shown here. Adapted from [66].

Californium

Californium is a radioactive, silvery-white transuranium element in the actinide series with atomic number 98. It was first discovered in 1950 by Thompson, Street Jr., Ghiorso, and Seaborg through the bombardment of curium with helium ions [69]. The isotope produced during this initial synthesis was californium-244 (^{244}Cf) which has a half-life of around 45 minutes and decays primarily by alpha emission with an energy of 7.1 MeV [70]. Some of the isotopes of californium are listed in Table 1.3.2. A detailed study of how the isotopes of Cf were produced can be found in [71].

From Table 1.3.2, californium possesses a number of isotopes with widely differing half-lives and decay properties. For the planned spectroscopy experiment, the isotope of primary interest is ^{249}Cf. This isotope is particularly well suited because it combines a long-life of 351 years with the practical advantage that it can be obtained in isotopically pure form which is essential for precision measurements as it avoids complication from isotope shifts.

As seen in Table 1.3.1, the sensitivity coefficients K of Cf^{15+} and Cf^{17+} to variations in the fine-structure constant α are exceptionally high, making them promising candidates for next-generation optical atomic clocks and fundamental physics experiments. This heightened sensitivity is primarily due to the occurrence of a level crossing between the $6f$ and $5f$ orbitals, which enhances relativistic effects and leads to a stronger dependence of the clock transition frequencies on α (see Section 2.2). In Cf^{17+}, the relevant clock transition occurs between the low-lying states $5d^{10}\ 6s^2\ \ 6p_{1/2}$ to $5d^{10}\ 6s^2\ \ 5f_{5/2}$

Isotope	half-life	Primary decay mode
^{248}Cf	334 d	α
^{249}Cf	351 yr	α
^{250}Cf	13.0 yr	α
^{251}Cf	898 yr	α
^{252}Cf	2.6 yr	α
^{253}Cf	17.8 d	β
^{254}Cf	60.5 d	Spontaneous fission

Table 1.3.2: Overview of selected californium isotopes, including their half-lives and primary decay modes [72]. The isotopes listed vary significantly in stability, with half-lives ranging from several days to nearly nine centuries. Most californium isotopes decay via alpha emission, although some, such as ^{254}Cf, undergo spontaneous fission, and ^{253}Cf primarily decays through beta emission.

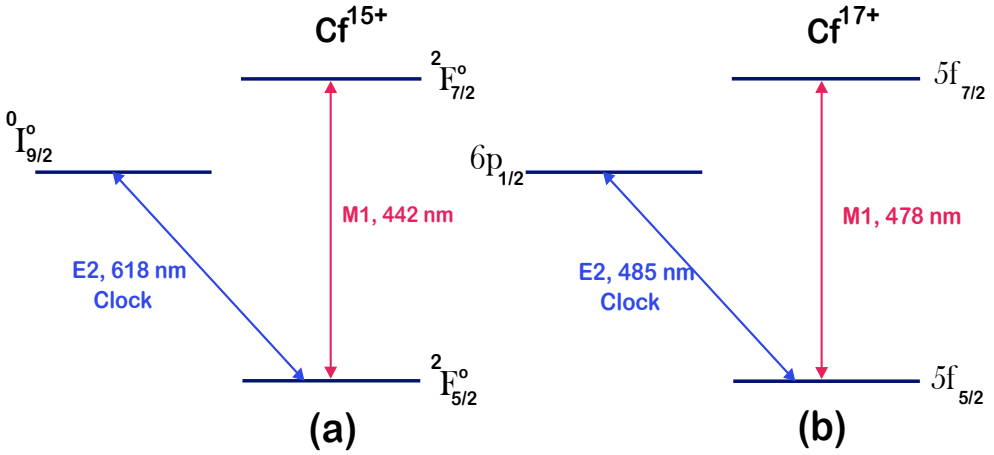

Figure 1.3.3: Clock transitions in (a) Cf^{15+} at 618 nm and (b) Cf^{17+} at 485 nm, showing the level crossings between the $6p$ and $5f$ orbitals. The transition wavelengths are theoretical predictions taken directly from the calculations presented in [73]. Figure adapted from [73].

with a transition wavelength of 485 nm. For Cf^{15+}, the clock transition takes place between the states $5d^{10}\ 5f\ 6p^2\ \ ^2F_{5/2}$ to $5d^{10}\ 5f^2\ 6p\ \ ^4I_{9/2}$, corresponding to a wavelength of 618 nm (see figure 1.3.3).

1.4 Clock Networks

The elusive nature of dark matter has motivated scientists to develop highly accurate and stable atomic clocks to detect possible interactions between scalar dark matter fields and Standard Model fields. While individual clocks can provide sensitive tests, building a network of clocks significantly enhances the detection capabilities. Such networks improve sensitivity to potential variations in fundamental constants, such as the fine-structure constant, in various forms, including drifts (slow temporal changes) [74], transients (sudden, temporary shifts) [75], and oscillations (periodic fluctuations) [76].

Modern optical clocks are far more precise than conventional time-distribution methods [77]. Techniques such as GPS signals or microwave links are sufficient for everyday timekeeping, but they do not provide the stability and accuracy required to compare state-of-the-art optical clocks. To compare optical clock at their full precision they must therefore be connected directly, which can be achieved by transmitting a stable optical signal through fiber optics cables. Frequency combs at each clock site compare the local clock frequency to this shared optical signal, removing dependence on the exact frequency of the transfer laser. Environmental disturbances in the fiber cause phase noise, which is actively corrected in real time by analyzing reflected light using an interferometer [78]. To preserve the signal's stability, specialized unused fiber lines (dark fibers) with bi-directional optical amplifiers are used, enabling frequency transfer with precision limited only by the clocks themselves, even across distances of thousands of kilometers [79].

Clock networks enable the validation of simultaneous measurements across multiple clock pairs, enhancing the reliability of correlated timing data. They can provide critical insights into the directionality and speed of oscillating dark matter fields, assuming such fields interact with atomic clocks [80]. Furthermore, clock networks are effective in distinguishing true signals from environmental noise, such as magnetic interference caused by solar wind, thereby improving the accuracy in identifying the origin of potential signals [81]. The realization of a global quantum clock network could enable the construction of a unified, real-time international time scale with unprecedented accuracy and long-term stability, surpassing current standards and advancing a wide

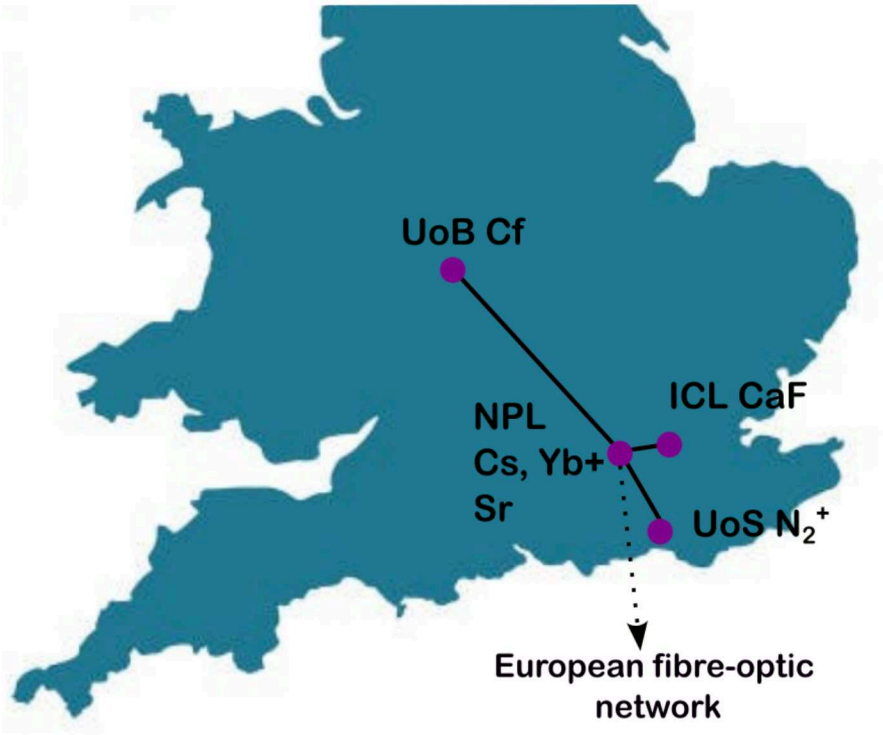

Figure 1.4.1: The QSNET network. Adapted from [33]. The map illustrates the locations of all clocks along with the elements under investigation that will be part of QSNET.

range of scientific and technological applications [82].

Optical clock networks are important not only for precise timekeeping, but also for studying fundamental physics. Tests for variations of fundamental constants require comparisons between clocks with different sensitivities, described by their sensitivity coefficients K (see Section 1.3) [83]. Comparing two identical clocks gives little useful information, because they react in the same way. In contrast, comparing different types of clocks such as neutral atoms and highly charged ions makes it possible to detect differences in how they respond to changes in fundamental constants. A network that includes a variety of clocks with different K values therefore makes it possible to search for new physics in ways that a single type of clock cannot.

Several clock network initiatives have already been developed within the international metrology community, primarily aimed at time and frequency transfer, relativistic geodesy and the realization of improved global time scales [84, 85]. In addition to their metrological goals, such networks are sensitive to new physics and provide important proof-of-principle demonstrations for fundamental physics applications. One example of such an initiative is the QSNET project - "A network of clocks for measuring

the stability of fundamental constant" [86], which seeks to link advanced atomic and molecular clocks, both current and next-generation, in a coordinated network to improve the detection of potential variations in fundamental constants (see figure 1.4.1). The network brings together existing systems, such as Cs, Sr and Yb^+ atomic clocks at the National Physical Laboratory, alongside other clocks under development: a N_2^+ molecular ion clock at the University of Sussex, a CaF optical lattice clock at Imperial College London, and a Cf highly charged ion clock at the University of Birmingham [33]. By connecting diverse clocks that possess heightened sensitivity to variations in fundamental constants like the fine-structure constant (α) and the electron-to-proton mass ratio (μ), QSNET aims to advance the ability to detect phenomena such as dark matter interactions and possible violations of fundamental symmetries.

Building on the objectives of QSNET, this thesis focuses on the experimental and theoretical groundwork necessary for the realization of the Cf highly charged ion clock, a key component of the network. This work involved performing proof-of-principle spectroscopy measurements of highly charged nickel ions (see Chapter 7) in an Electron beam ion trap. Additionally, a new ion injection system for handling rare radioactive elements such as Cf has been developed (refer Chapter 5). Complementary to the experimental efforts, theoretical calculations using computational codes were conducted for highly charged Cf ions, providing predictions that will support future spectroscopic investigations (see Chapter 6).

2 Theory

This chapter outlines the theoretical framework necessary to understand the atomic properties and interactions relevant to HCIs, particularly in the context of high-precision spectroscopy and their potential applications in probing fundamental physics.

Section 2.1 begins with an overview of relevant atomic physics, covering both one-electron and multi-electron systems, and extends this understanding to HCIs, which occupy a unique regime due to their high nuclear charge and a reduced electronic configuration. Particular emphasis is placed on transition probabilities and external field effects such as the Zeeman effect, which are essential for interpreting spectroscopic data and identifying viable clock transitions in HCIs. Section 2.2 presents the concept of level crossings in highly charged californium ions, which can lead to enhanced sensitivity to variations in fundamental constants. Section 2.3 gives a brief overview of the key ionization processes occurring within an electron beam ion trap, such as electron impact ionization, radiative recombination, and autoionization. Section 2.4 introduces atomic structure codes used to calculate energy levels, transition rates, and other properties essential for interpreting experimental results and identifying suitable clock candidates.

2.1 Atomic Structure and Spectroscopy Basics

Atomic physics provides the framework to describe the behavior of electrons in both simple and complex atomic systems. This section begins with one-electron atoms and then extends to multi-electron systems, highlighting the concepts and effects relevant to highly charged ions.

2.1.1 One-Electron Atomic Systems

Hydrogen-like ions, comprising a nucleus with charge Ze and a single bound electron, represent one of the most fundamental atomic systems. Due to their simplicity, they provide an ideal framework for exploring the underlying properties of highly charged

ions. The Schrödinger equation for such a system is given by [87] :

$$\hat{H}\Psi(\mathbf{r},t) = \left(-\frac{\hbar^2}{2m}\nabla^2 + V(\mathbf{r},t)\right)\Psi(\mathbf{r},t) = E\Psi(\mathbf{r},t)$$

The Hamiltonian operator $\hat{H}$ represents the total energy of the quantum system and acts on the wavefunction $\Psi(\mathbf{r},t)$, which describes the state of the particle as a function of position and time. The term $-\frac{\hbar^2}{2m}\nabla^2$ corresponds to the kinetic energy operator, where $\hbar$ is the reduced Planck constant, m is the particle's mass, and ∇^2 is the Laplacian accounting for spatial variation of the wavefunction. $V(\mathbf{r},t)$ is the potential energy that depends on position and time. E is the energy eigenvalue associated with the wave function $\Psi(\mathbf{r},t)$ and represents the measurable energy value of the system in this state. Solving this Schrödinger equation for the Coulomb potential $V(r) = -\frac{Ze^2}{4\pi\epsilon_0 r}$ gives the energy as [88] :

$$E_n = -\left[\frac{m_e}{2\hbar^2}\left(\frac{Ze^2}{4\pi\epsilon_0}\right)^2\right]\frac{1}{n^2},\ n = 1,2,3,... \tag{2.1}$$

where n is the principal quantum number. However, the Schrödinger equation, as formulated above, is inherently non-relativistic and does not account for the intrinsic spin of the electron nor relativistic effects that become significant especially for ions with high nuclear charge Z. The energy derived after including those corrections (collectively called fine-structure) is given by [89, 90]

$$\Delta E_{fs} = -\frac{mc^2Z^4\alpha^2}{2n^3}\left(\frac{1}{j+\frac{1}{2}} - \frac{3}{4n}\right) \tag{2.2}$$

where j is the total angular momentum, n is the principal quantum number and the fine-structure constant α is given by:

$$\alpha = \frac{e^2}{2\epsilon_0 hc}$$

The Dirac equation on the other hand incorporates both the electron's spin and relativistic effects, and one can also derive the fine-structure shown in equation 2.2. The Dirac Hamiltonian is given by [91]:

$$H_D = c\alpha p + (\beta - 1)mc^2 + V \tag{2.3}$$

where α and β are Dirac operators usually expressed in Paul spin matrices, p is the momentum operator, c is the speed of light, V is the Coulomb potential.

The exact relativistic energy eigenvalue solution for a hydrogen-like atom (one electron bound to a nucleus of charge Ze) is [90]

$$E_{nj} = mc^2 \left\{ \left[1 + \frac{\alpha^2 Z^2}{\left(n - (j+1/2) + \sqrt{(j+1/2)^2 - (\alpha^2 Z^2)} \right)^2} \right]^{-\frac{1}{2}} - 1 \right\} \tag{2.4}$$

An expansion in powers of α by following Sommerfeld's treatment, yields the first two terms as:

$$\frac{E_{nj}}{hc} = -\frac{RZ^2}{n^2} - \frac{R\alpha^2 Z^4}{n^3} \left(\frac{1}{j+1/2} - \frac{3}{4n} \right) \tag{2.5}$$

where R is the Rydberg constant. This expression is identical to the sum of equation 2.1 and 2.2, which is the non-relativistic energy and the fine-structure correction, respectively.

2.1.2 Multi-Electron Atomic Systems

While hydrogen-like ions can be treated analytically due to the presence of only a single electron, atoms and ions with multiple electrons present a much more complex quantum mechanical problem. When accounting for both the kinetic energy of the electrons and their interactions with the electrostatic field of the nucleus, assumed to be infinitely massive, as well as the mutual electrostatic repulsion between electrons, the Hamiltonian for an atom or ion with nuclear charge Ze and N electrons is given by [92]

$$H = \sum_{i=1}^{N} \Big(-\frac{\hbar^2}{2m} \nabla_{r_i}^2 - \frac{Ze^2}{(4\pi\epsilon_0) r_i} \Big) + \sum_{i<j=1}^{N} \frac{e^2}{(4\pi\epsilon_0) r_{ij}} \tag{2.6}$$

In this expression, r_i represents the position vector of the ith electron relative to the nucleus, and $r_{ij} = |r_i - r_j|$ is the distance between electrons i and j. The final term accounts for the electron-electron repulsion, summed over all distinct electron pairs. The inclusion of the electron-electron interaction term makes it impossible to solve the Schrödinger equation exactly, as the motion of each electron depends on all the others. This results in a many-body problem, for which approximation methods are required. One such approximation is the central field approximation which assumes that each electron moves independently in an average, spherically symmetric potential generated by the nucleus and the other electrons. This allows the use of hydrogen-like orbitals as

a basis but with effective nuclear charges to account for screening by inner electrons. This is the basis for the Hartree and Hartree-Fock methods, where the wavefunction is written as a product (or Slater determinant) of single-electron orbitals [92].

In multi-electron atoms, each electron has orbital angular momentum l_i and spin $s_i = 1/2$. These combine in different ways depending on the atomic number resulting in coupling schemes which are approximations of the real eigenstates, that provide generally valid results either for light atoms (LS) or heavy atoms(jj):

- LS (Russell–Saunders) coupling (valid for light atoms):

$$\vec{L} = \sum \vec{l}_i, \quad \vec{S} = \sum \vec{s}_i, \quad \vec{J} = \vec{L} + \vec{S}$$

  The atomic states are labeled using term symbols:

$$^{2S+1}L_J$$

  where L is represented by letters such as S, P, D, F for $L = 0, 1, 2, 3$, respectively.

- jj coupling (important for heavy atoms):
  Each electron's total angular momentum $j_i = l_i + s_i$ is calculated individually, and then summed to obtain $J = \sum j_i$. This scheme becomes necessary when spin-orbit interactions are strong.

2.1.3 Scaling in Highly Charged Ions

Highly charged ions are a natural extension of multi-electron atomic systems, characterized by the removal of a large number of electrons from an atom, resulting in strong Coulomb fields and pronounced relativistic and quantum electrodynamical effects. In HCIs, many atomic properties, such as binding energies, transition rates, and relativistic corrections, scale strongly with nuclear charge Z. While hydrogen-like ions follow simple Z-dependent trends, in multi-electron systems the scaling is better described using the effective nuclear charge Z_{eff}, where $Z_{\text{eff}} = Z - N_e$ (where N_e is the number of shielding electrons) [93]. The electron binding energy increases roughly as Z_{eff}^2 due to the enhanced Coulomb attraction. Fine-structure splittings, arising from relativistic corrections, scale approximately as Z_{eff}^4, becoming increasingly dominant in heavy ions. Hyperfine structure, which reflects the interaction between electron and nuclear magnetic moments, typically scales as Z_{eff}^3. Additionally, quantum electrodynamical (QED) effects such as the Lamb shift scale as Z_{eff}^4 [35].

2.1.4 Transition Probabilities

When an atom or ion transitions from an excited state to a lower one, a photon is emitted whose energy corresponds to the difference between the two energy levels. The probability of such a radiative transition occurring is governed by quantum mechanical selection rules, which dictate whether a transition is allowed or forbidden based on specific properties of the initial and final states. One important selection rule involves parity [94]:

$$\Delta P = \begin{cases} (-1)^{\kappa} & \text{for electric multipole } E_{\kappa} \text{ transitions} \\ -(-1)^{\kappa} & \text{for magnetic multipole } M_{\kappa} \text{ transitions} \end{cases} \tag{2.7}$$

Here, κ denotes the multipole order of the transition: $\kappa = 1$ corresponds to dipole transitions, $\kappa = 2$ to quadrupole transitions, and so forth.

Additionally, the total angular momentum J and the magnetic quantum number M which represents the projection of J onto the quantization axis, satisfy the selection rules:

$$\Delta J = 0, \pm 1, ..., \pm\kappa, \quad |J - J'| \leq \kappa \leq J + J' \tag{2.8}$$

$$\Delta M = 0, \pm 1, ..., \pm\kappa \tag{2.9}$$

The intensity I_{10} of the spectral line corresponding to the transition from the upper state 1 to the lower state 0 is given by

$$I_{10} = N_1 \cdot A_{10} \cdot \hbar\omega \tag{2.10}$$

where N_1 is the population density of atoms in the upper state, A_{10} is the Einstein coefficient for spontaneous emission, which gives the transition rate from state 1 to state 0 and $\hbar\omega$ is the energy of the emitted photon, given by $\hbar\omega = E_1 - E_0$.

The rate at which a one-photon transition occurs from an initial excited state $|a\rangle$ to a final excited state $|b\rangle$ is quantified by the transition probability per unit time, expressed as

$$dA = \frac{e^2\omega}{2\pi\hbar c}\left|\langle b|\vec{\alpha}\vec{\epsilon}^{*} \cdot e^{-i\mathbf{kr}}|a\rangle\right|^2 d\Omega. \tag{2.11}$$

Here, $\langle b|$ and $|a\rangle$ represent the relativistic wavefunctions obtained from the Dirac equation, $\vec{\alpha}$ is the Dirac matrix, $\vec{\epsilon}$ stands for the polarization vector, $\mathbf{k}$ is the photon momentum vector, and $d\Omega$ represents the differential solid angle element of the radiation.

The Einstein A coefficient, which quantifies the transition probability for electric dipole (E1) transitions, is related to the absorption oscillator strength f_{ik} (dimensionless) and the line strength S (which quantifies the squared transition dipole moment) through the following expression [95, 96]:

$$^{\mathrm{E1}}A_{ki} = \frac{2\pi e^2}{m_e c\epsilon_0 \lambda^2}\frac{g_i}{g_k}f_{ik} = \frac{16\pi^3}{3h\epsilon_0\lambda^3 g_k}S \tag{2.12}$$

where e is the elementary charge, m_e is the electron mass, c is the speed of light, λ is the transition wavelength, ϵ_0 is the vacuum permittivity and g_i and g_k are statistical weights of the lower and upper level given by $2J_i + 1$ and $2J_k + 1$ with J being the total angular momentum quantum number. The line strength S is often expressed in units of $\mathrm{m^2C^2}$.

For E2 transitions, the spontaneous emission probability is given by:

$$^{\mathrm{E2}}A_{ki} = \frac{16\pi^5}{15h\epsilon_0\lambda^5 g_k}S \tag{2.13}$$

Here S is the electric quadrupole line strength, expressed in SI units as $\mathrm{m^4C^2}$.

For M1 transitions, the corresponding transition probability is given by:

$$^{\mathrm{M1}}A_{ki} = \frac{16\pi^3\mu_0}{3h\lambda^3 g_k}S \tag{2.14}$$

Here S is the magnetic dipole line strength, with units of $\mathrm{J^2T^{-2}}$ where J is joules and T is tesla and μ_0 is the magnetic permeability of free space.

For the present work, the most relevant ones are E1 and M1 transitions as these possess the largest transitions probabilities and therefore produce observable spectral lines. E2 transitions which are generally too weak to be detected under typical EBIT conditions, can be inferred indirectly using the Rydberg-Ritz principle, which is discussed in Section 6.2.4.

2.1.5 Zeeman Effect

When an atom is placed in an external magnetic field, such as the 8 T field in the Heidelberg EBIT, its energy levels shift due to the interaction between the magnetic field and the magnetic moment associated with the electrons' angular momentum. This phenomenon, known as Zeeman splitting, removes the degeneracy of magnetic sublevels by splitting a single energy level into several distinct components corresponding to different magnetic quantum numbers.

The magnetic dipole moment associated with the total angular momentum **J** of the atom arises from both the orbital and spin angular momenta of the electrons and can be expressed as [87]

$$\boldsymbol{\mu} = -\mu_B(\mathbf{L} + g_s\mathbf{S}), \tag{2.15}$$

where μ_B is the Bohr magneton and g_s is the electron spin g-factor.

The Hamiltonian describing the interaction with the external magnetic field **B** is then given by

$$H_{\mathrm{ZE}} = -\boldsymbol{\mu} \cdot \mathbf{B}. \tag{2.16}$$

If the energy from this interaction is much smaller than the fine-structure splitting, it can be treated as a perturbation. Using the vector model, the magnetic moment is projected onto the total angular momentum **J**, assuming the magnetic field is oriented along the z-axis.

In this approximation, the Zeeman energy shift becomes

$$E_{\mathrm{ZE}} = g_J \mu_B B M_J, \tag{2.17}$$

where M_J is the magnetic quantum number.

The Landé g-factor, g_J, can be estimated using the well-known formula:

$$g_J = 1 + \frac{J(J+1) - L(L+1) + S(S+1)}{2J(J+1)}. \tag{2.18}$$

The Zeeman effect thus splits a spectral line into $2J+1$ components. When considering transitions between these Zeeman sublevels, each magnetic quantum number M_J must be treated separately. The general selection rule for multipole transition of order κ is given in equation 2.9. In practice, the most intense Zeeman components come from changes in magnetic quantum number $\Delta M = 0, \pm 1$, which correspond to the dominant E1 and M1 transitions. The $\Delta M = 0$ transition are called the π transitions which are polarized parallel to the magnetic field and the $\Delta M = \pm 1$ transitions are called σ transitions, with $\sigma^+(+1)$ and $\sigma^-(-1)$ polarized perpendicular to the magnetic field.

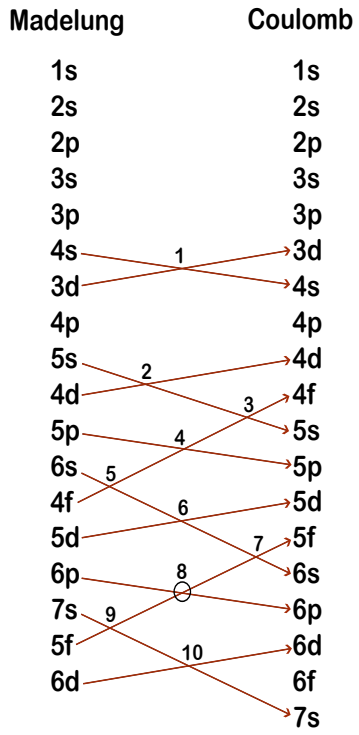

Figure 2.2.1: Comparison of Coulomb and Madelung orbital energy orderings. Level crossings in HCIs between orbitals are marked with numbers from 1 to 10. The crossing labeled 8, highlighted with a circle, corresponds to the $5f-6p$ level crossing in californium ions Cf^{15+} and Cf^{17+}. Figure adapted from [53].

2.2 Level Crossing in Californium

In neutral atoms, the ordering of electrons among orbitals is generally well described by Madelung ordering. In this scheme, orbitals fill in order of increasing $n + l$, and when $n + l$ values are equal, the orbital with the lower n fills first (see figure 2.2.1). For example, the $4s$ orbital is filled before the $3d$ orbital.

In HCIs, the removal of electron reduces electron-electron screening, and the remaining electron experience a much stronger effective nuclear potential. In such systems, the energies depend primarily on the principal quantum number n, and the ordering shifts from Madelung towards Coulomb ordering. Thus, crossings of energy levels occur as the ionization increases, as shown in figure 2.2.1; these are referred to as level crossings. Close to such a crossing, the energy difference between the two levels becomes very small, allowing transitions in the optical range which can be highly sensitive to variations in α. This sensitivity is quantified by the parameter q, introduced in Equation 1.9. For a level with principal quantum number n and total angular momentum

j, q can be approximated by [97]:

$$q_{nj} \approx -I_n \frac{(Z\alpha)^2}{\nu(j+1/2)} \tag{2.19}$$

where I_n is the ionization energy, Z is the nuclear charge and ν is the effective principal quantum number. Transitions between levels near a crossing typically have large q-values.

In californium ions, particularly in charge states Cf^{16+} and Cf^{17+}, the $6p$ and $5f$ orbitals become nearly degenerate in energy, enabling E1 transitions between them that lie in the optical range. This near-degeneracy arises due to level crossing, where the $5f$ orbital, initially less bound in neutral or low-charge Cf ions, becomes more tightly bound than the $6p$ orbital in the highly charged Cf ions. As shown in figure 2.2.1, the system departs from the Madelung orbital ordering typical of neutral atoms and adopts a more Coulomb-like structure. The resulting inversion of the $5f$ and $6p$ energy levels occurs at the crossing labeled as point 8, which is marked with a circle in the figure.

In these highly charged Cf ions, the $6p_{1/2}$ orbital is affected by relativistic corrections because it has significant electron density near the nucleus. In contrast, the $5f$ orbital is more spatially extended and less affected. The resulting large difference in relativistic effects between the two orbitals leads to a transition with a high differential q-value, making it an excellent probe for potential variations in α [98].

2.3 Electron and Ion Dynamics in an EBIT

Electrons emitted from an electron gun (see Section 3.1.1) are radially compressed by a strong magnetic field, in case of the Heidelberg EBIT generated by superconducting Helmholtz coils at the trap center. These high-energy electrons collide with neutral atoms, resulting in the removal of bound electrons and produce HCIs. The dense electron beam generates a negative space-charge potential that traps the positive ions near the electron beam axis. The number of trapped ions is proportional to the electron density. Since the ions remain in continuous contact with the electron beam, several processes take place in the trap. A detailed explanation of these processes is given in [99]. These processes determine how ions are produced, excited and emit radiation. The most important ones are described below.

Electron impact ionization: This is the dominant process in the trap. When high-energy electrons collide with ions, and their kinetic energy E exceeds the ionization potential P_i of the valence electrons, the most loosely bound electrons are ejected from the ion, leading to electron impact ionization (EII).

$$A^{q+} + e^- \rightarrow A^{(q+1)+} + 2e^-$$

A^{q+} denotes the ion with charge q. An approximation of the cross section for EII is given by the empirical formula proposed by Lotz [100].

$$\sigma = \sum_{i=1}^{N} a_i q_i \frac{\ln E/P_i}{EP_i}\Big(1 - b_i\, e^{-c_i(E/P_i - 1)}\Big);\ E \geq P_i$$

where a_i, b_i and c_i are empirical parameters associated with subshells i, P_i is the binding energy, q_i is the number of electrons and N represents the number of subshells present.

Radiative recombination: The ions can undergo radiative recombination (RR) when a free electron is captured by a positively charged ion, emitting a photon.

$$A^{q+} + e^- \rightarrow A^{(q-1)+} + h\omega$$

where $h\omega$ represents the energy released, which equals the sum of the ion's binding energy and the kinetic energy of the free electron. The cross section for RR is derived from [101]:

$$\sigma_{rr} = \frac{8\pi\alpha^5 Z_{\text{eff}}^4}{3\sqrt{3}n^3 E_e h\omega}.$$

Here n is the principal quantum number, Z_{eff} is the effective charge.

Charge exchange: Charge exchange occurs when a highly charged ion collides with a neutral atom, molecule or residual gas particle and captures one (or more) electrons. This process reduces the charge state of the ion and often leaves it in an electronically excited state. It can be written as

$$A^{q+} + B \rightarrow \Big[A^{(q-1)+}\Big]^* + B^+$$

where B denotes a neutral particle.

Dielectronic Recombination: Two sequential steps characterize dielectronic recombination; initially, a free electron is captured by an ion while simultaneously exciting one of its bound electrons to a higher energy level, forming a doubly excited intermediate state. Subsequently, this state stabilizes by releasing a photon, producing a recombined ion with a reduced positive charge [99].

$$A^{q+} + e^- \rightarrow \left[A^{(q-1)+}\right]^* \rightarrow \left[A^{(q-1)+}\right] + h\omega$$

Electron impact excitation: When a free electron collides with an atom or ion and transfers sufficient energy to a bound electron, the atom or ion becomes excited - this process is known as electron impact excitation. This process is fundamental in plasma environments such as an EBIT, and leads to characteristic photon emission as the excited ion returns to a lower energy level [99].

$$A^{q+} + e^- \rightarrow \left[A^{(q+)}\right]^* + e^- \rightarrow A^{q+} + h\omega$$

The excited ion A^{q+} can subsequently either decay by spontaneous or stimulated photon emission or undergo autoionization, resulting in the loss of an electron.

Radiative excitation: When a photon with energy $\hbar\omega$ interacts with an ion, it can be absorbed, raising the ion into an electronically excited state without changing its charge. This process can be represented as

$$A^{q+} + \hbar\omega \rightarrow [A^{q+}]^*$$

Photoionization: When an ion absorbs a photon with sufficient energy, it can lose an electron and become more positively charged, resulting in the formation of a higher charge state ion and a free electron. The reaction can be described by the equation:

$$A^{q+} + \hbar\omega \rightarrow A^{(q+1)+} + e^-$$

Autoionization: This process occurs when an excited ion spontaneously ionizes by emitting an electron, resulting in an increase in its charge state, as expressed by:

$$[A^{q+}]^* \rightarrow [A^{q+1}] + e^-$$

The processes outlined above represent the essential interactions governing ion formation, charge state evolution and excitation in an EBIT. Under typical operating

conditions, electron impact ionization drives the production of HCIs, while recombination processes such as radiative recombination, dielectronic recombination and charge exchange with residual neutrals lead to a reduction of the charge state. The balance between these ionization and recombination process determines the steady-state charge state distribution achievable in the trap.

2.4 Codes for Atomic Structure Calculation

In order to calculate the structure of atomic systems, the computer software codes Flexible Atomic Code (FAC) and AMBiT are employed. FAC is an integrated software package capable of computing a broad spectrum of atomic parameters, including energy levels, radiative and collisional transitions, and ionization and recombination processes. By combining the Configuration Interaction (CI) method with Dirac-Hartree-Fock calculations, FAC produces results that fully account for relativistic effects [102].

AMBiT integrates the Configuration Interaction approach with Many-Body Perturbation Theory (MBPT) [103]. It uses the particle-hole formalism, meaning it focuses on the "holes" or missing electrons in otherwise filled shells, to improve accuracy. Besides the usual corrections that account for interactions between the inner (core) and outer (valence) electrons, MBPT can also be used to handle interactions among the outer electrons themselves, especially those in higher energy levels. The calculation results for specific Cf and Ni HCIs are given in Chapter 6.

2.4.1 Configuration Interaction

The CI method makes the atomic structure calculation more accurate by taking into account how electrons interact with each other. The many-electron wavefunction Φ is expressed as a combination of Slater determinants, each representing a specific arrangement of electrons in the orbitals [104]:

$$\Phi = \frac{1}{\sqrt{N!}} \begin{vmatrix} \phi_1(\mathbf{x}_1) & \phi_2(\mathbf{x}_1) & \cdots & \phi_N(\mathbf{x}_1) \\ \phi_1(\mathbf{x}_2) & \phi_2(\mathbf{x}_2) & \cdots & \phi_N(\mathbf{x}_2) \\ \vdots & \vdots & \ddots & \vdots \\ \phi_1(\mathbf{x}_N) & \phi_2(\mathbf{x}_N) & \cdots & \phi_N(\mathbf{x}_N) \end{vmatrix} \tag{2.20}$$

where $\mathbf{x}_i = (\mathbf{r}_i, \sigma_i)$ denotes the spatial and spin coordinates of the ith electron and $\phi_j(\mathbf{x}_i)$ are single-electron wavefunctions. The total CI wavefunction is then a linear combination of several such determinants and includes excited configurations [105];

$$\Psi_{\mathrm{CI}} = c_0\Phi_0 + c_1\Phi_1 + c_2\Phi_2 + \dots \tag{2.21}$$

where Φ_0 is the Hartree-Fock ground state determinant, $\Phi_1,\ \Phi_2, \cdots$ are excited state determinants and $c_0,\ c_1, \cdots$ are the coefficients that determine the contribution of each configuration to the total wavefunction.

2.4.2 Configuration Interaction + Many-Body Perturbation Theory

CI has limited ability to account for core-core and core-valence correlations, especially in complex systems like highly charged ions. MBPT is effective in calculating them, although it is less accurate in valence-valence correlation. The CI+MBPT method combines the strength of both techniques [99].

- MBPT is first used to build an effective Hamiltonian that incorporates core-valence correlation corrections
- This Hamiltonian is then used in a CI calculation to handle valence-valence correlation.

By combining these two methods, CI and MBPT achieve high accuracy in calculating energy levels in HCIs including those near level crossings where the correlation effects may reorder energy levels.

3 HD-EBIT Experimental Setup

Electron beam ion traps have been extensively utilized for several decades as powerful tools to produce and confine highly charged ions. These devices enable detailed studies of atomic structure and fundamental electron-ion interaction processes of HCIs and allow plasma diagnostics to be performed. The conceptual predecessor to EBITs, electron beam ion source (EBIS), was first developed by Donets in 1969 [106]. The original EBIS was primarily designed as an ion source for accelerators, but its design laid the groundwork for subsequent developments in ion trapping technology.

Over time, with improvements in ion confinement techniques, the focus shifted towards trapping and studying HCIs for extended durations, leading to the emergence of the EBIT as a specialized variant of EBIS. The term EBIT reflects this transition from merely producing ions to actively trapping them using an intense, focused electron beam.

The first section of this chapter provides a detailed overview of the Heidelberg EBIT (HD-EBIT), which was formerly known as FreEBIT, a prominent instrument in this field. Originally constructed in Freiburg in 1999 [107], the HD-EBIT was later relocated to Heidelberg in 2001, where it has since operated continuously [108]. The HD-EBIT has played a significant role in advancing research on HCIs, offering high precision and stability in ion trapping and spectroscopy [108, 109].

The second section focuses on the injection system for gaseous and organic elements and its implementation in the HD-EBIT. The third section describes the Czerny-Turner optical spectrometer employed at the HD-EBIT.

3.1 Heidelberg Electron Beam Ion Trap

HCIs are generated through a process known as electron impact ionization (see Section 2.3), in which electrons are sequentially stripped from neutral atoms or low-charged ions by repeated collisions with high-energy electrons. In the context of an EBIT, this

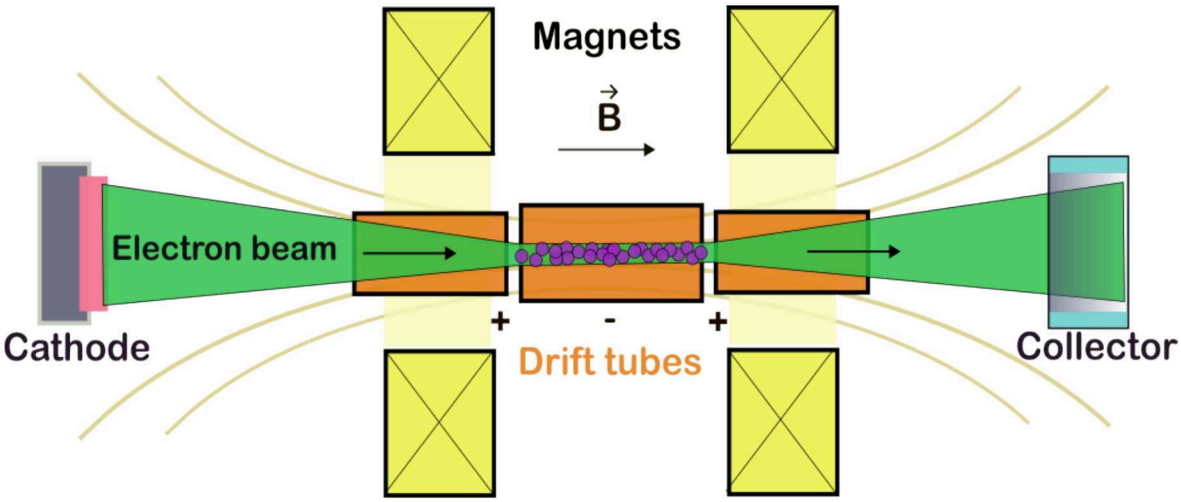

Figure 3.1.1: Schematic overview of an electron beam ion trap. The main components, including the cathode (electron gun), drift tubes, collector, and magnets generating the axial magnetic field, are indicated. The purple spheres in the center of the drift tube are the trapped ions.

is accomplished using a tightly focused, high-current electron beam that passes through a central region of the trap.

Figure 3.1.1 shows a schematic representation of an EBIT. The process begins with the generation of an electron beam, which is subsequently compressed and focused by a strong axial magnetic field. This magnetic field is typically produced by superconducting or permanent magnets and plays a crucial role in confining and guiding the beam along the central axis of the EBIT. As the beam traverses the trap region, it encounters neutral atoms or low-charge-state ions that have been injected into the system. Through successive collisions, the beam electrons ionize these atoms by removing one or more bound electrons at a time.

This ionization process continues as the ions remain confined in the trap, allowing for the accumulation of very high charge states over time. After passing through the interaction region, the electron beam proceeds to the final stage of the system, where it is ultimately collected. While this overview outlines the general mechanism of HCI production in an EBIT, the specific functions and design considerations of components such as the electron gun, ion trap, and collector are addressed in the following sections.

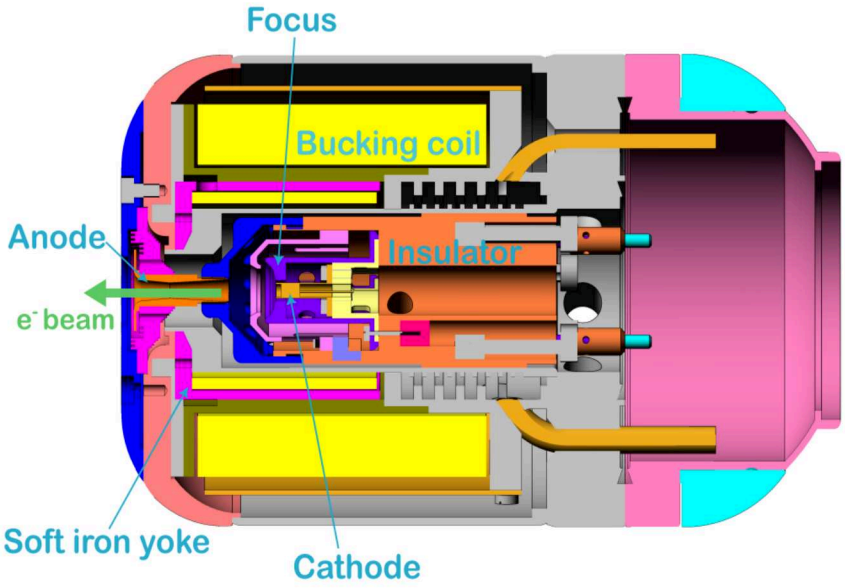

Figure 3.1.2: Sectional view of the electron gun of the HD-EBIT. The electrodes namely the cathode, focus, and anode are shown here. These electrodes are essential for the emission, control, and extraction of the electron beam. The control of the magnetic field is provided by the bucking coil and the soft iron yoke.

3.1.1 HD-EBIT Electron Gun

A sectional view of the electron gun is shown in figure 3.1.2. At the center of the gun is the cathode, a 3 mm diameter tungsten filament doped with barium, which emits electrons when heated to high temperatures via thermionic emission. The electron gun also includes a focusing electrode and an anode, which together control the extraction and focusing of the electron beam. Electrons are extracted by applying a potential difference between the cathode and the anode, while the focusing electrode is used to shape and control the electron current.

The HD-EBIT is designed to deliver electron beam energies of up to 350 keV with currents as high as 750 mA, enabling the production of hydrogen-like ions of heavy elements up to uranium [107]. For the optical spectroscopy measurements performed in this work, the maximum electron beam energy was limited to 2.5 keV. To minimize the influence of the magnetic field generated by the superconducting coils at the trap center, the cathode is shielded using a soft iron yoke and a bucking coil.

3.1.2 HD-EBIT Central Region

Nine drift tubes (DTs) are arranged linearly inside a central tube following the electron gun as shown in figure 3.1.2. The central drift tube, DT9, has an inner diameter of 10 mm and features slotted apertures. These drift tubes serve to axially confine HCIs by producing an electrostatic potential along the beam axis. DT9 is positioned at the center of the trap region, where two superconducting Helmholtz coils generate a strong magnetic field that radially compresses the electron beam, enhancing ionization efficiency.

To maintain superconductivity in the coil windings, liquid helium is refilled weekly into the inner cryogenic shield during operation, keeping the temperature at approximately 4.2 K and enabling ultra-high vacuum conditions with a trap-center pressure on the order of 10^{-13} mbar. This inner shield is surrounded by two additional thermal shields at 20 K and 50 K, which are cooled via a cryocooler cold head. During standard operation, the superconducting coils are operated in persistent mode, in which the power supply is disconnected after charging and the current (76.24 A) circulates indefinitely in the closed superconducting loop, producing a magnetic field of approximately 8 T at the trap center.

When neutral atoms are introduced into the trap center (DT9), they interact with the compressed electron beam and undergo successive electron impact ionization, leading to the formation of HCIs. Trapping of these ions is achieved both axially and radially. Axial confinement is realized by applying a lower voltage to DT9 and higher voltages to its adjacent drift tubes, forming a potential well along the trap axis (see figure 3.1.3 for the voltage configuration). Radial confinement arises from the negative space charge of the electron beam and the strong axial magnetic field provided by the superconducting coils.

To control the charge sate distribution of ions, the trap can be regularly dumped by adjusting the drift tube potentials. In typical operation, the dumping cycle can be configured to release trapped ions for a brief period, for example, 5 s following an accumulation phase of approximately 595 s. This allows for systematic measurements and prevents overloading of the trap with unwanted charge states.

The central region of the EBIT has six access ports (see figure 3.1.3). The opposing ports along the Z-axis accommodate the electron gun and the collector. Ports along the X-axis provide access for optical and X-ray spectroscopy. The bottom Y-axis port is typically used for neutral gas injection (see Section 3.2), while the top Y-axis port remains unused during standard operation. In setups requiring laser-based atom injec-

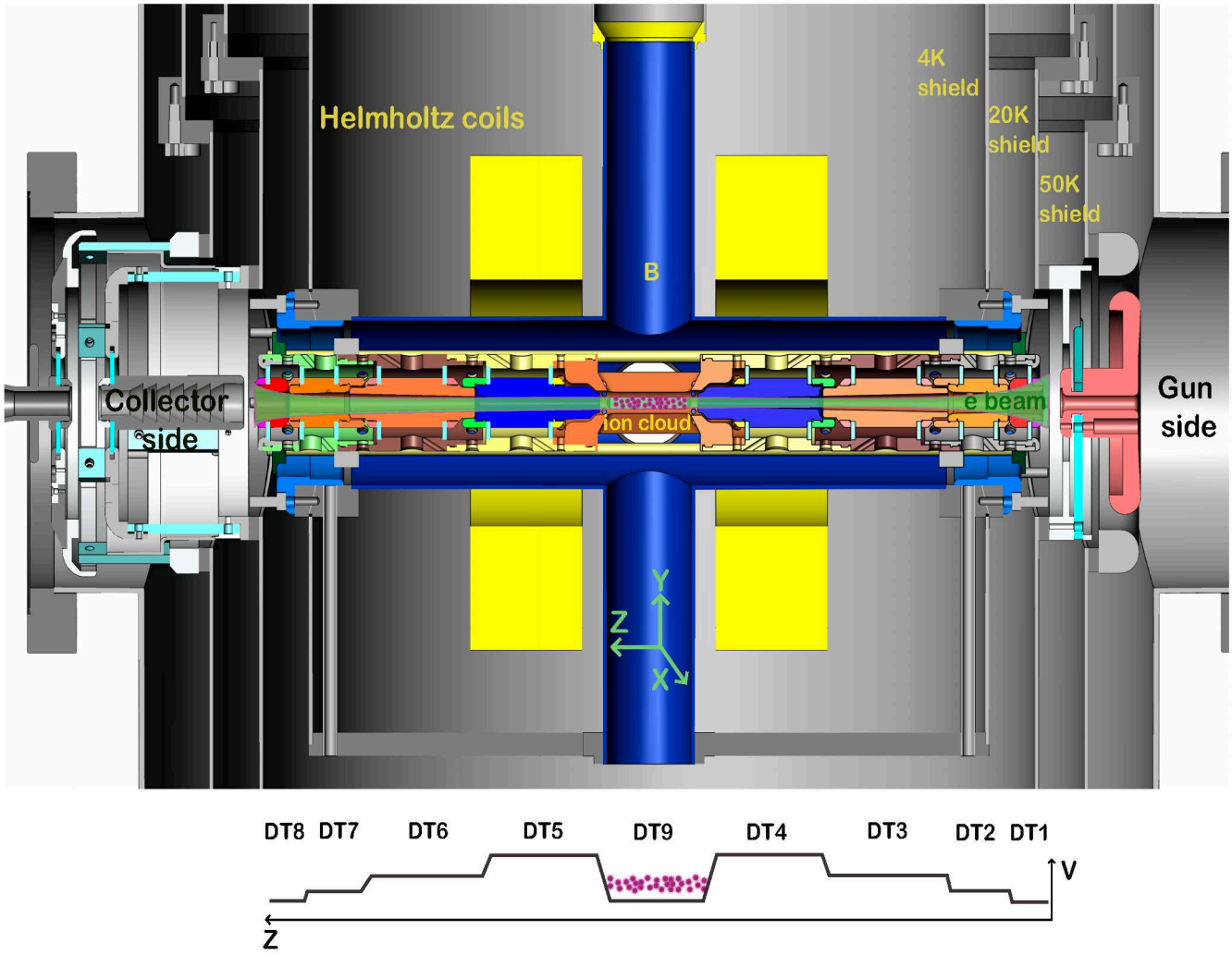

Figure 3.1.3: Top: Schematic diagram of the drift tube assembly inside the HD-EBIT, showing the linear arrangement of nine drift tubes (DTs) and the electron beam trajectory. The electron beam is compressed toward the central drift tube (DT9) by a strong axial magnetic field generated by two superconducting coils positioned around the trap region.
Bottom: Axial trapping potential (voltage vs. Z-position) applied to the drift tubes. The central tube (DT9) is held at a lower potential relative to its neighboring tubes, producing an electrostatic potential well that axially confines the highly charged ions. The outer drift tubes are held at even lower voltages to maintain electron beam propagation and confinement along the axis.

tion, these Y-axis ports are repurposed: the bottom port is used for target insertion, and the top port is used to direct laser light toward the target. Details of this procedure are discussed in Chapter 5.

3.1.3 Electron Beam

Ions are produced and trapped at the center of drift tube DT9. To estimate the charge states produced in the trap center, a precise determination of the electron beam energy is essential. One important parameter is the radius of the electron beam r_H, which encloses approximately 80% of the total beam. As described by Hermann in [110], this radius is given by:

$$r_H = r_B \sqrt{\frac{1}{2}\sqrt{\frac{1}{4} + \frac{8 m_e k_B T_c {r_c}^2}{e^2 B^2 {r_B}^4} + \frac{{B_c}^2 {r_c}^4}{B^2 {r_B}^4}}}$$

Here r_c is the cathode radius, B_c is the magnetic field strength at the cathode surface, T_c is the temperature of the cathode, k_B is the Boltzmann constant, and e is the elementary charge. The Brillouin radius r_B, which represents the minimum radius of the electron beam under ideal focusing, is given by:

$$r_B = \sqrt{\frac{m_e I_e}{\pi \epsilon_0 v_z e B^2}}$$

where the ϵ_0 is the vacuum permittivity, I_e is the electron beam current, v_z is the axial electron velocity, m_e is the electron mass and, B is the axial magnetic field. The calculated value of r_H ranges between 40 µm and 200 µm [111].

The effective electron beam energy E_e at the trap center depends on the cathode potential U_c, the central drift tube potential U_{DT9} and the space charge potential Φ_{sc}, and is given by:

$$E_e = e(U_{\mathrm{c}} + U_{\mathrm{DT9}} - \Phi_{\mathrm{sc}})$$

The space charge potential Φ_{sc}, which arises due to the negative charge of the electron beam compressed by the strong magnetic field, varies with the radial distance from the

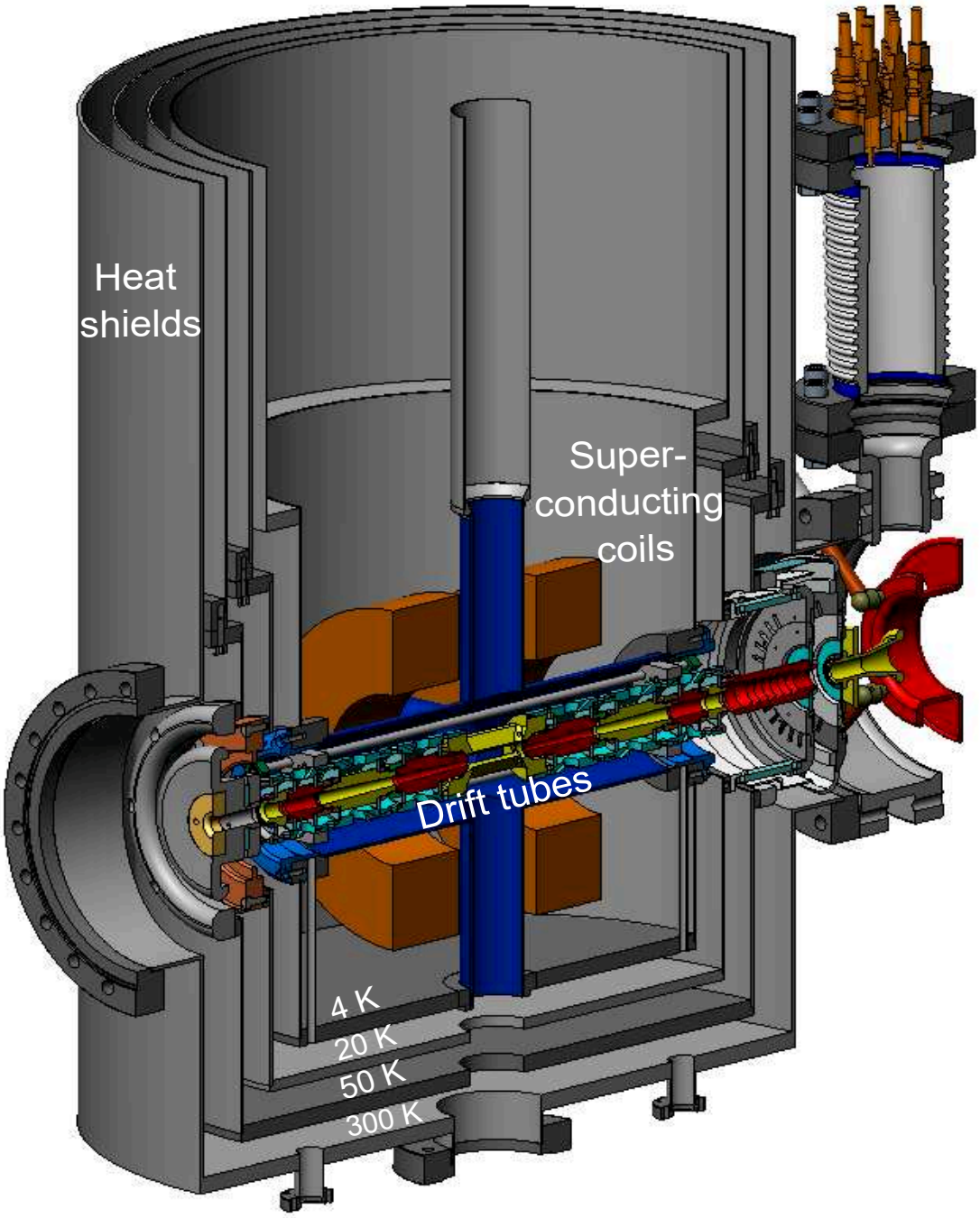

Figure 3.1.4: Heidelberg electron beam ion trap. Adapted from [112]

beam axis. It is expressed as:

$$\begin{aligned}\Phi_{sc} &= \frac{\rho}{2\pi\epsilon_0}\left(\frac{r^2}{2r_{\mathrm{H}}^2} - \frac{1}{2} - \ln\left(\frac{r}{r_{\mathrm{DT9}}}\right)\right), \text{for } r \leq r_{\mathrm{H}} \\ \Phi_{sc} &= \frac{\rho}{2\pi\epsilon_0}\ln\left(\frac{r}{r_{\mathrm{DT9}}}\right), \text{for } r \geq r_{\mathrm{H}}\end{aligned} \tag{3.1}$$

where ρ is the charge density of the electron beam, given by

$$\rho = \frac{I}{\pi v r_{\mathrm{H}}^2}$$

Once produced, trapped ions experience continuous heating due to Coulomb interactions with the high-energy electron beam, see Section 2.3. To mitigate this, evaporative cooling is employed: low-Z ions, gain sufficient energy through collisions, preferentially escape over the axial potential barriers. This selective loss of lighter ions reduces the overall kinetic energy of the trapped ion ensemble, thereby cooling the remaining highly charged ions [113].

3.1.4 HD-EBIT Collector

After passing through the drift tube region, the electron beam is collected at the collector. A schematic representation of the collector is shown in figure 3.1.5. Surrounding the collector is a coil that generates a magnetic field to deflect the electron beam toward the collector walls. Secondary electrons produced during this process, which may become trapped in a Penning mode configuration [114], are drawn into the suppressor electrode, thereby preventing them from re-entering the trap region. An additional electrode, known as the extractor, is maintained at a high negative potential to prevent any remaining electrons from escaping the collector. This extractor electrode also serves the purpose of extracting highly charged ions from the trap.

A schematic overview of the Heidelberg electron beam ion trap, including the electron gun, central trapping region, and collector described above, is shown in figure 3.1.4.

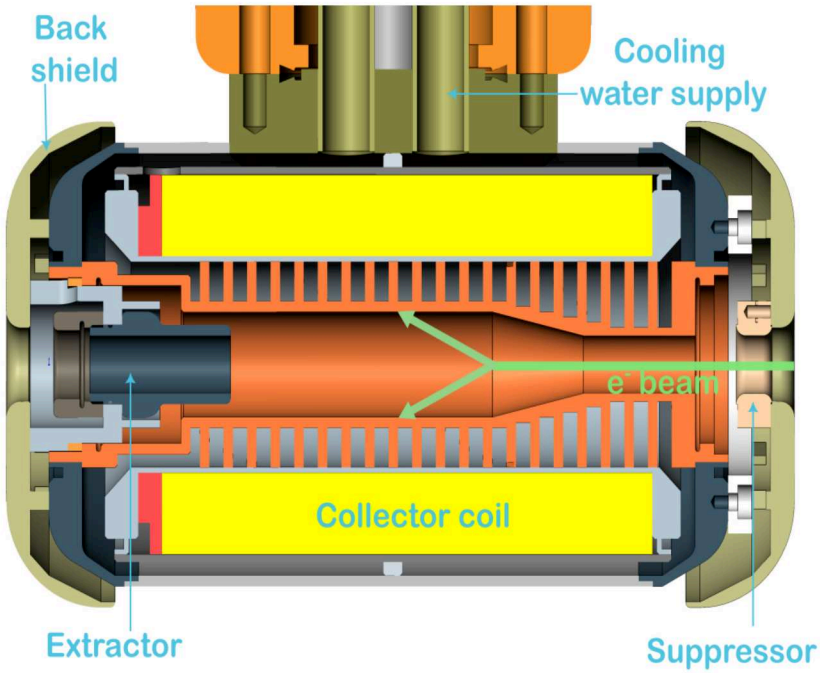

Figure 3.1.5: Sectional view of the collector of HD-EBIT. Due to the magnetic field from the collector coil, the electron beam from the trap diverges into the walls shown in orange. The high negative potential at the extractor electrode draws out positively-charged ions into a beam line and prevents the electrons from leaving the collector.

3.2 Injection System for Gases and Volatile Organic Compounds

The injection of elements in gaseous form or as volatile organic compounds into the trap is achieved using the following system: the substance held in a bottle or container, in its gaseous or volatile form, is connected to a needle valve, which regulates flow into a differential pumping system. Differential pumping systems are used in vacuum engineering to maintain distinct pressure zones within connected regions of an experimental setup. This is accomplished by separating the regions with narrow apertures and equipping each with its own dedicated vacuum pump.

The HD-EBIT gas injection system employed in this experiment is a differential pumping system consisting of two stages, each maintained at a distinct pressure by individual turbomolecular pumps. Pressure gauges are installed on both stages to monitor vacuum conditions. The stages are separated by an aperture (A1 in figure 3.2.1), a slit measuring approximately 3 mm $\times$ 3 mm, which helps establish a pressure differential

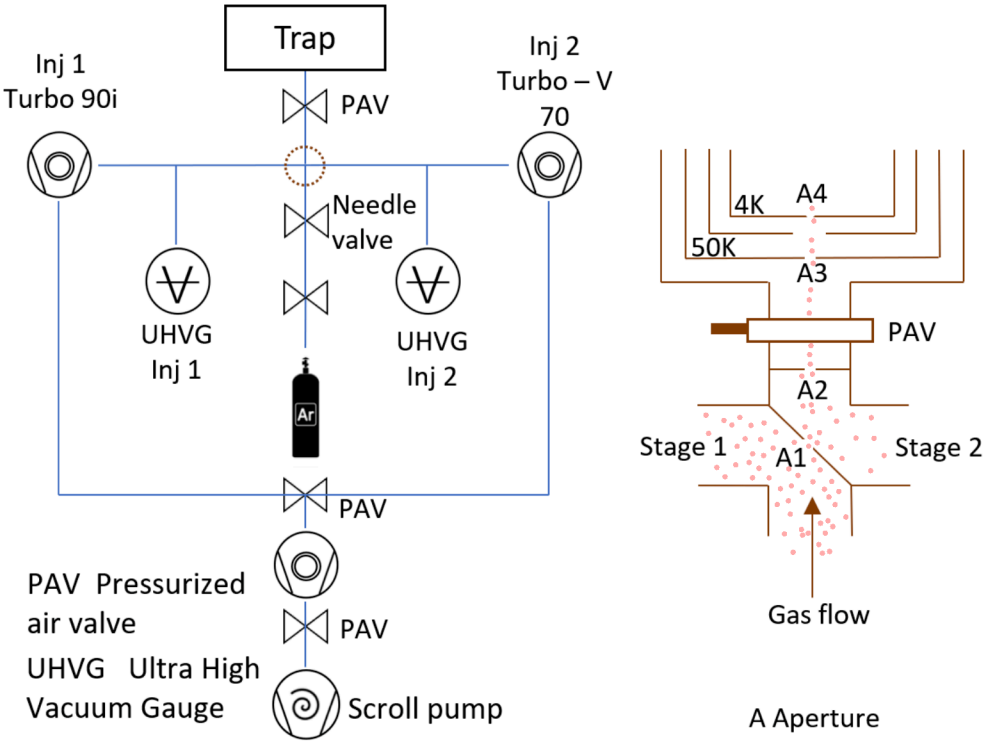

Figure 3.2.1: The schematic diagram of the vacuum system for the injection of gaseous elements and volatile organic compounds is shown on the left. The dotted circle is zoomed in on the right side which indicates flow of the gas in each stages and apertures. With this method a narrow stream of the atomic beam can be produced. Adapted from [115].

of approximately one order of magnitude between the stages.

After passing through the differential pumping system, the gas encounters another aperture A2, also a slit, measuring 20 mm in length and 4 mm in width, which is connected to the valve of the EBIT. Beyond the valve, the third aperture A3 is located at the 50 K thermal shield, consisting of a plate with a rectangular opening measuring 8 mm $\times$ 4 mm. The fourth aperture, positioned at the 4 K shield, is a slit measuring 15 mm in length and 2 mm in width. These apertures serve to collimate the gas stream, allowing a narrow and directed flow into the central drift tube. A schematic of this injection system is shown in figure 3.2.1.

Noble gases, such as argon and xenon, were injected into HD-EBIT during previous measurement campaigns. The injection procedure is as follows. The needle valve connected to the Ar/Xe gas bottle is slightly opened to achieve pressures of approximately 10^{-7} mbar in the first stage and 10^{-8} mbar in the second stage, respectively.

Nickel injection is carried out in a slightly different manner because it involves a non-gaseous volatile compound: Bis(2,2,6,6-tetramethyl-3,5-heptanedio)nickel(ii), CAS No. 41749-92-2, commonly referred to as bis(nickel) [116]. Approximately 2 grams of this compound are placed in a small container in a nitrogen environment to prevent oxidation by atmospheric oxygen. The container is then connected directly to the injection system without a needle valve.

The container with nickel and its transfer line to the valve located beneath the EBIT is then gradually heated in a controlled incremental fashion to 65 °C. Under a pressure below 1.8×10^{-3} mbar [116], the compound sublimates. The pressure conditions in the two stages are maintained as in the argon injection.

Although this injection method is simple and commonly employed, it relies on a continuous supply of material and thus requires relatively large quantities of the desired element. To enable experiments with rare or limited-quantity materials, the gas injection system was removed and replaced by a new configuration directly as discussed in detail in Chapter 5.

3.3 Czerny-Turner spectrometer

The electron beam excites ions, which subsequently emit photons during radiative de-excitation, as discussed in Section 2.3. To analyze this emission, the HD-EBIT

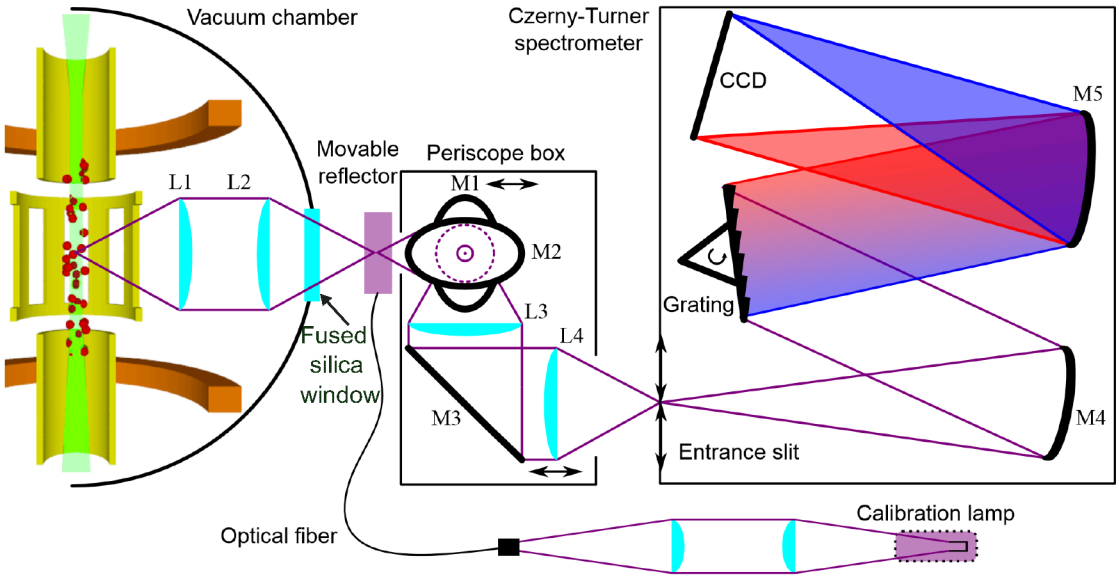

Figure 3.3.1: An overview of the optical spectrometer of HD-EBIT is shown here. This figure is taken from [112]. The optical path of the fluorescence light emitted from the ion cloud from DT9 to the CCD camera is illustrated here. The movable reflector reflects the calibration light into the periscope box taking the same path as the fluorescence light

is equipped with an optical spectrometer, as shown in figure 3.3.1. The path to the spectrometer contains several optical elements. The fluorescence light is collected by two lenses, L1 and L2, each with a diameter of 1 inch and a focal length of 150 mm. These are mounted inside the vacuum chamber along the optical path toward the fused silica window on the side of the main magnet chamber facing the drift tubes. The entrance slit of the spectrometer is vertical, thus the horizontal image of the ion cloud at the center of DT9 has to be rotated 90 degrees. This is achieved by a periscope system placed in a box after the window of the vacuum chamber.

Inside the periscope box, the mirror M1 collects and reflects the light to mirror M2, after which the lens L3 collimates the light to lens L4 via mirror M3. Lens L4 focuses the light to the entrance slit of the spectrometer. Due to the chromatic aberration inherent in the single lenses employed in this system, the focal length of each lens varies slightly with the wavelength of incident light. To mitigate this effect, lens L4 is mounted on a linear translation stage, to optimize the focus for each specific wavelength at the entrance slit of the spectrometer.

The spectrometer employed in this setup is a 2 m McPherson Model 2062, based on the Czerny-Turner optical configuration. Incident light entering through the entrance slit is

first directed onto the diffraction grating by the collimating mirror (M4). The diffracted light is then collected by the focusing mirror (M5) and subsequently directed onto a charge-coupled device (CCD) for image acquisition. The model Oxford instruments Andor Newton CCD with a pixel matrix 2048 × 512 is employed in this experiment. Each pixel has a size of 13.5 × 13.5 µm^2. To reduce thermal noise, the camera is cooled to −80°C.

By varying the angle of the grating, the range of the spectrum that is imaged can be changed. Additionally, the spectrometer's resolving power is influenced by the entrance slit width, which is adjustable from a maximum of 2 mm down to a fully closed state (0 µm).

Due to the limited availability of well-characterized wavelength measurements for highly charged ions, hollow cathode lamps such as Fe-Ar, Cu-Fe-Mn, Co-Ni-Ne are commonly used for calibration purposes. Light from the calibration lamp is first collected and collimated by a lens which is then focused by a second lens into an optical fiber, see figure 3.3.1. The output end of the fiber directs the light onto a movable diffuse aluminum reflector positioned between the vacuum chamber window and the periscope box. When the calibration light is reflected from this plate, it blocks the light from the ion cloud, ensuring that the calibration light follows the exact same optical path outside the EBIT as the ion signal. This configuration is ideal for accurate wavelength calibration.

Grating

The three diffraction gratings employed have different groove densities; 150 grooves/mm, 1800 grooves/mm and 3600 grooves/mm, which contributes to the resolving power of the spectrometer. The main wavelengths for each of these grating are 500 nm, 400-800 nm and 200-400 nm, respectively. In this experiment, blazed gratings are employed which have an asymmetric groove profile with each groove acting as a reflecting surface defined by a blaze angle. Figure 3.3.2 illustrates the sawtooth-shaped groove profile of a blazed diffraction grating. This geometry concentrates most of the diffracted light into a selected diffraction order at the desired wavelength range, enhancing the grating's efficiency.

The grating equation provides the relationship between wavelength of the incident light and the angles at which constructive interference occurs for a diffraction grating. It is given by the equation [117]:

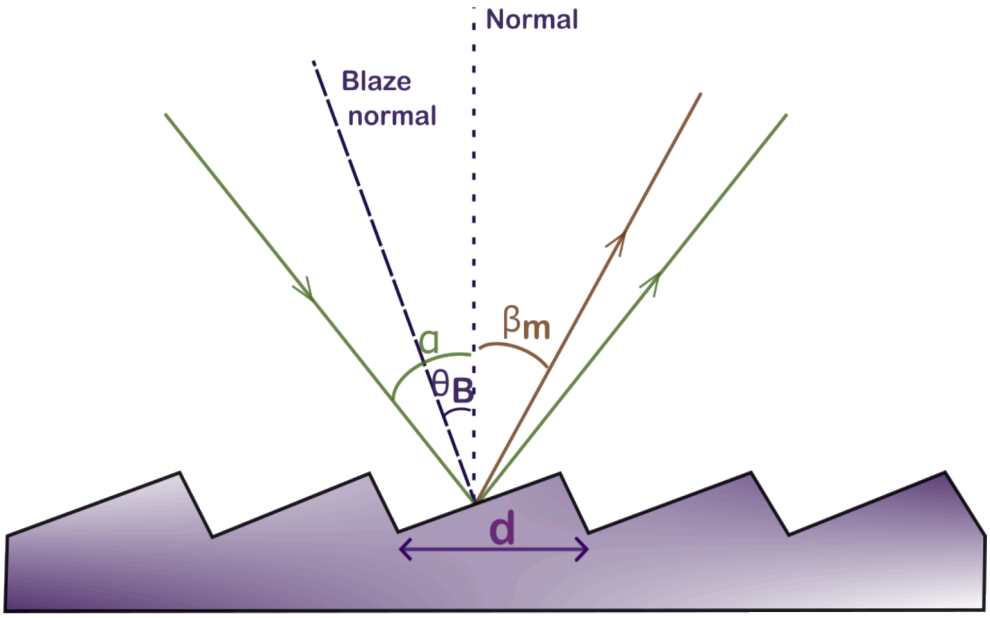

Figure 3.3.2: Schematic of a blazed grating. The angles of incidence α and diffraction β_m corresponds to the mth diffraction order. The blaze angle θ_B is defined as the angle between the groove surface normal and the grating normal.

$$m\lambda = d(\sin\,\alpha + \sin\,\beta_m) \tag{3.2}$$

Here m is the diffraction order, λ is the wavelength, d is the spacing of the grooves and α and β are the angle of incidence and diffraction, respectively. When the angle at which light strikes the grating is fixed, different wavelength are diffracted at different angles and this separation is referred to as dispersion. It determines how far apart the spectral components are spread on the detector. Differentiating the grating equation with respect to wavelength gives the angular dispersion of the grating:

$$\frac{d\beta}{d\lambda} = \frac{m}{d\,\cos\,\beta} \tag{3.3}$$

This equation indicates that the dispersion increases with diffraction order and decreases with groove spacing d.

The selected spectrometer and grating configuration are well suited for optical spectroscopy of highly charged ions, whose prominent transitions lie in the visible and near-ultraviolet spectral range. This setup has been successfully employed in previous experiments at the HD-EBIT for a variety of elements [36, 112, 115], demonstrating reliable detection of weak emission lines from highly charged ions. In the present work, the same configuration enabled optical spectroscopy of highly charged nickel ions (see

Section 7.1.3) and will be used for the planned measurements on highly charged californium ions.

4 Clock Setup: Mini-EBIT, Beam Line and Paul trap

Due to the high temperature of HCIs in an EBIT, performing clock measurements directly in this trap is challenging. Therefore, in the final clock set up, an EBIT is connected to a beam line for the transport of highly charged ions into a Paul trap for spectroscopy measurements. The EBIT used for the clock is not the HD-EBIT used for the initial spectroscopy of HCIs but a more compact variant known as the mini-EBIT, which was first developed in 2018 [118]. Despite sharing the fundamental working principles with larger EBITs like the HD-EBIT, the mini-EBIT differs considerably in its design and operational requirements. These differences arise from the need for portability, reduced size, and simplified infrastructure, making the mini-EBIT an attractive option for laboratories with space or budget constraints, or for specialized applications requiring mobility.

This chapter provides a brief description of the construction of the mini-EBIT, an overview of the beam line and the Paul trap, as well as a general introduction to the planned Cf clock setup.

4.1 Miniature Electron Beam Ion Trap

Following the development of the first micro EBIT by Khodja and Briand [119], various miniaturized EBITs have been developed. Unlike larger EBITs like the HD-EBIT, mini-EBITs are easy to construct, maintain and operate. They are compact and work at room-temperature. In 2018, a new class of EBIT was constructed at Max Planck Institute for Nuclear Physics (MPIK) [118] named the Heidelberg Compact EBIT (HC-EBIT), which provided better features and performance than the previous ones. In addition to its approximately 1 tesla magnetic field, the electron gun, collector and drift tube assembly were newly designed. The Birmingham EBIT follows the same design [120] as the HC-EBIT and its construction will be briefly discussed below.

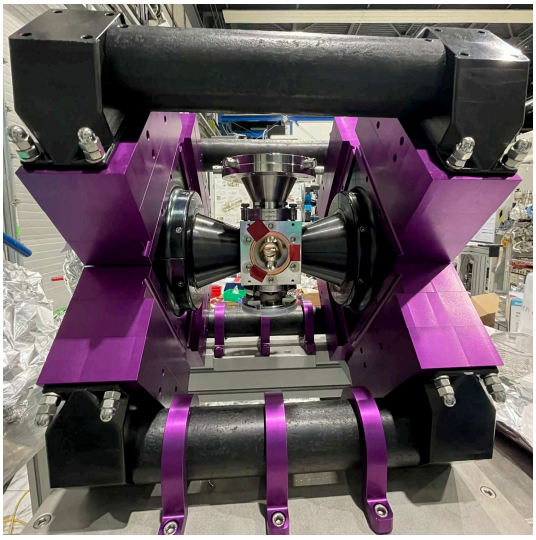

Figure 4.1.1: Birmingham EBIT during construction. The permanent magnets are placed inside the purple aluminum blocks. The yoke structure made of soft iron is colored black.

4.1.1 Mini-EBIT Magnetic Structure

In contrast to the HD-EBIT which uses superconducting Helmholtz coils for the magnetic field, a mini-EBIT uses 72 NdFeB permanent disk magnets, each with a diameter of 40 mm and a length of 30 mm and magnetized along the cylinder axis. Each magnet has a magnetic field strength of approximately 0.5 T. Eight arrays of magnets are arranged in 3×3 fashion separated by aluminum blocks. These magnets are placed on a yoke consisting of magnetic steel parts connected by four soft iron rods and two hollow conical pole soft iron parts. The yoke focuses the magnetic field towards the center of the trap and together with the magnets, approximately 0.85 T magnetic field density is reached. A picture of the Birmingham EBIT during construction is shown in figure 4.1.1.

4.1.2 Mini-EBIT Electron Gun

The working principle of the electron gun is the same as given in Section 3.1.1. A cross section of the Pierce-type electron gun [118] is shown in figure 4.1.2. The barium doped tungsten thermionic dispenser cathode is secured between two molybdenum pieces. All the metal parts used near the cathode: threaded rods, screws, and nuts, are made of molybdenum to withstand the high temperature from the cathode. Positioned along three alumina ceramic rods are the stainless steel base, the cathode assembly, the

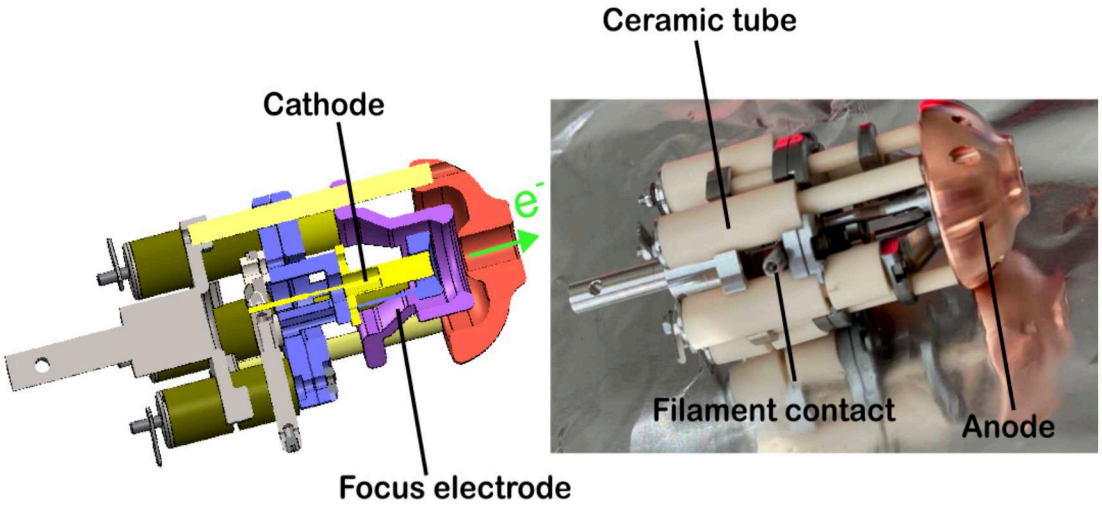

Figure 4.1.2: Cross-sectional CAD model (left) and photograph (right) of the Pierce-type electron gun used in the mini-EBIT. The electron beam is emitted from the cathode, controlled by the focus electrode, and accelerated through the anode towards the drift tube region.

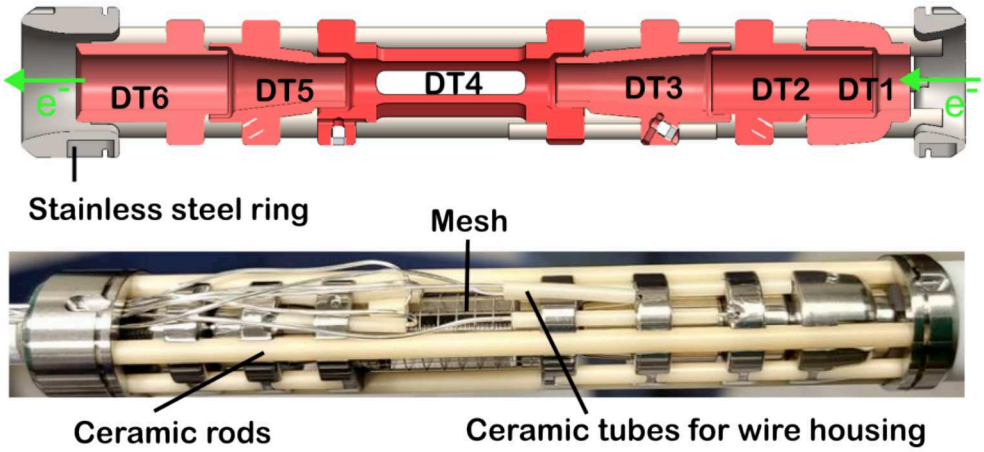

Figure 4.1.3: Cross-sectional CAD model (top) and photograph (bottom) of the mini-EBIT central region showing the six titanium drift tubes (DT1–DT6) aligned along the beam axis. The electron beam from the gun enters DT1 and propagates through to DT6 towards the collector.

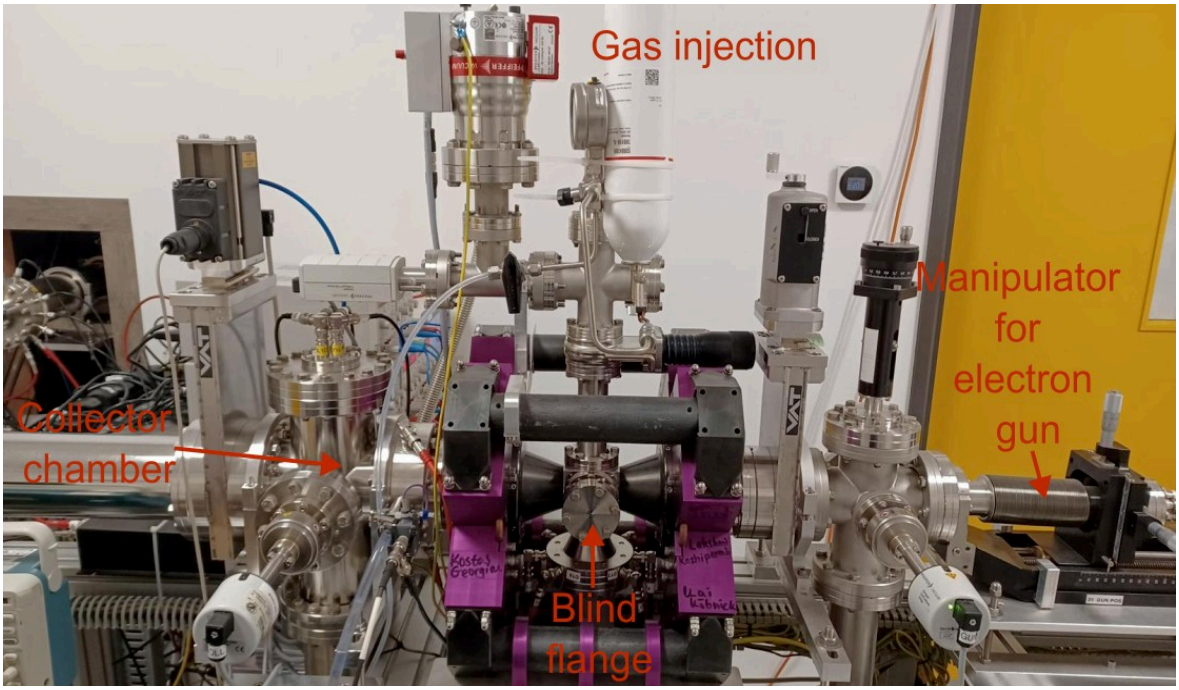

Figure 4.1.4: Photograph of the EBIT showing the main access ports and connected subsystems. The gas injection system is attached at the top port, while a lateral port with a blind flange is visible for future laser desorption integration. The electron gun manipulator is located on the right, and the collector chamber on the left. The turbomolecular pump connected to the bottom port is not visible.

molybdenum focus electrode and the copper anode electrode. There are ceramic spacers placed in different sections to avoid sparks, to electrically insulate and to provide correct distances. The electron gun is attached to a rod which in turn is connected to a manipulator. The bellow of the manipulator is contracted to the position so that the gun is inserted into one of the cones of the yoke.

4.1.3 Mini-EBIT Central Region

In contrast to HD-EBIT, the mini-EBITs features six drift tubes constructed from grade 5 titanium alloy, with the central drift tube designated DT4. These electrodes are secured by four ceramic rods and two stainless steel rings. Ceramic spacers with different lengths are positioned between electrodes to provide accurate distances. Silver coated copper wires are connected to each drift tubes to supply voltages. The wires are housed in hollow ceramic rods to prevent electrical discharge. The remaining exposed portion of the wire passes through ceramic beads and is connected to the feed-through flange. The drift tube assembly is shown in figure 4.1.3. The DT4 can be accessed

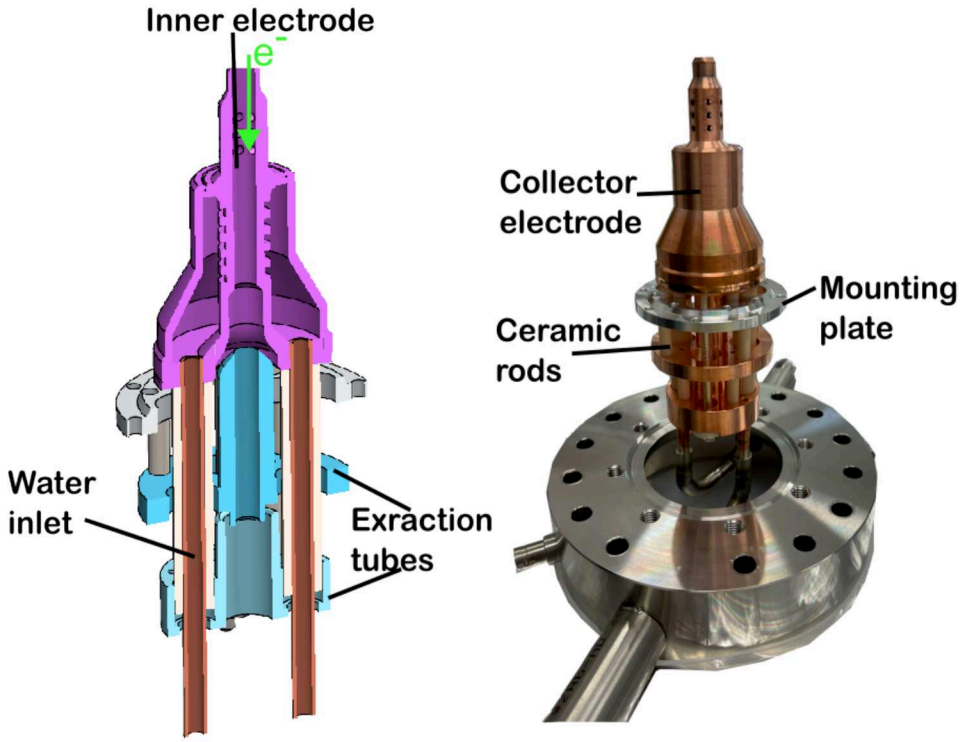

Figure 4.1.5: Cross-sectional CAD model (left) and photograph (right) of the mini-EBIT collector assembly, located downstream of DT6 along the electron beam axis. The water-cooled copper collector absorbs the incoming electron beam while the extractor electrodes enable efficient extraction of HCIs.

directly from four ports (see figure 4.1.4). The top port is connected with the gas injection system, bottom port with a T-piece to which a turbo molecular pump and a pressure gauge are attached. The remaining two ports will be used for the laser desorption system just as in the HD-EBIT. The potential applied to the drift tubes follows the same curve as the HD-EBIT given in 3.1.3.

4.1.4 Mini-EBIT Collector

The collector of the mini-EBIT is shown in figure 4.1.5. It is made of a hollow collector electrode, which encloses a space for water cooling. Electron-beam welded copper rods provide cooling water flow. Two additional extractor electrodes are placed outside the collector electrodes for ion extraction purposes. All the electrodes are made of copper. In contrast to HD-EBIT, the mini-EBIT collector does not have a suppressor electrode.

4.2 Highly Charged Ion Beam Line

Figure 4.3.1 shows a schematic overview of the experimental setup consisting of the EBIT, beam line and the Paul trap. The beam line components comprise Sikler lenses, a bender electrode, pulsed drift tubes (PDTs), a retarding field analyzer, and several microchannel plates (MCPs). Ions produced in the EBIT are extracted from the trap by applying a high potential to the DT4 electrode (see figure 4.1.3). These ions then pass through Sikler lenses, which are a specialized form of einzel lenses featuring grounded outer and a central electrode segmented into four parts. This design allows not only for focusing and steering of the ion beam but also for selecting specific time windows to extract ions of desired charge states.

The selected ions are directed through a double-focusing, electrostatic 90° bender [121], which is followed by an additional Sikler lens. Subsequently, the ions enter a PDT, composed of two cylindrical tubes with serrated ends and bound by Sikler lenses on both sides. A gradient potential that is switched in time across the PDT serves to bunch and decelerate the ions.

For diagnostic purposes, an MCP coupled with a retarding field analyzer is placed after the PDT. By biasing the retarding field analyzer, only ions with kinetic energies exceeding the product of their charge and the applied potential are allowed to pass through. For a detailed explanation of the beam line, refer to [118, 122].

4.3 Paul Trap

The ions ultimately enter the Paul trap (PT) after passing through two einzel lenses and a mirror electrode. A comprehensive description of the Paul trap can be found in [123]. The PT is biased to a potential slightly below the residual kinetic energy of the ions to facilitate their capture. Within the trap, a pre-existing ion cloud composed of ions with a charge to mass ratio similar to that of the HCIs is confined. For definiteness, the ion cloud will be referred to as Be^+ ions here, though other ion species can also be used.

To ensure efficient injection, the first mirror electrode (MR1) is initially set to a potential lower than the kinetic energy of the incoming HCIs. Immediately after their entry, the potential on MR1 is rapidly increased, preventing the ions from escaping the trap. The HCIs then traverse the Be^+ ion cloud and are reflected by the second mirror electrode (MR2) located at the opposite end of the Paul trap. This reflection

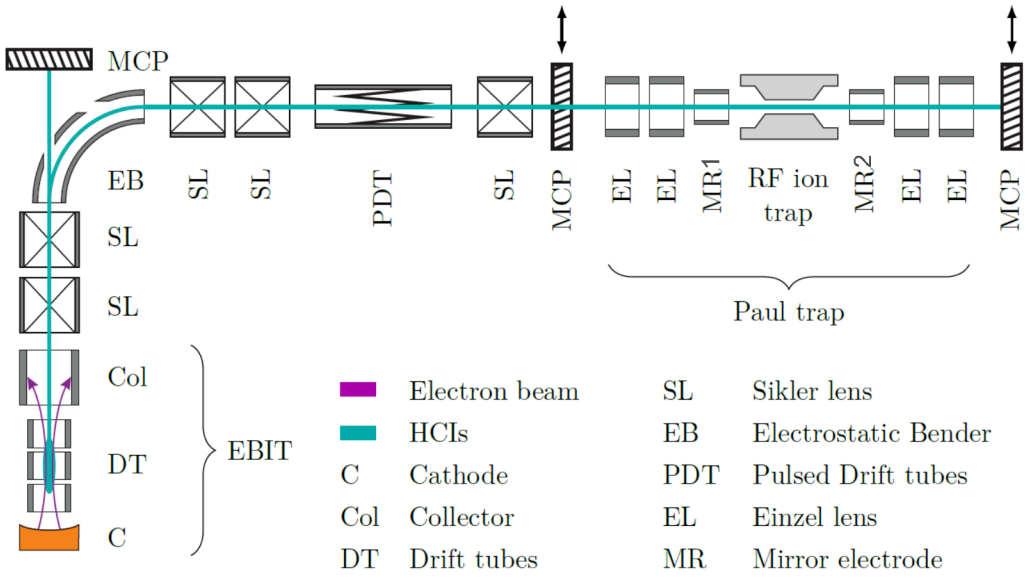

Figure 4.3.1: Schematic of EBIT, beam line and Paul trap, taken from [123].

process continues as the HCIs oscillate back and forth between MR1 and MR2. During these oscillations, the HCIs gradually lose energy through interactions with the Be^+ ion cloud, get confined within the trap and eventually co-crystallize in the Be^+ crystal via sympathetic cooling.

The Be^+ cloud is heated by modulating the radio-frequency (RF) drive of the trap at a frequency near the secular resonance of the Be^+ ions. As a result, ions are successively removed from the trap until only a single Be^+ ion remains together with the HCI. A highly stable laser is then used to probe a narrow optical transition of the HCI, which defines the clock's reference frequency. Since HCIs typically lack accessible transitions for direct detection, quantum logic spectroscopy is used [124, 125]. Here, the HCI's internal state is mapped onto the shared motion of the two-ion crystal and can be subsequently read out via the logic ion. The laser is locked to the HCI transition, and its frequency is measured with an optical frequency comb, enabling extremely accurate timekeeping with fractional uncertainties approaching 10^{-18} [126] or even 10^{-19} [127]. Further details about the clock setup can be found in [118]. The proposed clock configuration is modeled after an existing setup, as shown in figure 4.3.2.

For the Birmingham experiment, a mini-EBIT and beam line, both fabricated at MPIK, were transferred to the University of Birmingham. The Paul trap, which has been constructed at Physikalisch-Technische Bundesanstalt (PTB), is currently being used to perform measurements with a calcium ion cloud. Additionally, highly charged ions of xenon are being trapped [120]. The remaining components of the clock setup are still

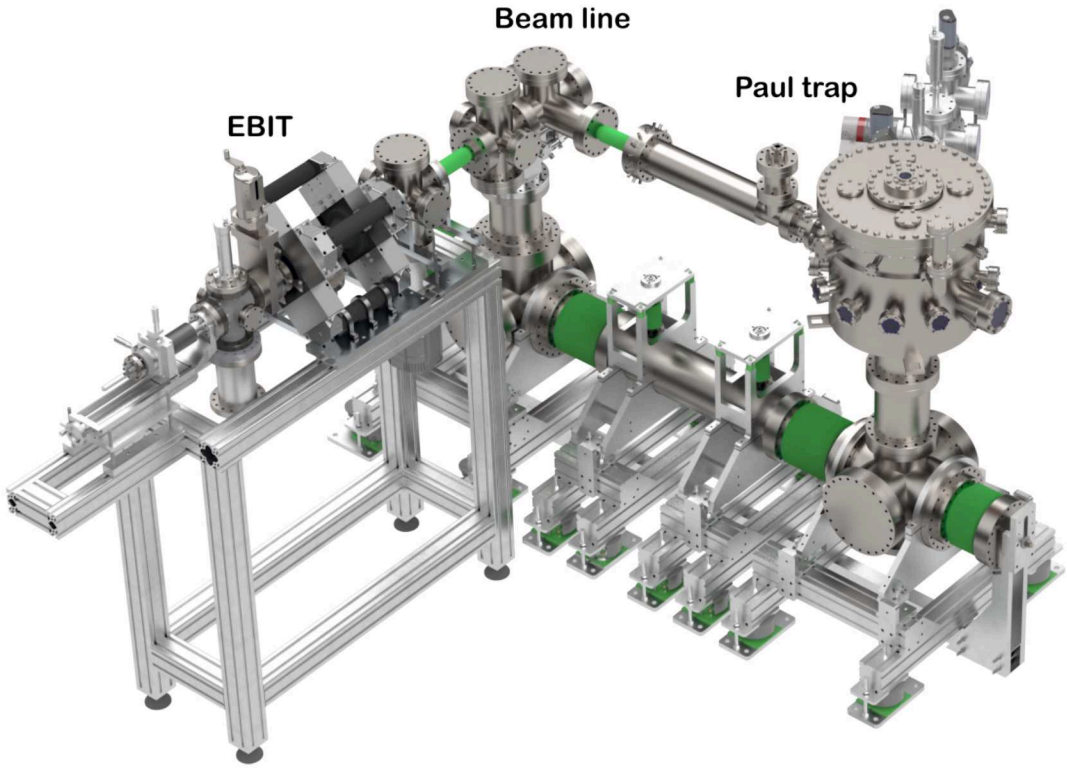

Figure 4.3.2: Overview of the HCI clock setup. Adapted from [123].

under development. The ultimate goal is to integrate this system with other precision clocks in the UK network (QSNET) to perform comparative frequency measurements of clock transitions, aiming to detect potential variations in fundamental constants.

5 Development of Injection System for Rare Metals

Due to radiation safety constraints, laboratory experiments with radioactive elements are typically limited to material quantities in the nanogram range. At such low amounts, conventional injection techniques, such as the gas injection method described in Section 3.2, are no longer suitable, as they rely on a continuous and comparatively large material supply. Consequently, an alternative injection technique with high efficiency and minimal material loss is required for rare and radioactive elements. The injection of rare elements has been implemented previously [128] for the injection of holmium into a miniature EBIT. For holmium, a laser-induced desorption technique is employed to release atoms from a sample holder containing the radioactive material by irradiating it with laser pulses. The sample is placed directly inside the drift tube and once irradiated by pulsed laser light, the corresponding atoms and some ions released into the trap region.

The design and implementation of such an injection system for the HD-EBIT, however, present several technical challenges. In contrast to miniature EBITs, the HD-EBIT is a significantly larger and more complex experimental setup, in which direct access to the trap region is restricted. In addition, direct visual access to the trap region is prevented by the presence of temperature shields, and the inner vacuum chamber must be maintained at cryogenic temperatures to ensure proper operation of the superconducting magnets. As a result, heat transfer from the outer room-temperature environment must be carefully controlled. The following sections describe how these challenges were addressed.

Since the target must be positioned very close to the trap center inside DT9 (see figure 3.1.3), the injection system comprises a target holder containing the radioactive material, a manipulator system for the holder, and an optical setup for laser-induced desorption. Once the laser pulse strikes the target surface, neutral atoms and ions are released into the trap region, where they are subsequently ionized to highly charged states by the EBIT electron beam. Owing to the placement of the target holder directly

inside the drift tube assembly, the laser desorption process occurs in close proximity to the electron beam, enabling highly efficient injection of the released target material into the trapping and ionization region.

5.1 Californium Target Implementation

For californium, a rare and radioactive actinide element, laser-induced desorption [128] is used to release neutral atoms from a solid target into the EBIT for subsequent ionization. The 33 mm long titanium sample holder holds the target which has been deposited using the Drop on Demand (DoD) technique [129]. The DoD technique allows precise placement droplets of the desired element into a tiny, specific target area, ensuring controlled utilization of the radioactive sample [130].

Titanium was selected as the material for the sample holders due to several reasons. It is non magnetic, mechanically robust and is a relatively light element so Ti ions produced during the experiment reach only low charge states compared to the much heavier Cf ions. During laser-induced desorption, not only californium atoms but also a small amount of titanium from the sample holder is released and subsequently ionized in the trap center. In the EBIT, low charge state titanium ions experience weaker confinement and readily escape, resulting in selective evaporative cooling [131]. This loss of weakly confined titanium ions removes energy from the ion ensemble and favors the accumulation of highly charged californium ions.

For this experiment, the target holder has a 0.5 mm diameter recess at the tip where the sample is dispensed, see figure 5.1.2. The holders were positioned upside down in a polyethylene storage block containing holes with a diameter of 3 mm (see figure 5.1.1), ensuring that the tip remained suspended without contacting the bottom surface or the surrounding packaging material. This configuration protected the tip from mechanical damage during transport and, after deposition, prevented the radioactive ^{249}Cf target from touching any surfaces or being handled directly during removal. The storage block was placed in a plastic container and secured with sponges to prevent movement during transport. Five titanium sample holders were sent to the Nuclear Chemistry institute of the Department of Chemistry at Johannes Gutenberg University Mainz, where ^{249}Cf was deposited onto the holders using the DoD technique.

The isotope ^{249}Cf, which is one of the more stable isotopes with a half-life of 351 years, will be used for this experiment. To calculate the number of atoms in 1 g of californium:

$$\text{Number of atoms} = \text{number of moles} \times \text{Avogadro's number} \tag{5.1}$$

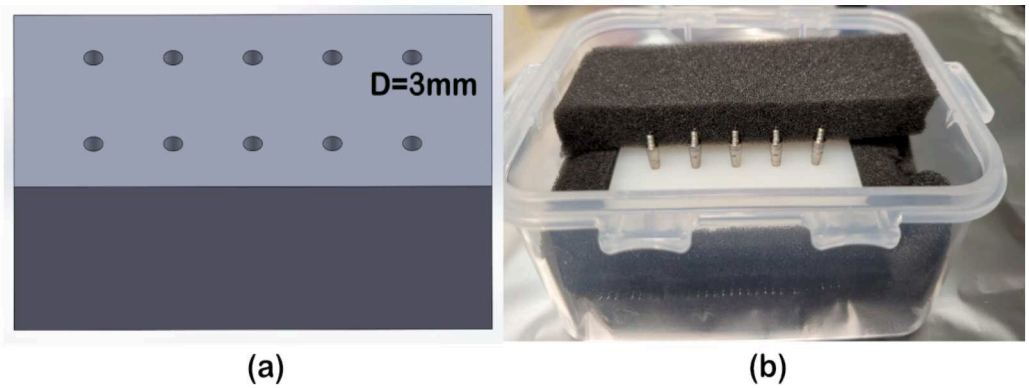

Figure 5.1.1: Storage and transport configuration of the Cf target holders. (a) CAD model of the polyethylene storage block. (b) Transport container with the storage block secured by sponges and five target holders in place.

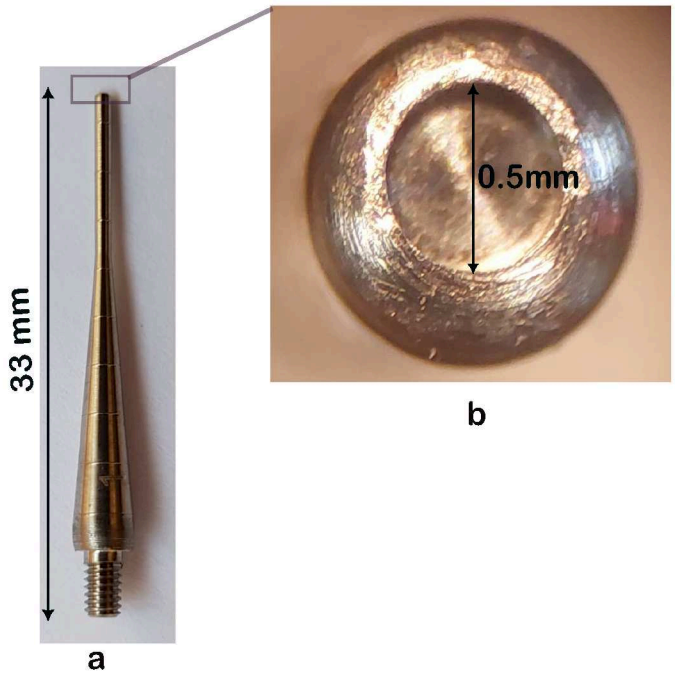

Figure 5.1.2: Titanium target holder and recessed tip for Cf deposition. (a) 33mm long target holder. (b) Top view of the tip of the target holder with the 0.5 mm recess where the 6.6 ng of ^{249}Cf is dispensed by the DoD method.

$$\text{Number of moles} = \frac{\text{given mass}}{\text{molar mass}} = \frac{1\text{ g}}{249\text{ g}} = 0.004016\text{ mol} \tag{5.2}$$

Therefore, number of atoms in 1 g = 0.004016 mol$\times 6.022 \times 10^{23}$atoms mol^{-1} = 2.42$\times$ 10^{21} atoms.

Thus, the number of atoms in 1 ng of Cf is $= 2.42 \times 10^{21} \times 10^{-9} = 2.42 \times 10^{12}$ atoms.

The rate of radioactive decay is given by the equation [132]:

$$\frac{dN}{dt} = -\lambda N \tag{5.3}$$

where N is the number of radioactive nuclei and λ is the decay constant. The radioactive decay half-life is defined by:

$$t_{\frac{1}{2}} = \frac{\ln 2}{\lambda} \tag{5.4}$$

With these equations the activity R can be determined by:

$$R = \ln 2 \frac{N}{t_{\frac{1}{2}}} \tag{5.5}$$

The activity R in 1 ng of ^{249}Cf is then 4.778×10^9 decays per year. Dividing it by 3.16×10^7 seconds gives the activity in becquerel, which is 151 Bq. For the planned Cf spectroscopy measurements, each target holder contains approximately 1000 Bq, corresponding to about 1.6×10^{13} atoms or roughly 6.6 ng of ^{249}Cf. For comparison, the human body contains approximately 0.017 g of the naturally occurring radioactive isotope ^{40}K, corresponding to an activity of the order of 4×10^3 Bq [133].

5.2 Manipulator System for the Sample Holder

The sample holder is screwed onto a copper rod which in turn is attached to a fiberglass aka Glasfaserverstärkter Kunststoff (GFK) hollow rod which has an outer diameter of 10 mm (see figure 5.2.1). A current is supplied to the holder to maintain it at the potential of the drift tube. The holder is mechanically attached to the copper rod, which is connected to a wire that passes through the GFK rod and ultimately reaches the feed-through flange at the bottom, where it is connected to a power supply. The feed-through flange is mounted on a UHV Precision XYZ Manipulator (KPM),

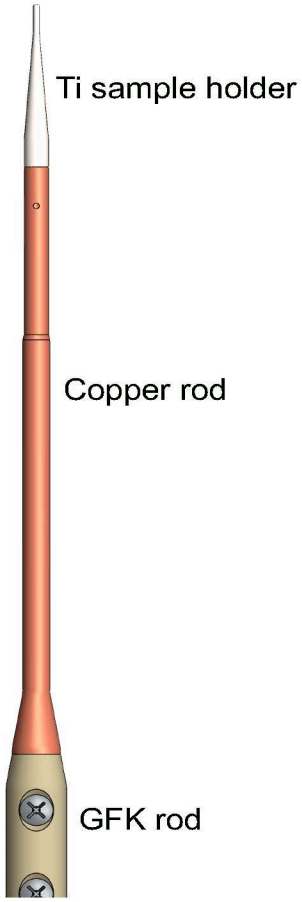

Figure 5.2.1: Sample holder mounting assembly with copper support rod and GFK insulation rod.

which is capable of translating up to 600 mm along the Z-axis. In the X and Y directions, the manipulator has a range of motion of 25 mm. The present rod assembly design follows the laser-induced desorption model developed for the 'free electron laser Hamburg'(FLASH)-EBIT by [134] and is implemented here for the HD-EBIT.

The complete rod assembly passes through two apertures, one at the 50 K and one at the 4 K shield, see Section 3.1.2. The 50 K aperture is a hollow aluminum cylinder with 10.5 mm wall thickness which is screwed on to two aluminum half moon plates that are attached to the 50 K shield, see figure 5.2.2. The inner diameter of the aperture is 15 mm. The 4 K aperture is a 23 mm long aluminum cylinder with 0.5 mm thickness and has an inner diameter of 10 mm. A polyether ether ketone (PEEK) hollow screw with an umbrella head with inner threading is attached to the previously installed stainless steel plate with a PEEK nut and the 4 K aluminum cylinder is screwed to the PEEK screw, see figure 5.2.3.

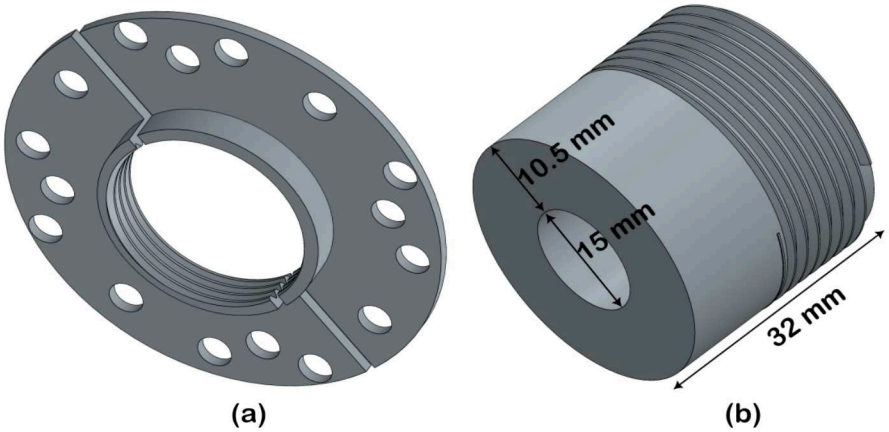

Figure 5.2.2: 50 K shield aperture components. (a) The half moon plates made of aluminum which are attached to the 50 K shield of the HD-EBIT. (b) The aluminum hollow cylinder that is screwed to the half moon plates. Together these form the aperture in the 50 K shield.

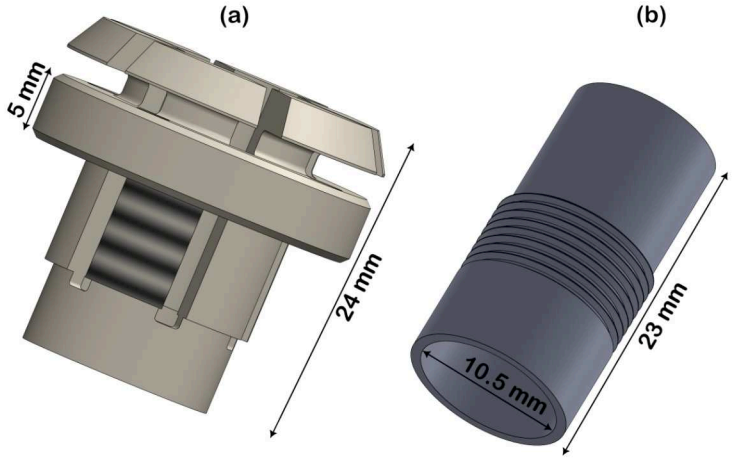

Figure 5.2.3: 4 K shield aperture components. (a) The PEEK umbrella headed screw secured with a PEEK nut onto the plate which is attached to the 4 K shield of HD-EBIT. (b) The aluminum hollow cylinder is the aperture with 10 mm inner diameter that is secured into the PEEK umbrella headed screw.

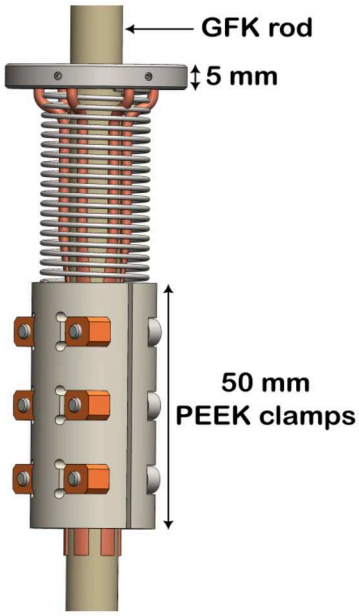

Figure 5.2.4: Thermalization components attached to the rod assembly. A 5 mm thick aluminum plate is attached to the fiberglass rod with a PEEK clamp. Copper braids are attached to the plate with screws and the PEEK clamp secures them to the rod. The spring is simply placed on the clamp which then compensates for the contraction in cold temperature and reliably presses the aluminum plate against the HD-EBIT 50 K shield to ensure thermalization.

To enhance heat transfer efficiency as the rod transitions from room-temperature to 4 K, an aluminum plate, affixed with six copper braids each 12 cm in length, is secured to the rod using a stainless steel spring with 2 mm wire thickness (relaxed length 60 mm and compressed length 37 mm) and a PEEK clamp (see figure 5.2.4). The clamp is affixed to the manipulator rod using non-magnetic stainless steel screws, and due to the contraction of PEEK at low temperatures, copper nuts are employed. The spring is compressed when the aluminum plate makes contact with the 50 K aperture of HD-EBIT and subsequently relaxes slightly as the materials contract in the cold environment. The distance from the bottom of the PEEK clamp to the target holder tip is 331 mm.

The six-way cross beneath the valve at the bottom of HD-EBIT serves multiple functions (see figure 5.2.5), most notably enabling the target to be swapped without requiring a complete warm-up of the EBIT, otherwise it would take weeks for the system to become operational again. To perform the target swap, the rod must first be retracted until the target holder is positioned near the center of the cross. The valve beneath the EBIT is then closed, isolating the EBIT from the injection system. At this point,

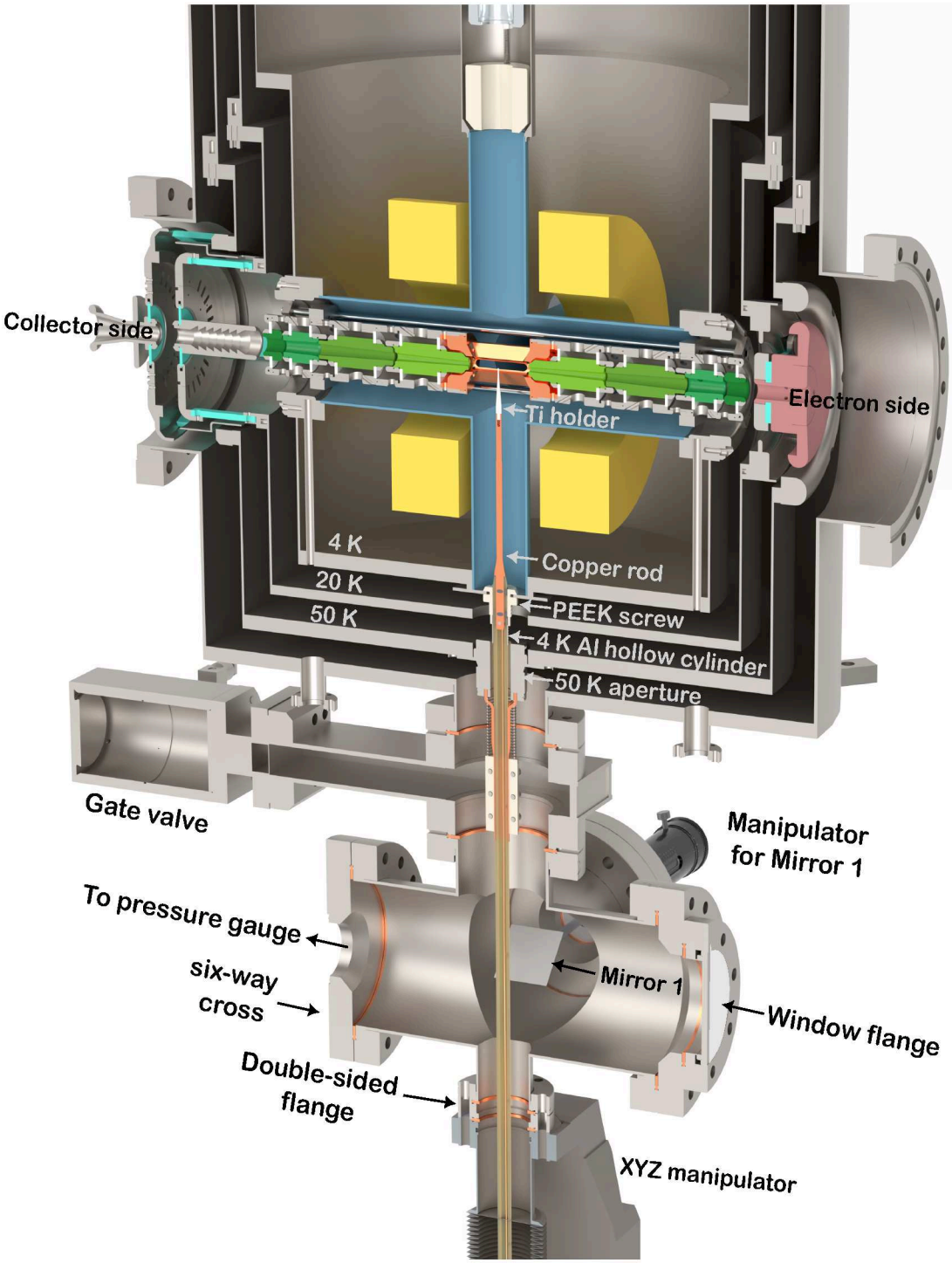

Figure 5.2.5: The manipulator-target system for the HD-EBIT, showing the locations of the parts highlighted in figures 5.2.1-5.2.4. Figure illustrates the titanium target holder at the middle of the drift tube. More pictures of HD-EBIT can be found in the Appendix B.

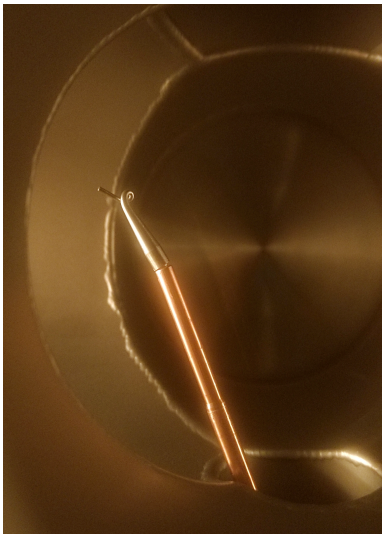

Figure 5.2.6: Twisted and bent target holder resulting from failed insertion through the apertures without visibility of its position.

the injection system is brought to atmospheric pressure. One of the window flanges (marked in figure 5.2.5) can then be removed, allowing the target holder to be easily swapped. Following the swap, the injection system is sealed off, pumped down, and within approximately 24 hours, the system is expected to be ready to resume operation.

Additionally, the six-way cross has the following significant parts attached. The valve and the manipulator are attached to the top and bottom ports, respectively. A CF100 T-piece is mounted onto one of the ports, with a vacuum pump connected to the tail end and a blind flange sealed at the arm end (see figure 5.2.8). Two opposite ports of the cross are occupied by a pressure gauge and a window flange (see figure 5.2.5). In a preliminary design, the remaining port was a blind flange. However, when the Ti holder was first inserted into the EBIT, it hit one of the apertures and experienced significant deformation resulting in severe bending, see figure 5.2.6. This led to the replacement of the blind flange with the addition of a square mirror (Mirror 1) of dimension 50.8 mm. This Mirror 1 is positioned at a 45 degree angle on a linear stage manipulator. The opposite port of the Mirror 1 which initially had the blind flange (attached to the CF100 T-piece) was replaced with a window flange. With Mirror 1, the 50 K aperture could be seen very clearly.

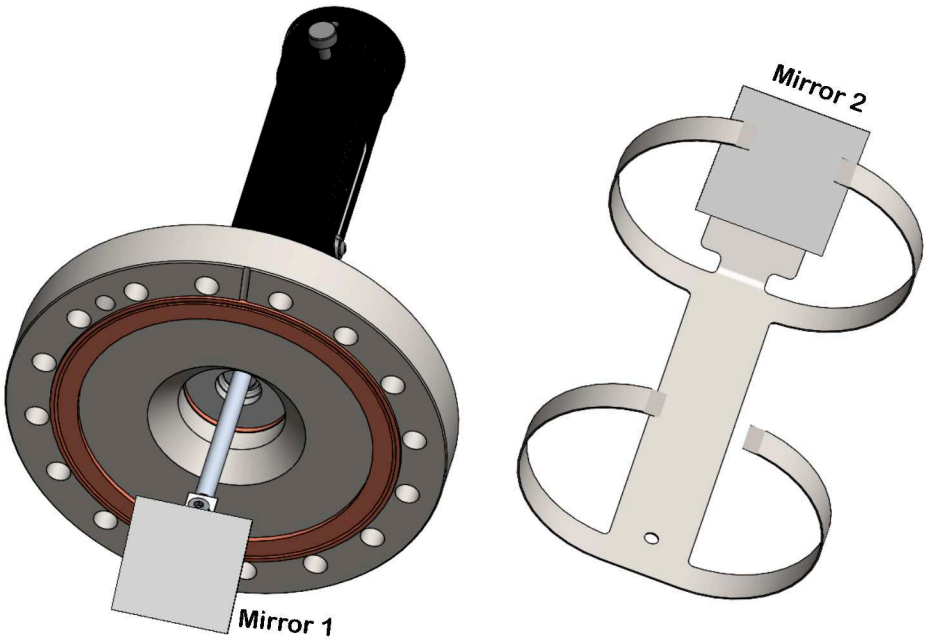

Figure 5.2.7: CAD model arrangement of Mirror 1 and Mirror 2 used to provide visual guidance during target holder insertion through the 50 K aperture.

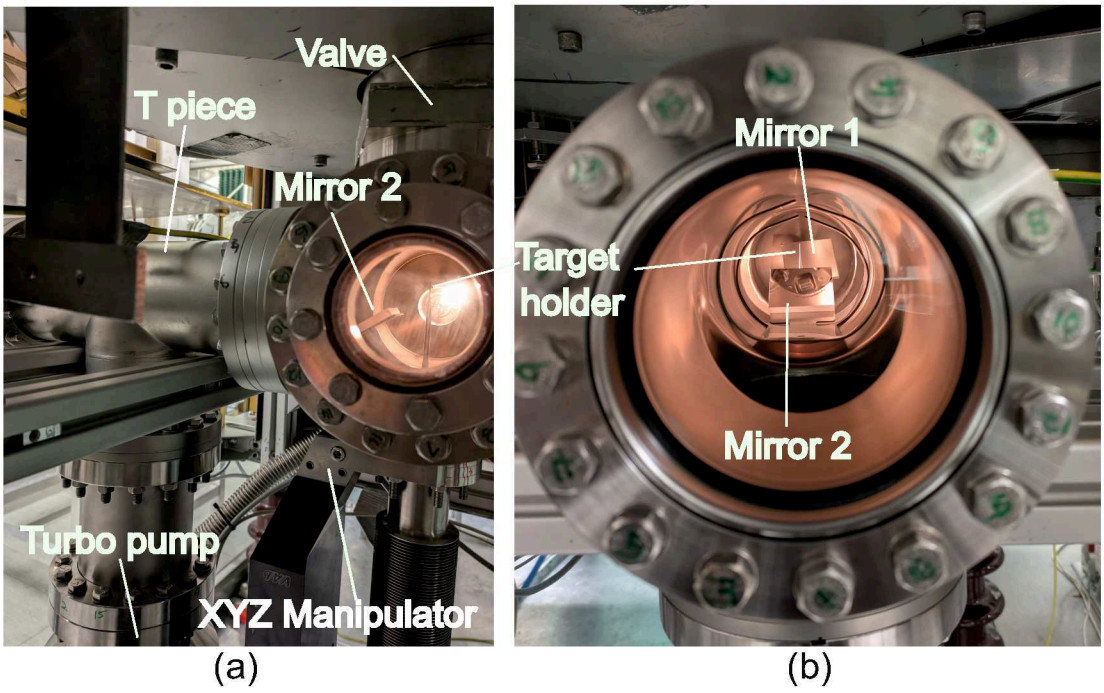

Figure 5.2.8: Mirror arrangement on the six-way cross for monitoring the valve position. (a) Mirror 2 mounted on the left port of the six-way cross at the location of the T-piece. (b) Reflected view of the closed valve observed using Mirror 2. Mirror 1 is mounted on the port opposite to Mirror 2.

Testing the Setup with an Empty Holder

A telescope was positioned opposite to Mirror 1 and 1.5 meters away from the six-way cross to provide closer observation during the insertion of the holder. The holder must pass through two apertures: the first at the 50 K shield and the second at the 4 K shield. During the insertion process, the view of Mirror 1 was obstructed by the spring and PEEK clamp assembly (figure 5.2.4), leading to a disruption in visibility. To resolve this, another square mirror of dimension 50.8 mm (Mirror 2) was positioned at the front of the rod to prevent further interference and ensure an unobstructed view of the 50 K aperture.

Mirror 2 is mounted on a stainless steel mirror mount installed inside the arm of the six-way cross where the T-piece is connected (see figure 5.2.8). The mirror is glued onto a square mounting plate bent at 45°, allowing visual monitoring of the 50 K aperture during insertion of the target holder (see figure 5.2.7). The mounting plate is connected to a central support strip with two circular retaining rings that match the inner diameter of the six-way cross, ensuring stable positioning of the mirror mount inside the cross.

Using Mirror 2, it was observed that the target holder was significantly off-center, indicating that the rod required a slight angular correction to pass through the 50 K aperture. After the fine adjustments of the telescope alignment, the tip of the target holder was estimated to be approximately 10 mm displaced from the center of the 50 K aperture. The XYZ manipulator could not fully compensate for this offset, as its adjustment range had reached its mechanical limit. To correct this misalignment, a double-sided flange was added to the top of the XYZ manipulator (see figure 5.2.5). This CF 40 flange was machined with a 2-degree bevel across its sealing face, introducing a small tilt to the manipulator and redirecting the holder rod toward the center of the 50 K aperture.. The distance from the beginning of the 50 K aperture to the face of the top flange of the manipulator is 300 mm.

$$\theta = \tan^{-1} \frac{10}{300}$$

Since the 50 K and 4 K apertures are separated only by a few centimeters, correct alignment through the 50 K aperture would guarantee clearance through the 4 K aperture as well.

To verify whether the target holder was aligned with the center of DT9 (refer figure 3.1.3), a second telescope was positioned at a viewing window on the beamline,

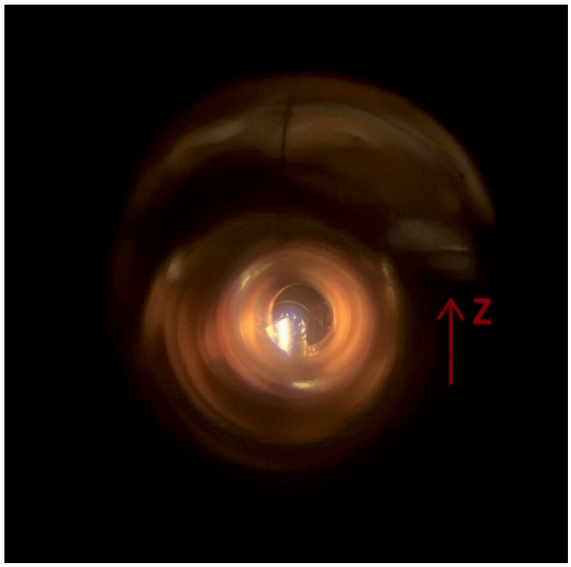

Figure 5.2.9: Photograph of the successful insertion of the Ti target holder into HD-EBIT looking along the axis of the EBIT. With the manipulator located at the bottom, the tip's position can be adjusted along the X,Y, and Z axes. At 79 mm in the Z direction, the tip is about at the center of the drift tube.

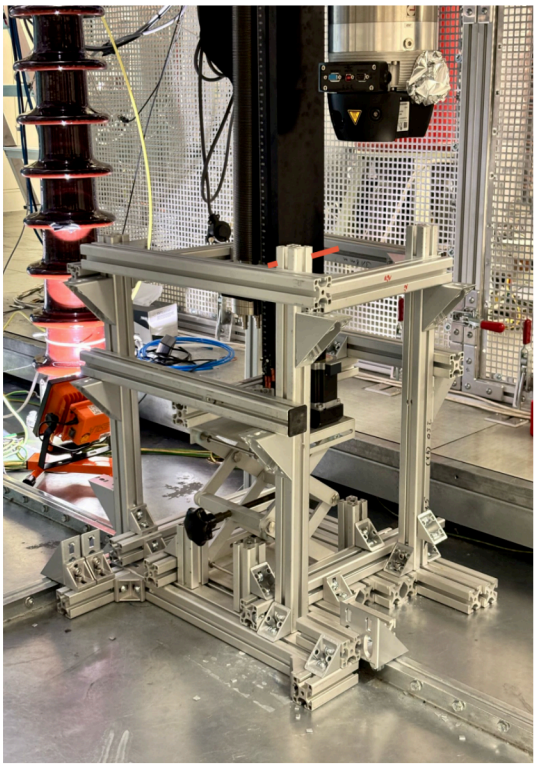

Figure 5.2.10: Aluminum profile support setup for the manipulator with a double scissor jack with the proposed aluminum rod position marked in red.

allowing observation along the EBIT axis through the collector and into the drift tube. With the 2-degree double flange in place, the target holder successfully passed through the 50 K aperture. However, only a portion of the holder was visible looking along the EBIT axis indicating that it was not centered within DT9. Adjusting the stages on the manipulator intended for positional alignment didn't produce any displacement of the holder. On the other hand, when the manipulator was gently pushed by hand, reducing the tilt angle, the holder moved toward the center of DT9. Therefore, the bevel angle was reduced from 2 degree to 1 degree. This adjustment provided sufficient angular correction, allowing the holder to be inserted smoothly and centered within the DT9.

Once the target holder was positioned in the center of DT9, an aluminum profile support frame was installed to provide mechanical support for the manipulator, as the injection system is suspended from the flange of the EBIT outer shield. Without proper support, this setup could cause damage. This arrangement is illustrated in figure 5.2.10. The double scissor jack in the figure was initially placed below the manipulator to provide primary support. An additional aluminum rod will be attached to the manipulator for further reinforcement; while not shown in the figure, its intended position is indicated by the red line.

When the target holder was aligned with the center of drift tube 9, the manipulator stage scale readings were 12.64 mm and 11.78 mm on the two lateral adjustment stages, and 79 mm on the insertion (z) stage (see Fig. 5.2.9). These values correspond to the manipulator scale readings required for reproducible alignment.

5.3 Preliminary Optical Setup for Laser Desorption

The second part of the injection system is the laser setup. The laser used for this configuration is a 'Quantel Big Sky Laser Ultra' with laser beam diameter of 2.5 mm and a wavelength of 532 nm. Due to the large size of the HD-EBIT, the laser beam must travel a relatively long path. Most of the optical components are therefore placed outside the EBIT even though the available space is constrained. In addition, vibrations from the cold head of the cryocooler located at the top of the EBIT present further challenges. To mitigate these issues, the optical components for focusing the laser are mounted on a 50 mm thick optical breadboard with dimensions 500 mm $\times$ 380 mm as shown in figure 5.3.1.

To achieve the required beam conditioning and final micron-scale beam spot size at

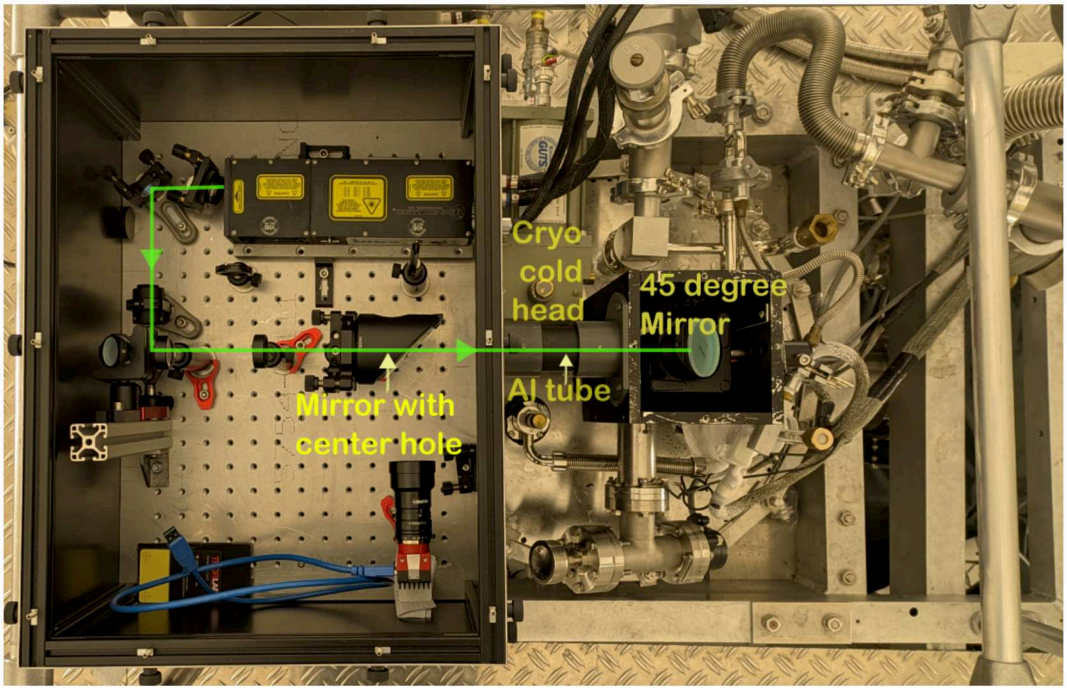

Figure 5.3.1: The top view of the HD-EBIT. To the left is the larger box where the 50 mm optical breadboard is placed, covered by black anodized aluminum plates. To the right is the small black cage where the 45 degree mirror and the 350 mm focal length lens are placed. The laser light travels through a small black aluminum tube for safety. The cold head of the cryogenic system of HD-EBIT is visible near this tube.

the target, the laser beam is expanded and focused using a sequence of lenses (see figure 5.3.2). The beam path is as follows: The 2.5 mm diameter laser beam first reflects from a mirror at 90 degrees into a 3X beam expander. The expanded 7.5 mm beam then passes through two lenses with focal lengths of 35 mm and 50 mm, increasing the beam diameter to 10.7 mm, according to

$$\frac{d^1}{d^2} = \frac{f^1}{f^2} \tag{5.6}$$

with $d^1 = 7.5$ mm, $d^2 = 10.7$ mm, $f^1 = 35$ mm, and $f^2 = 50$ mm.

The enlarged beam then passes through a 45 degree mirror with a central hole and subsequently hits another 45 degree mirror which directs the beam towards a 350 mm focal length lens. This produces a beam waist of about 22.1 µm on its focal plane where an aperture is located. The small waist, when collimated by another 200 mm focal length lens becomes approximately 6.12 mm. After passing through another lens of 200 mm focal length, the collimated beam is re-focused onto the target with a beam waist size of 22.1 µm. The beam waist of a collimated beam focused by a lens can be calculated by the equation [135]:

$$2w_0 = \frac{4M^2\lambda f}{\pi D} \tag{5.7}$$

where M^2 is the beam quality factor (taken as 1 for an ideal Gaussian beam), λ is the wavelength, D is the collimated beam diameter at the lens with focal length f. This expression gives the focused spot diameter defined at the $1/e^2$ intensity level of the Gaussian beam.

The last 45 degree mirror and the 350 mm lens are placed in a block which is placed on the top of the window flange of the EBIT. This can be seen in the figure 5.3.1. A black anodized aluminum tube with a diameter of 40 mm connects the two optical blocks, enclosing the beam path and preventing exposure to stray laser light.

Since the lenses along with the aperture must be placed inside the HD-EBIT vacuum system, they are mounted in holders connected to the 50 K shield (see figure 5.3.3). Each holder consists of two parts: a hollow cylinder that houses the lens, and a second, smaller cylinder placed on top to prevent the lens from shifting. Both lens holders are connected to three titanium rods using six nuts. At the top of this assembly, an aluminum flanged hollow cylinder (see figure 5.3.3), which serves as the aperture, is attached to the first lens holder via three PEEK rods.

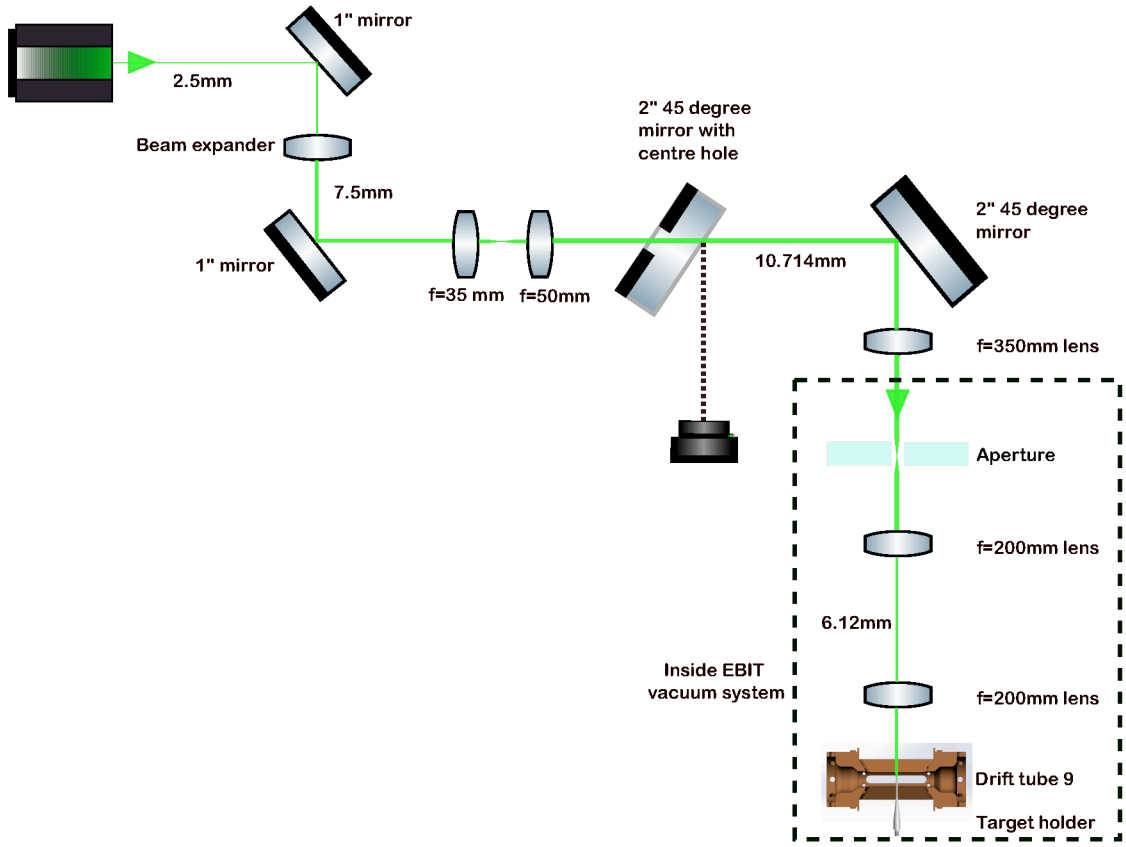

Figure 5.3.2: The optical path of the 532 nm green ablation laser beam of the injection system is shown here. The diameter of the beam changes when traveling through different optical components which is illustrated here. The camera images the tip of the target holder when the laser beam hits it.

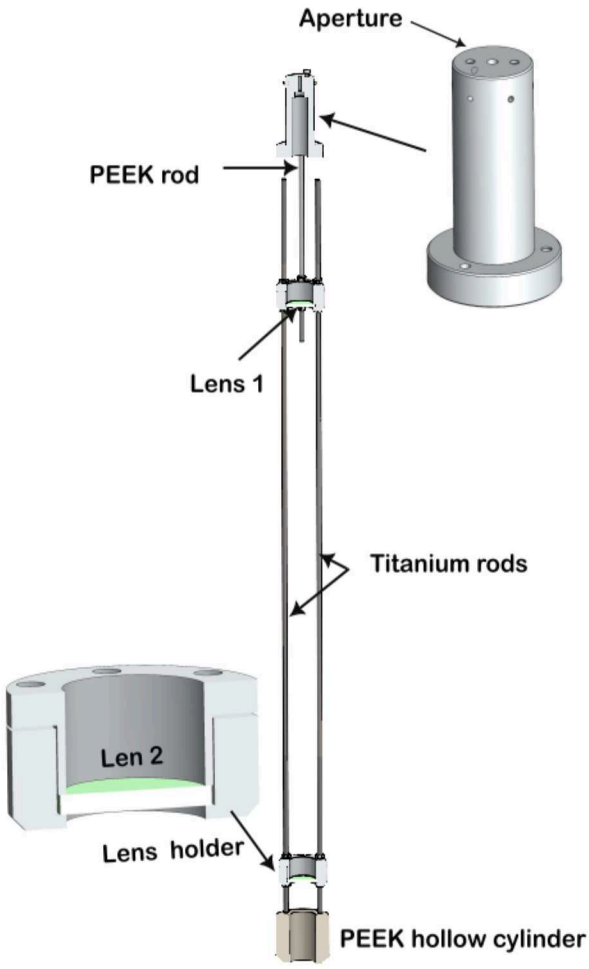

Figure 5.3.3: The figure shows the lens holder assembly. One-inch lenses with a focal length of 200 mm are placed in lens holders attached to titanium rods. At the top is the aperture, formed by the aluminum flanged hollow cylinder. The bottom PEEK hollow cylinder was later removed for easy insertion.

At the bottom, there is a PEEK hollow cylinder with a trapezoidal taper cut into part of its length. This cylinder is connected by nuts only at the bottom, allowing it to move upwards along the titanium rods. Its purpose is to facilitate the smooth insertion of the entire lens holder assembly into the inner vacuum chamber of HD-EBIT. Additionally, it ensures the assembly remains properly aligned and does not tilt in any direction (see figure 5.3.3). However, during the actual insertion of the lens holder assembly, this cylinder impeded the process and was therefore removed to simplify assembly.

The top surface of the flanged cylinder contains a 3.4 mm aperture, which is placed at the focal plane of the first lens in the vacuum chamber (Lens 1 in figure 5.3.3). Lens 1, with a focal length of 200 mm, is therefore positioned 200 mm below this aperture, such that the light emerging from the aperture is collimated after passing through Lens 1. The collimated beam then propagates to a second lens (Lens 2 in figure 5.3.3) located approximately 500 mm below the first. The Lens 2, also with a focal length of 200 mm, focuses the beam onto the target holder, which is positioned 200 mm beyond the lens at the center of DT9.

To verify that the laser beam hits the tip of the target holder, a camera is placed in the optical block. In figure 5.3.2, the lower 200 mm lens captures the image of the target holder, collimates it and sends the collimated image upwards to the upper 200 mm lens. This lens focuses the image onto the plane of the aperture center. The image then passes through the 350 mm lens, which collimates it again and directs it to the camera objective (100 mm focal length), which forms the final image on the camera sensor.

With the current optical configuration, however, the top-view image of the target holder cannot be clearly observed on the camera sensor. The illumination in the trap region is limited, and the small aperture diameter of 3.4 mm in the lens holder assembly further restricts the amount of transmitted light. As a result, the camera cannot reliably resolve the position of the target tip. Therefore, it is not possible to verify whether the desorption laser beam is accurately striking the target surface. Since precise alignment between the laser and the target is essential for controlled laser desorption, further improvement of the illumination and imaging system is required before the injection setup can be fully commissioned.

For the planned experiments, the laser will be operated in pulsed mode, with pulse energies of a few millijoules and nanosecond duration. This operating regime has previously been shown to produce successful laser desorption in previous work [128] in a mini-EBIT (see Chapter 4).

6 Calculations of Atomic Structure and Transitions

This chapter presents atomic structure calculations performed using two independent codes: the Flexible Atomic Code (FAC) and AMBiT. These calculations were conducted for highly charged ions of nickel and californium, which are of interest for fundamental atomic physics and high-precision spectroscopy. For each ion, the relevant energy levels and transition wavelengths were calculated using both FAC and AMBiT, while Landé g-factors were obtained exclusively from AMBiT. Comparisons between the two methods are included to evaluate the consistency of the predicted wavelengths and to highlight the strengths of each approach. The calculations were performed using established implementations of FAC and AMBiT [102, 103], with input configurations adapted for the ions investigated in this work.

6.1 Nickel Calculations

Nickel ions with charge states ranging from Ni^{11+} to Ni^{15+} were investigated. Nickel was chosen as a suitable benchmark system because several charge states exhibit strong and well-isolated optical transitions in the visible spectral range, which are readily accessible with the available spectrometer configuration. In particular, Ni^{12+} was selected for detailed study because it exhibits two optical clock transitions, see Section 1.3.2. The 511 nm M1 transition was observed experimentally and is used as a representative example to illustrate the FAC and AMBiT calculations, while the 498 nm E2 clock transition is too weak to be detected under the present experimental conditions.

6.1.1 FAC Calculations for Nickel

For Ni^{12+} ($Z = 28$), after the removal of 12 electrons from neutral nickel, the remaining 16 electrons occupy the lowest energy orbitals according to the Coulomb ordering described in Chapter 2. In this charge state, the 1s, 2s, 2p, and 3s subshells are fully

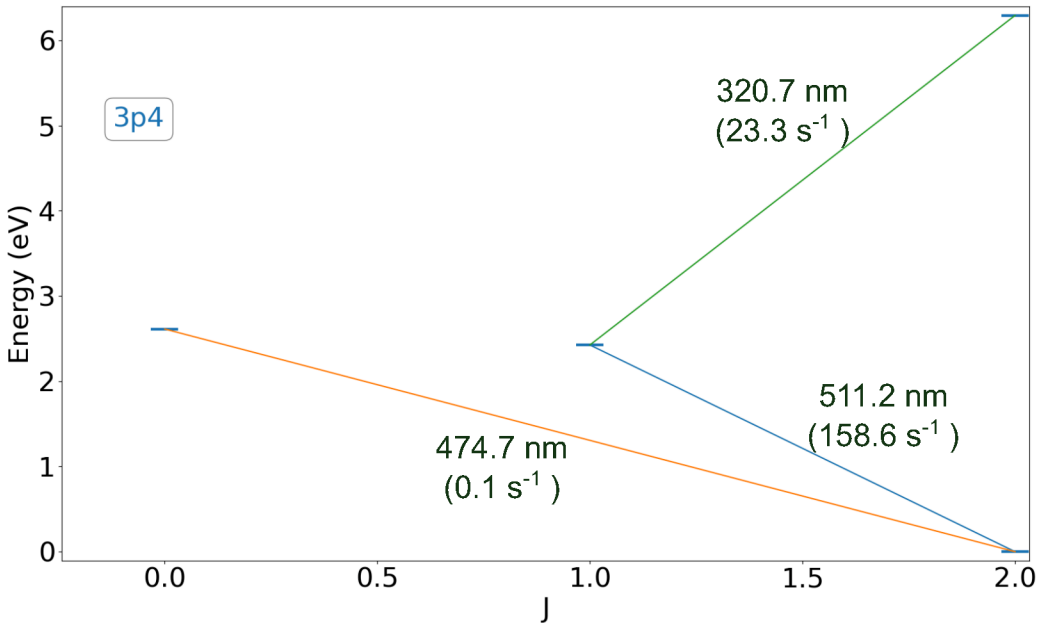

Figure 6.1.1: Grotrian diagram of Ni^{12+} from FAC. In the plot, the X-axis represents the total angular momentum, while the Y-axis indicates the energy in eV. Each horizontal line corresponds to an atomic level, and the lines connecting different levels represent possible radiative decay paths between energy levels. The wavelengths are given in nm and the values next to them in brackets correspond to the transition rates A_{ki}, which have units of s^{-1}. For Ni^{12+}, the most intense spectral line is observed at 511.2 nm.

occupied, forming a closed-shell core with the configuration $1s^2\,2s^2\,2p^6\,3s^2$. As these inner shells are tightly bound and lie significantly lower in energy than the valence electrons, they were treated as 'frozen' core and were not included in the configuration interaction expansion. The outermost electrons reside in the $3p$ subshell, giving the ground-state valence configuration $3p^4$. Only the valence electrons in the $3p$ and higher subshells were allowed to participate in excitations in the present calculation.

To account for possible E1 transitions and electron correlation effects, several excited configurations were included by promoting electrons from the $3p$ orbital into the $3d$ subshell. Specifically, configurations involving one to three electrons in the $3d$ orbital were considered, corresponding to $3p^3 3d^1$, $3p^2 3d^2$, and $3p^1 3d^3$. These configurations were chosen to represent the dominant low-lying excited states accessible through single- and multi-electron excitations. Using this configuration set, FAC was employed to compute energy levels, transition wavelengths, transition probabilities, and emission intensities resulting from collisional excitation. A detailed list of the electronic config-

urations employed for Ni^{11+} through Ni^{15+} is presented in Appendix A.

An example plot for Ni^{12+} is shown in figure 6.1.1. The results reveal that the most intense transition for Ni^{12+} occurs at 511.2 nm, with a transition rate of 158.6 s^{-1}. In addition, weaker transitions are predicted at 474.7 nm and 320.7 nm, with corresponding transition rates of 0.1 s^{-1} and 23.3 s^{-1}, respectively. A detailed comparison between the calculated wavelengths and the experimentally observed lines is presented in Chapter 7.

6.1.2 AMBiT Calculations for Nickel

The electronic structure of Ni^{12+} was also calculated using the AMBiT atomic structure code. A brief explanation of the key parameters for AMBiT and the relevant physical assumptions adopted in the calculation are given here. The input file specifies the atomic number $Z = 28$ and includes 16 electrons, corresponding to the Ni^{12+} ion. The reference configuration used was:

```
1s2 2s2 2p6 3s2:  3p1.33 3p+2.67
```

The colon separates the filled levels of the frozen core from the valence space. The valence electrons are distributed across the relativistic subshells $3p_{1/2}$ and $3p_{3/2}$ with fractional occupations, summing to an average configuration of $3p^4$. Table 6.1.1 summarizes the relativistic subshells of atomic orbitals, characterized by their orbital angular momentum l, total angular momentum j, and the corresponding degeneracy.

In relativistic atomic theory, each orbital (s, p, d, f, g) splits into subshells with different j values due to spin-orbit coupling. The degeneracy of each subshell, defined as the number of distinct quantum states available, is given by $2j+1$. For example, for $j = \frac{3}{2}$, the degeneracy is $2 \times \frac{3}{2} + 1 = 4$.

To compute the fractional occupation of the $3p$ subshell, we note that it consists of $3p_{1/2}$ and $3p_{3/2}$ components with degeneracies 2 and 4, respectively. AMBiT calculates each relativistic subshell separately and applies a weight determined by its occupation. Let x denote the occupation per state within the relativistic subshell, which can be determined from the total number of electrons and the degeneracy of each subshell. For a total of 4 electrons in the $3p$ subshell:

$$\begin{aligned} 2x + 4x &= 4 \\ x &= \frac{2}{3} \end{aligned}$$

shell	$s_{1/2}$	$p_{1/2}$	$p_{3/2}$	$d_{3/2}$	$d_{5/2}$	$f_{5/2}$	$f_{7/2}$	$g_{7/2}$	$g_{9/2}$
l	0	1	1	2	2	3	3	4	4
j	1/2	1/2	3/2	3/2	5/2	5/2	7/2	7/2	9/2
$2j+1$	2	2	4	4	6	6	8	8	10

Table 6.1.1: Relativistic subshells characterized by orbital angular momentum l, total angular momentum j, and degeneracy $2j+1$. This table is adapted from [136].

Multiplying by the degeneracies yields the fractional occupations:

$$3p_{1/2} : 2 \times \frac{2}{3} = 1.33, \quad 3p_{3/2} : 4 \times \frac{2}{3} = 2.67$$

Thus, the relativistic occupation is expressed as $3p_{1/2}^{1.33}\, 3p_{3/2}^{2.67}$, maintaining the total of 4 electrons in the $3p$ shell.

The radial wavefunctions were represented numerically using a B-spline basis, which provided a flexible and accurate description of the electron behavior as a function of distance from the nucleus. Angular momentum states up to $l = 5$ (h orbitals) were included to ensure that higher angular momentum contributions to electron correlation were captured and that the results were numerically converged. The $3s$ orbital was treated as part of the valence space, allowing it to participate in excitations rather than being frozen in the core.

The Breit interaction was included to account for relativistic corrections to the electron-electron interaction. A CI calculation (see Section 2.4) was performed starting from the leading configuration $3p^4$, allowing up to two-electron excitations to account for valence-valence correlation. States of both even and odd parity were included for total angular momentum values $J = 0$ to $J = 6$, and up to eight solutions were computed per symmetry. For the MBPT correction (see Section 2.4), a virtual basis including up to 30 orbitals for each angular momentum symmetry (s to h) was used. This provided a sufficiently large orbital space to ensure convergence of the core-valence correlation contributions. Transition matrix elements (E1, M1, E2, M2) were calculated for all states with total energies less than -0.2 a.u., as specified by the AllBelow option in AMBiT.

Further details regarding the AMBiT input file can be found in [103]. The results from the AMBiT program is shown in figure 6.1.2. The AMBiT input file used for the Ni^{12+} calculation is provided in Appendix A.

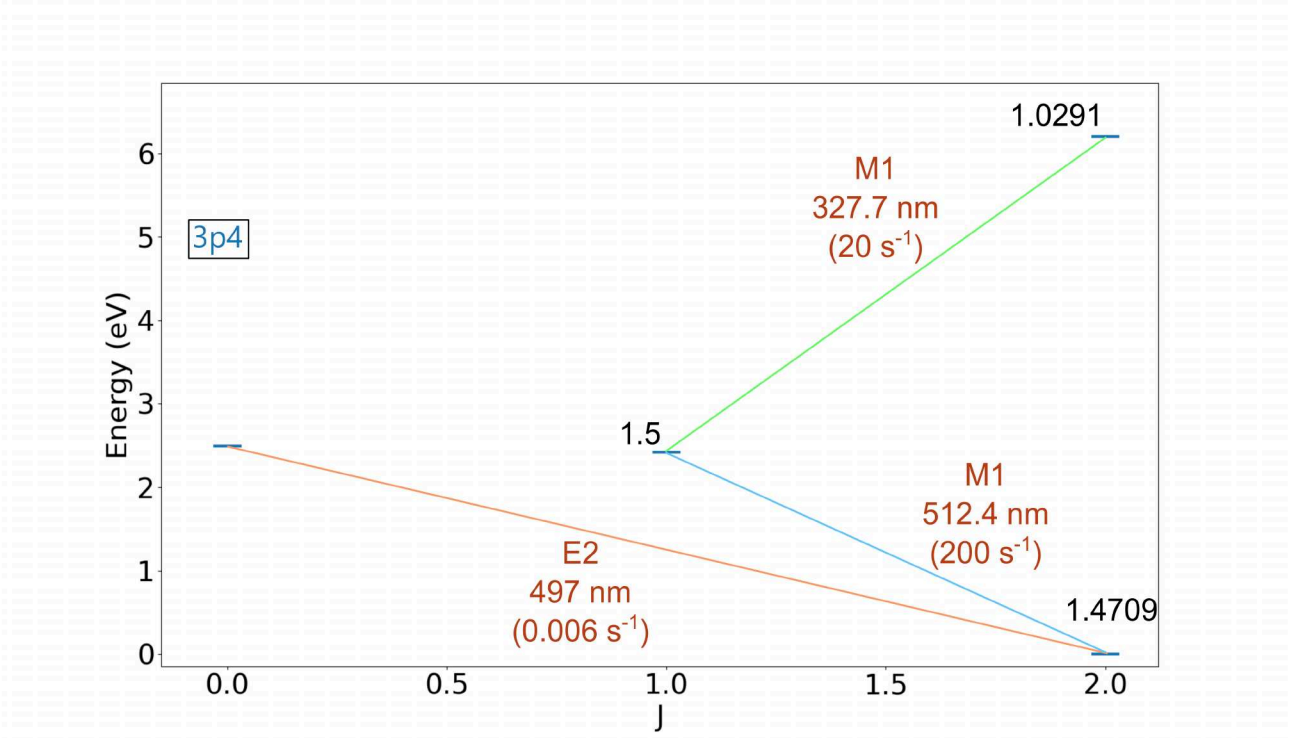

Figure 6.1.2: Grotrian diagram of Ni^{12+} from AMBiT. In the plot, the most intense transition corresponds to the 512.4 nm line, with an Einstein A coefficient (A_{ki}) of 200 s^{-1}. The weakest visible transition is the 327.3 nm line, which exhibits the lowest intensity. The black numerical labels shown at each energy level represent the Landé g-factors as calculated using the AMBiT atomic structure code.

6.1.3 Comparison of FAC and AMBiT Calculations for Ni

A comparison of the wavelengths calculated with FAC and AMBiT (Table 6.1.2) shows that the level of agreement depends strongly on the transition considered. For several transitions with large A_{ki} values, the relative differences are within a few percent. For example, the Ni^{15+} line at 354 nm (FAC) and 353.6 nm (AMBiT) differs by only 0.4 nm ($\approx 0.1\%$), while the prominent Ni^{12+} line at 511.2 nm and 512.4 nm differs by 1.2 nm ($\approx 0.2\%$). Larger differences are observed for certain transitions, especially in higher charge states and for weaker lines. For example, for the strong transition in Ni^{14+} at 258.9 nm (FAC) and 267.2 nm (AMBiT), a deviation of approximately 8 nm ($\approx 3.2\%$) is found. For weaker E2 transitions, wavelength deviations range up to 24% for the Ni^{13+} transition.

A similar pattern is found for the Einstein coefficients A_{ki}. For the strongest transitions, differences are typically on the order of 10-30%. For example, the Ni^{11+} line shows

Ion	J	λ_{FAC}(nm)	λ_{AMBiT} (nm)	g factor	$A_{ki(\mathrm{FAC})}$	$A_{ki(\mathrm{AMBiT})}$
Ni^{11+}	$0.5 \leftrightarrow 1.5$	418.1	419.5	0.67 , 1.33	245.9	200
Ni^{12+}	$1.0 \leftrightarrow 2.0$	511.2	512.4	1.5 , 1.47	158.6	200
	$0 \leftrightarrow 2.0$ (E2)	474.7	497.0	0 , 1.47	0.1	0.006
	$1.0 \leftrightarrow 2.0$	320.7	327.7	1.5 , 1.029	23.3	20
Ni^{13+}	$0.5 \leftrightarrow 2.5$ (E2)	267.7	330.8	0.67 , 1.2	0.9	0.08
Ni^{14+}	$0 \leftrightarrow 1.0$	686.4	658.7	0 , 1.5	53.1	60
	$1.0 \leftrightarrow 2.0$	759.3	771.9	1.5 , 1.432	26.9	30
	$2.0 \leftrightarrow 2.0$	258.9	267.2	1.068 , 1.432	257.6	200
	$0.0 \leftrightarrow 2.0$ (E2)	360.5	355.4	0 , 1.432	0.0	0.03
Ni^{15+}	$0.5 \leftrightarrow 1.5$	354	353.6	0.67 , 1.33	202.5	200

Table 6.1.2: Comparison of calculated wavelengths for selected transitions in highly charged nickel ions using FAC and AMBiT. The table lists the charge state and total angular momentum J for each transition, along with the corresponding wavelengths from both methods. Landé g-factors, calculated using AMBiT, are also included where available; values for the initial and final levels are separated by a comma.

a deviation of about 19%, while the Ni^{15+} transition differs by only about 1%. In contrast, weak and E2 transitions display much larger variations. For instance, the Ni^{13+} E2 transition differs by nearly an order of magnitude in A_{ki}.

Overall, the comparison shows that while noticeable discrepancies remain, particularly for weaker and E2 transitions, the two methods provide comparable predictions for the most prominent lines. For optical transitions, relative uncertainties of about 20% were reported in earlier comparisons of FAC results with experimental measurements, which translate into absolute wavelength deviations of several tens of nanometers and, in dense spectra, up to nearly 100 nm [115]. Although the differences are significant for high-precision spectroscopy, the calculated wavelengths offer valuable guidance for experimental investigations by narrowing the expected spectral region and facilitating line identification. Precise transition energies, however, ultimately require experimental determination.

6.2 Californium Calculation

In contrast to nickel, californium is a very heavy element with a high atomic number ($Z = 98$) and partially filled f-shells for which relativistic effects and electron correlation are expected to play an important role in the electronic structure. Nevertheless, the same computational framework employed for nickel are applied here to

the calculation of highly charged californium ions. In the following subsections, FAC and AMBiT calculations are presented for several californium charge states using input configurations analogous to those used for nickel, allowing a consistent treatment and comparison across the two elements.

6.2.1 FAC Calculations for Californium

Electronic structure calculations were performed for several charge states of californium, ranging from Cf^{12+} to Cf^{19+}, using FAC. This range of charge states covers the ions of interest for the present and planned spectroscopy experiments.

For ions with charge states Cf^{12+} to Cf^{16+}, the ground state was treated as having a closed-shell configuration, including all subshells up to and including the 5d and 6s orbitals. This approach simplifies the system by focusing on excitations from a well-defined core and is suitable for these moderately charged ions where the outer shells are not yet significantly depleted.

From Cf^{17+} onward, the 6s orbital was treated as part of the valence space, allowing excitations from this orbital into higher-lying orbitals. This adjustment accounts for the progressive ionization of the outer electrons and provides a more accurate description of the electronic structure at higher charge states. A summary of the configurations used in the FAC input for each californium charge state is provided in Appendix A.

6.2.2 AMBiT Calculations for Californium

AMBiT calculations employ a complementary approach by utilizing a frozen-core approximation combined with a detailed relativistic treatment of the valence electrons. For charge states Cf^{12+} through Cf^{17+} the closed-shell core was fixed as

$$1s^2\,2s^2\,2p^6\,3s^2\,3p^6\,3d^{10}\,4s^2\,4p^6\,4d^{10}\,4f^{14}\,5s^2\,5p^6\,5d^{10}\,6s^2,$$

with fractional occupation numbers used to represent mixed valence configurations within the CI framework. In the higher charge states Cf^{18+} and Cf^{19+}, the 6s shell was explicitly included in the valence space rather than being treated as part of the frozen core. The full set of valence configurations used in AMBiT is provided in Appendix A.

6.2.3 Comparison of FAC and AMBiT Calculations for Cf

In the case of Cf^{15+}, which has three electrons in the valence shell, the number of possible electronic transitions is very large, so a complete list is impractical. Instead, we highlight transitions with spontaneous emission probabilities (A_{ki} values) of approximately 20 s^{-1} and above, based on FAC calculations. These relatively strong transitions are likely to be observable in future experiments with the HD-EBIT, as demonstrated by successful measurements of HCI transitions with similar strengths using the same facility [115].

The calculated magnetic dipole (M1) cooling transitions for Cf^{17+} and Cf^{15+}, occurring at wavelengths near 468.8 nm and 445.3 nm respectively, correspond to strong radiative transitions that can efficiently remove kinetic energy from the ions through spontaneous emission. These wavelength are consistent with previous theoretical predictions of 479 nm and 442 nm, as reported by [73], with deviations of approximately 10 nm and 3 nm, respectively. Their higher A_{ki} values indicate that these lines are expected to be among the strongest optical transitions for these charge states (See Table 6.2.4 and 6.2.2).

Although experimental measurements to verify these predictions have not yet been performed, a quantitative comparison between FAC and AMBiT provides an estimate of the theoretical uncertainty. For the investigated californium charge states, the predicted wavelengths typically differ by a few nanometers for several prominent transitions, while deviations of up to several tens of nanometers are observed for more complex configurations, as summarized in Tables 6.2.1 - 6.2.7. The agreement between FAC, AMBiT, and the independent calculations of [73] supports the reliability of the predicted transitions and their potential for future experimental observation.

As the number of valence electrons increases, the number of possible electronic transitions, and therefore the number of potential decay channels, increases as well. This general effect leads to denser and more complex spectra and becomes particularly significant for heavy ions such as highly charged californium which possess open f shells with 14 available single-electron states. This gives rise to a large number of possible electron configurations and closely spaced energy levels, in contrast to the much simpler open p shell structure of highly charged nickel ions. For Cf^{16+}, Cf^{15+} Cf^{14+}, Cf^{13+} and Cf^{12+} (see Table 6.2.3 - 6.2.7), only the ground state configuration transitions with spontaneous emission rates (Einstein A coefficients) above 20 s^{-1}, based on calculations from both FAC and AMBiT, are included here.

For Cf^{18+}, the 6s shell is filled with two electrons, forming a closed-shell configuration.

No transitions calculated with FAC could be clearly matched to corresponding transitions from AMBiT within the same energy range and total angular momentum J. Therefore, no direct comparison is presented for this charge state. For Cf^{19+}, there is a single valence electron outside a closed-shell core. According to FAC, the ground state configuration is $6s^1$, whereas AMBiT predicts a $6p^1$ ground state. However, both codes identify an excited state involving a $5f^1$ configuration, and a transition involving this configuration is included in Table 6.2.1.

The deviations observed in Tables 6.2.1 to 6.2.7 between FAC and AMBiT for some of the predicted optical transitions, particularly in Cf^{16+} and Cf^{15+}, are consistent with known limitations of FAC for optical spectroscopy [115]. In the present calculations, the FAC-AMBiT differences range from below 1 nm for several transitions in Cf^{12+} and Cf^{13+}, to a few tens of nanometers for transitions in Cf^{14+}, Cf^{15+} and Cf^{17+} and reach up to approximately 180 nm for some transitions in Cf^{16+} illustrating both the strengths and the limitations of FAC and AMBiT for high-Z open-shell ions.

Level	J	λ_{FAC}(nm)	λ_{AMBiT} (nm)	g factor	$A_{ki(\mathrm{FAC})}$	$A_{ki(\mathrm{AMBiT})}$
$5f^1$	2.5 ↔ 3.5	463	503.5	0.857 , 1.143	116	90

Table 6.2.1: Transition in $5f^1$ for Cf^{19+} from FAC and AMBiT calculations.

Level	J	λ_{FAC}(nm)	λ_{AMBiT} (nm)	g factor	$A_{ki(\mathrm{FAC})}$	$A_{ki(\mathrm{AMBiT})}$
$5f^1$	2.5 ↔ 3.5	488.7	468.8	0.857 , 1.43	98.9	100

Table 6.2.2: Transition in $5f^1$ for Cf^{17+} from FAC and AMBiT calculations.

Level	J	λ_{FAC}(nm)	λ_{AMBiT} (nm)	g factor	$A_{ki(\mathrm{FAC})}$	$A_{ki(\mathrm{AMBiT})}$
$5f^1\ 6p^1$	3.0 ↔ 4.0	346.3	437.1	0.830 , 1.05	288.7	80
$5f^1\ 6p^1$	2.0 ↔ 3.0	714.7	532.6	0.845 , 1.174	32.1	80
$5f^2$	2.0 ↔ 2.0	321.1	377.6	1.168 , 0.756	100.8	40
$5f^2$	2.0 ↔ 3.0	714.5	796.1	0.756 , 1.099	58.8	40
$5f^2$	3.0 ↔ 4.0	503.8	504.5	1.099 , 1.118	90.3	60
$5f^2$	4.0 ↔ 4.0	498.2	684.3	1.118 , 1.123	76.9	20
$5f^2$	4.0 ↔ 4.0	414.9	303.2	1.123 , 0.850	49	100
$5f^2$	4.0 ↔ 5.0	565.0	515.3	0.850 , 1.033	125.8	200
$5f^2$	5.0 ↔ 6.0	282.3	297.5	1.033 , 1.028	113	100
$5f^2$	5.0 ↔ 6.0	707.8	697.3	1.033 , 1.139	56.1	60
$5f^2$	6.0 ↔ 6.0	469.5	518.8	1.028 , 1.139	30.6	30

Table 6.2.3: The wavelengths in nm for the ground and first excited state configuration for Cf^{16+} are given. Only the transitions with $A_{ki} > 20\ s^{-1}$ are included here.

Level	J	λ_{FAC}(nm)	λ_{AMBiT} (nm)	g factor	$A_{ki(\mathrm{FAC})}$	$A_{ki(\mathrm{AMBiT})}$
$5f^1\ 6p^2$	$2.5 \leftrightarrow 3.5$	405	445.3	0.848 , 1.085	193.2	90
$5f^2\ 6p^1$	$2.5 \leftrightarrow 2.5$	256.4	293.9	1.107 , 0.717	188.9	100
$5f^2\ 6p^1$	$2.5 \leftrightarrow 3.5$	372.3	374.2	0.717 , 1.445	164.5	100
$5f^2\ 6p^1$	$2.5 \leftrightarrow 3.5$	722.2	758.1	0.717 , 1.039	38.1	30
$5f^2\ 6p^1$	$3.5 \leftrightarrow 4.5$	492.9	426.1	1.085 , 1.007	78.7	23
$5f^2\ 6p^1$	$4.5 \leftrightarrow 4.5$	273.3	238.4	1.007 , 0.817	81.6	30
$5f^2\ 6p^1$	$4.5 \leftrightarrow 4.5$	396.1	389.3	1.037 , 0.817	46.2	50
$5f^2\ 6p^1$	$4.5 \leftrightarrow 5.5$	412.6	405.5	0.817 , 1.002	323.6	300
$5f^2\ 6p^1$	$4.5 \leftrightarrow 5.5$	577.4	643.8	1.037 , 1.173	54.5	30
$5f^2\ 6p^1$	$4.5 \leftrightarrow 5.5$	261.3	344.6	1.037 , 0.973	73.2	10
$5f^2\ 6p^1$	$5.5 \leftrightarrow 6.5$	578.4	589.9	1.002 , 1.08	99.3	80
$5f^2\ 6p^1$	$5.5 \leftrightarrow 6.5$	254.0	300.2	1.002 , 1.033	363.4	200

Table 6.2.4: The wavelengths in nm for the ground and first excited state configuration for Cf^{15+} are given. Only the transitions with $A_{ki} > 20\ s^{-1}$ are included here.

Level	J	λ_{FAC}(nm)	λ_{AMBiT} (nm)	g factor	$A_{ki(\mathrm{FAC})}$	$A_{ki(\mathrm{AMBiT})}$
$5f^2\ 6p^2$	$0.0 \leftrightarrow 1.0$	786.7	743.5	0 , 1.519	35.1	40
$5f^2\ 6p^2$	$1.0 \leftrightarrow 2.0$	241.5	247.9	1.519 , 0.736	30	30
$5f^2\ 6p^2$	$2.0 \leftrightarrow 2.0$	382.9	374.4	1.255 , 1.777	236.2	300
$5f^2\ 6p^2$	$2.0 \leftrightarrow 2.0$	290.2	295.3	1.177 , 0.736	193.8	200
$5f^2\ 6p^2$	$2.0 \leftrightarrow 3.0$	615.5	678.6	1.177 , 1.086	26	20
$5f^2\ 6p^2$	$2.0 \leftrightarrow 3.0$	549.2	522.8	0.736 , 1.086	138.1	200
$5f^2\ 6p^2$	$3.0 \leftrightarrow 4.0$	404.2	388.0	1.086 , 1.136	195.5	200
$5f^2\ 6p^2$	$4.0 \leftrightarrow 4.0$	347.5	339.2	1.086 , 0.827	103.8	100
$5f^2\ 6p^2$	$4.0 \leftrightarrow 5.0$	406.2	398.0	1.136 , 1.086	161	200
$5f^2\ 6p^2$	$4.0 \leftrightarrow 5.0$	452.9	439.9	0.827 , 1.033	268.9	300
$5f^2\ 6p^2$	$5.0 \leftrightarrow 6.0$	272.9	282.3	1.033 , 1.045	273.9	300
$5f^2\ 6p^2$	$5.0 \leftrightarrow 6.0$	613.9	624.0	1.033 , 1.127	84.1	70

Table 6.2.5: The wavelengths in nm for the ground state configuration for Cf^{14+} are given. Only the transitions with $A_{ki} > 20\ s^{-1}$ are included here.

Level	J	λ_{FAC}(nm)	λ_{AMBiT} (nm)	g factor	$A_{ki(\mathrm{FAC})}$	$A_{ki(\mathrm{AMBiT})}$
$5f^2\ 6p^3$	$0.5 \leftrightarrow 1.5$	539.6	527.1	0.098 , 1.008	121.6	100
$5f^2\ 6p^3$	$1.5 \leftrightarrow 1.5$	329.0	341.4	1.697 , 0.849	100.5	100
$5f^2\ 6p^3$	$1.5 \leftrightarrow 2.5$	347.6	339.6	0.849 , 0.984	112.4	100
$5f^2\ 6p^3$	$2.5 \leftrightarrow 2.5$	460.0	442.0	0.984 , 1.034	46.8	50
$5f^2\ 6p^3$	$2.5 \leftrightarrow 2.5$	402.4	389.3	1.063 , 0.625	67.6	80
$5f^2\ 6p^3$	$2.5 \leftrightarrow 3.5$	408.9	408.7	1.034 , 1.069	175.7	200
$5f^2\ 6p^3$	$2.5 \leftrightarrow 3.5$	296.8	298.0	0.625 , 1.069	138.8	100
$5f^2\ 6p^3$	$2.5 \leftrightarrow 3.5$	497.6	475.1	0.625 , 1.064	146.7	200
$5f^2\ 6p^3$	$3.5 \leftrightarrow 3.5$	326.5	328.3	1.189 , 1.052	177.8	200
$5f^2\ 6p^3$	$3.5 \leftrightarrow 3.5$	507.9	540.5	1.052 , 0.862	28.5	20
$5f^2\ 6p^3$	$3.5 \leftrightarrow 3.5$	288.1	283.1	1.076 , 0.862	138.1	200
$5f^2\ 6p^3$	$3.5 \leftrightarrow 4.5$	758.0	716.6	1.052 , 1.166	50.6	60
$5f^2\ 6p^3$	$3.5 \leftrightarrow 4.5$	304.1	308.1	0.862 , 1.166	60.6	60
$5f^2\ 6p^3$	$3.5 \leftrightarrow 4.5$	441.2	428.1	0.862 , 1.053	170.8	200
$5f^2\ 6p^3$	$4.5 \leftrightarrow 4.5$	272.8	270.7	1.111 , 0.924	33	30
$5f^2\ 6p^3$	$4.5 \leftrightarrow 4.5$	470.7	458.8	1.053 , 0.924	47.4	50
$5f^2\ 6p^3$	$4.5 \leftrightarrow 5.5$	323.7	318.6	0.924 , 1.104	87.9	100
$5f^2\ 6p^3$	$4.5 \leftrightarrow 5.5$	451.6	443.4	0.924 , 1.108	98.7	100
$5f^2\ 6p^3$	$5.5 \leftrightarrow 5.5$	435.7	422.9	1.104 , 1.041	110.2	100
$5f^2\ 6p^3$	$5.5 \leftrightarrow 6.5$	631.7	622.3	1.041 , 1.143	116.4	100

Table 6.2.6: The wavelengths in nm for the ground state configuration for Cf^{13+} are given. Only the transitions with $A_{ki} > 20\ s^{-1}$ are included here.

Level	J	λ_{FAC}(nm)	λ_{AMBiT} (nm)	g factor	$A_{ki(\mathrm{FAC})}$	$A_{ki(\mathrm{AMBiT})}$
$5f^2\ 6p^4$	$1.0 \leftrightarrow 2.0$	340.5	341.4	1.260 , 1.367	78.7	60
$5f^2\ 6p^4$	$1.0 \leftrightarrow 2.0$	451.0	438.0	1.260 , 0.917	61.4	70
$5f^2\ 6p^4$	$2.0 \leftrightarrow 2.0$	353.1	353.5	1.005 , 1.160	78.1	80
$5f^2\ 6p^4$	$2.0 \leftrightarrow 2.0$	542.0	521.9	0.917 , 1.160	54	40
$5f^2\ 6p^4$	$2.0 \leftrightarrow 2.0$	321.3	321.7	1.105 , 0.557	103.6	60
$5f^2\ 6p^4$	$2.0 \leftrightarrow 3.0$	369.6	367.5	0.557 , 0.895	234.2	200
$5f^2\ 6p^4$	$2.0 \leftrightarrow 3.0$	356.4	355.0	1.105 , 0.795	60.3	20
$5f^2\ 6p^4$	$2.0 \leftrightarrow 3.0$	253.6	253.5	0.557 , 1.025	86.2	100
$5f^2\ 6p^4$	$2.0 \leftrightarrow 3.0$	620.2	606.1	1.160 , 1.206	57.5	60
$5f^2\ 6p^4$	$3.0 \leftrightarrow 4.0$	436.4	430.1	0.795 , 1.151	57.1	60
$5f^2\ 6p^4$	$3.0 \leftrightarrow 4.0$	361.1	352.4	0.795 , 1.009	88.3	80
$5f^2\ 6p^4$	$3.0 \leftrightarrow 4.0$	329.1	326.2	0.795 , 1.090	87.5	100
$5f^2\ 6p^4$	$3.0 \leftrightarrow 4.0$	267.1	268.6	0.795 , 1.114	50.6	50
$5f^2\ 6p^4$	$4.0 \leftrightarrow 4.0$	370.3	375.7	1.114 , 1.072	101.9	90
$5f^2\ 6p^4$	$4.0 \leftrightarrow 4.0$	307.1	310.4	1.090 , 0.902	27.7	30
$5f^2\ 6p^4$	$4.0 \leftrightarrow 4.0$	334.6	334.0	1.009 , 0.902	101.1	100
$5f^2\ 6p^4$	$4.0 \leftrightarrow 5.0$	449.4	444.9	0.902 , 1.110	102.3	100
$5f^2\ 6p^4$	$5.0 \leftrightarrow 6.0$	646.8	632.5	1.021 , 1.127	81.8	90

Table 6.2.7: The wavelengths in nm for the ground state configuration for Cf^{12+} are given. Only the transitions with $A_{ki} > 20\ s^{-1}$ are included here.

6.2.4 Indirect Determination of Clock Transitions

Since the clock transition in highly charged ions is typically weak and challenging to observe directly, an effective approach to identify it involves finding a closed excitation cycle among relevant energy levels. Once such a closed cycle is established, the so-called Rydberg-Ritz combination principle can be applied to accurately determine the clock transition frequency from measured transition wavelengths within the cycle. This principle states that if the energies of three levels are connected by two known transitions, the third transition energy (or frequency) can be deduced by simple addition or subtraction of the known energy differences. In the context of spectroscopy, this allows the indirect determination of a transition that is too weak to observe directly, by combining measurements of stronger, more accessible transitions that form a closed loop.

Figures 6.2.1 and 6.2.2 illustrate two closed cycles calculated for Cf^{17+}, which enable precise evaluation of its clock transition using this method. The identified cycles exhibit transitions in the extreme ultraviolet (EUV) and vacuum ultraviolet (VUV) spectral regions as well, with wavelengths ranging approximately from 15 nm to 45 nm. Cycle 1 includes two EUV transitions at 24.1 nm and 15.7 nm, one VUV transition at 44.8 nm and one optical transition at 468.8 nm. The clock transition denoted as T3 can be indirectly calculated by the Rydberg Ritz principle as shown below:

$$\mathrm{T3} = (\mathrm{T1} + \mathrm{T2}) - (\mathrm{T5} + \mathrm{T4}) \tag{6.1}$$

Cycle 2 contains two EUV transitions at 17 nm and 16.4 nm and the clock transition denoted as T3 can be obtained by:

$$\mathrm{T3} = \mathrm{T1} - \mathrm{T2} \tag{6.2}$$

These short-wavelength transitions require spectrometers equipped with specialized optics and detectors capable of operating in the EUV and VUV ranges. However, the HD-EBIT facility currently lacks such instrumentation, which prevents direct observation of these lines and highlights the need for expanded spectral coverage in future experiments.

The figures 6.2.1 and 6.2.2 also list the transition types (electric dipole, E1, and magnetic dipole, M1) together with the corresponding Einstein coefficients. For the transitions forming the closed cycles, these coefficients span a wide range from approximately 10^2 s^{-1} for weak optical M1 transitions up to about 2×10^{11} s^{-1} for strong E1 transitions in the EUV and VUV regions. The cycles shown here were selected based

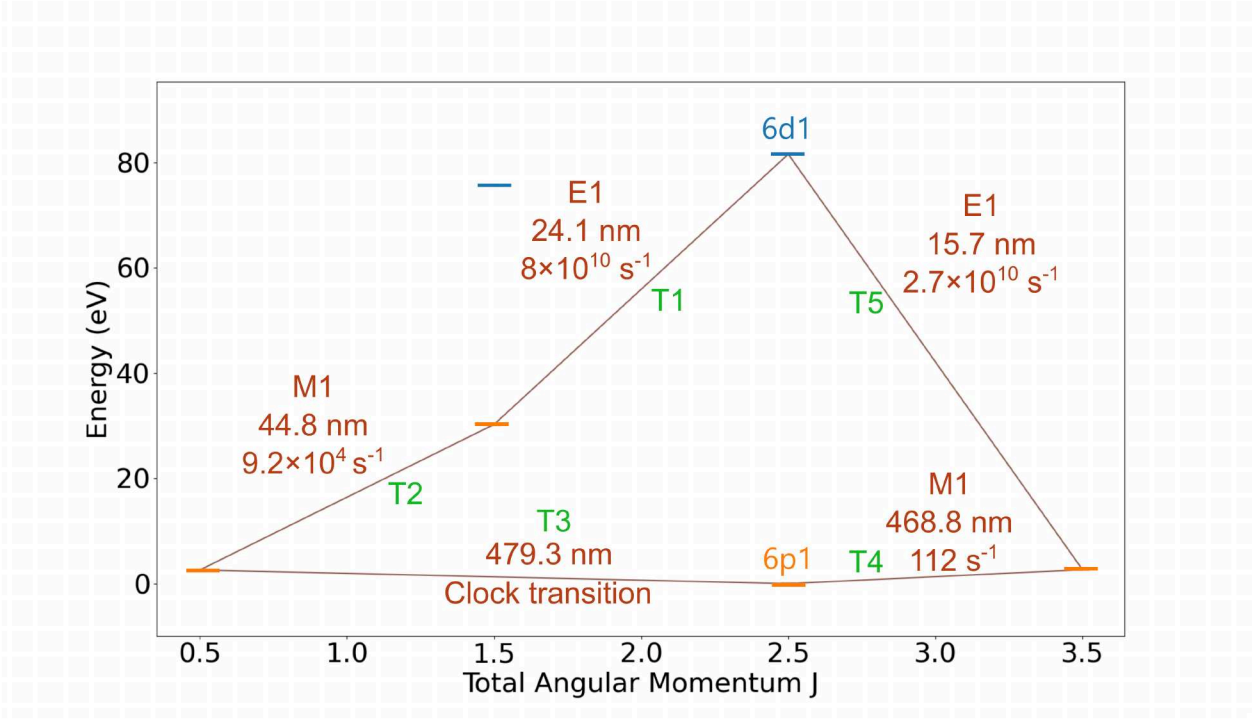

Figure 6.2.1: Closed excitation cycle (Cycle 1) for Cf^{17+} involving EUV, VUV and optical transitions. The clock transition is marked as T3.

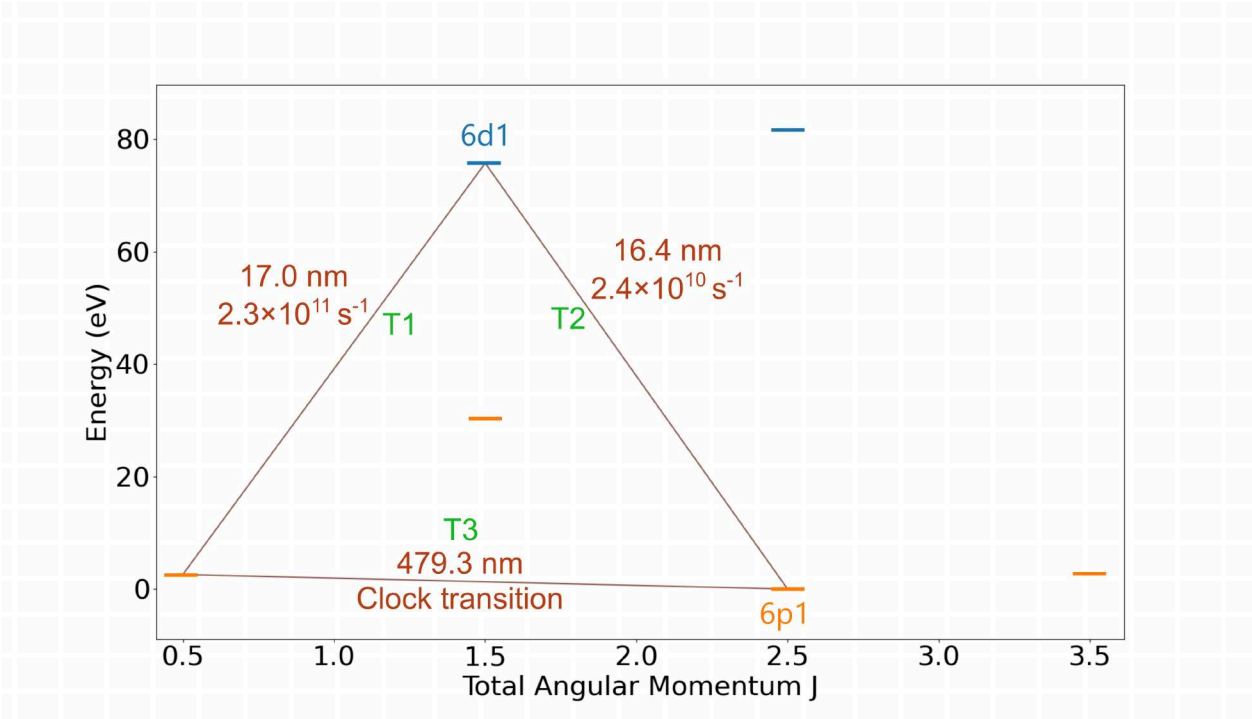

Figure 6.2.2: Closed excitation cycle (Cycle 2) for Cf^{17+} involving two EUV transitions. The clock transition is marked as T3.

on calculations because they involve comparatively strong transitions and therefore represent experimentally accessible candidates for experimental implementation of the Rydberg-Ritz scheme once suitable EUV and VUV spectrometers become available.

7 Optical Spectroscopy of Highly Charged Nickel Ions

This chapter presents the experimental procedures and results of optical spectroscopy performed on highly charged nickel ions in charge states Ni^{11+}, Ni^{12+}, Ni^{14+}, and Ni^{15+} in the HD-EBIT. These measurements serve as a proof-of-principle study in preparation for future spectroscopy of heavy highly charged ions such as californium, which are of particular interest for their potential use in fundamental physics tests and next-generation atomic clocks.

The goal of this work was to establish the experimental protocols for ion production, trapping, calibration, and spectroscopic detection within an EBIT environment. The methodology used to perform wavelength calibration and to identify spectral lines is described in detail, followed by the presentation of the measured spectra and line assignments. Where available, the measurements are compared with previously reported experimental results to assess consistency and accuracy. Finally, experimental limitations along with potential avenues for improving current and future measurements are discussed.

7.1 Analysis Procedure

The raw data acquired from the CCD camera are stored as a two-dimensional array of pixel intensities (refer Section 3.3). One axis of the CCD image corresponds to the wavelength-dispersed direction and is therefore related to wavelength, however, the pixel positions along this axis are not inherently calibrated in wavelength. Therefore, wavelength calibration is required to convert pixel positions into physical wavelength values.

In this experiment, hollow cathode lamps were used as calibration source. Known spectral lines from the corresponding lamp were identified in the CCD data, and their

corresponding pixel positions were used to perform a polynomial fit, typically quadratic or cubic. The resulting polynomial serves as the wavelength calibration, providing the relationship between pixel position and wavelength across the detector.

Additional corrections are applied to account for instrumental and environmental effects that can influence the recorded spectrum. These include removal of cosmic rays from the CCD images and correction of curvature and temperature-dependent shifts introduced by optical components. Once the calibrated and corrected spectra were obtained, Zeeman fitting models can be applied to extract parameters including the transition wavelengths and Landé g factors. The individual steps of the calibration, correction procedures, and analysis methods are described in the following sections.

7.1.1 Cosmic Removal

Cosmic rays are highly energetic particles originating from space. When they interact with the Earth's atmosphere, they produce secondary particles that can strike the detector and result in unwanted bright spots in the camera images. Since the typical exposure times of CCD images range from 20 minutes to 1 hour, these high-energy particles can cause isolated pixels with significantly higher intensities than the surrounding background or signal. These cosmic ray hits are spatially localized and typically affect only one or a few pixels, making them distinguishable from the broader spatial structure of the ion signal. To ensure accurate data analysis, such artifacts were removed using histogram outlier detection, as described in previous works [115, 134].

The method works by dividing the CCD image into small sections (typically 32×8 pixels) and analyzing each section individually. For each section, a histogram of pixel intensities is generated. The assumption is that real signal and background pixels will form a continuous distribution in the lower intensity range, while cosmic ray hits appear as outliers at much higher intensities. The algorithm searches the histogram for a gap, i.e., a set of consecutive empty bins (intensity intervals where no pixels fall). If such a gap exists and is statistically significant (e.g., longer than a certain multiple of the histogram's standard deviation), it is taken as a separation between normal signal and cosmic outliers. All pixels with intensities above this threshold are flagged as cosmic rays and replaced with NaN (not a number) values, ensuring they are ignored in subsequent data analysis steps. This process is repeated across the entire image.

7.1.2 Curvature and Temperature Corrections

The recorded spectral lines correspond to the image of the entrance slit formed on the CCD camera. These lines exhibit a slight curvature caused by optical distortions or geometric misalignments within the spectrometer. To correct for this curvature, a two-dimensional Gaussian function was fitted to the brightest calibration lines. The details of this procedure are described in previous work [115]; a brief explanation is provided here.

The 2D Gaussian used for the fitting is given by:

$$I(x,y) = A\exp\left(-\left(\frac{x-(m(y-y_0)^2+b(y-y_0)+c)}{\sigma_x}\right)-\left(\frac{y-y_0}{\sigma_x}\right)^2\right)+d$$

where A is the amplitude representing the intensity of the spectral line, y_0 is the vertical center position of the Gaussian on the detector, σ_x and σ_y are the standard deviations characterizing the line widths of the Gaussian profile along the horizontal and vertical directions and d is the constant offset accounting for noise.

The curvature of the spectral line is described by the quadratic polynomial for the center position in the x-direction as a function of y:

$$x_{\text{center}}(y) = m(y-y_0)^2 + b(y-y_0) + c$$

where m, b, and c represents the curvature, tilt, and baseline position of the spectral line, respectively.

Due to the extended acquisition times, thermal drift of the spectrometer optics causes a gradual drift of the image position on the CCD over the course of a measurement set. This drift was corrected following the procedure described in Ref. [115, 134]. Calibration images acquired throughout each set were used to track the positions of prominent reference lines, which were extracted using Gaussian fits. The temporal evolution of the line positions was fitted with a model selected according to the observed drift behavior, and the resulting interpolated shift was applied to all images to compensate for thermal drift.

7.1.3 Measurement Scheme

Spectroscopy measurements were carried out using the procedure followed by [115]. After introducing nickel atoms into the drift tube through the gas-injection setup described earlier in Section 3.2, the electron beam was operated at a current of approximately 20 mA. This yields low ion temperatures and thus reduced Doppler broadening, resulting in narrow Zeeman components in the recorded spectra.

Rather than beginning with a wide spectral survey, the experiment first aimed to confirm the production of highly charged Ni ions. This was achieved by setting the cathode voltage near 400 V, corresponding to an electron-beam energy slightly above the ionization potential of Ni^{12+} (384 eV [137]) and monitoring for characteristic emissions. The detection of the line at 511 nm provided evidence that ionization to the relevant charge states had been achieved.

After confirming the production of highly charged nickel ions, a wide energy scan was conducted varying the cathode voltage from 200 V to 600 V to explore the broader spectral region. For this, the spectrometer was configured to scan wavelengths from 260 nm to 660 nm. A 150 gr/mm grating was used due to its broad bandwidth of approximately 90 nm per CCD exposure. The full wavelength range was therefore recorded in multiple measurements by rotating the grating to successive central wavelengths, such that adjacent spectra overlapped.

7.2 Results

Raw CCD frames recorded during the scans contain only pixel information. These pixel coordinates were translated into wavelengths using the grating equation for the 150 gr/mm grating together with the spectrometer geometry. In addition, calibration lamp spectra recorded with the 150 gr/mm grating were used only as a rough consistency check of the wavelength scale, without performing a detailed pixel-to-wavelength calibration at this stage. This yields an uncalibrated wavelength scale that is sufficient to track the appearance and evolution of spectral lines as a function of electron beam energy.

The converted data for central wavelengths of 396 nm, 472 nm, and 548 nm are shown together in the stacked spectra presented in figure 7.2.1. In this figure, one can observe lines appearing at different values of the rough electron beam energy, as set by

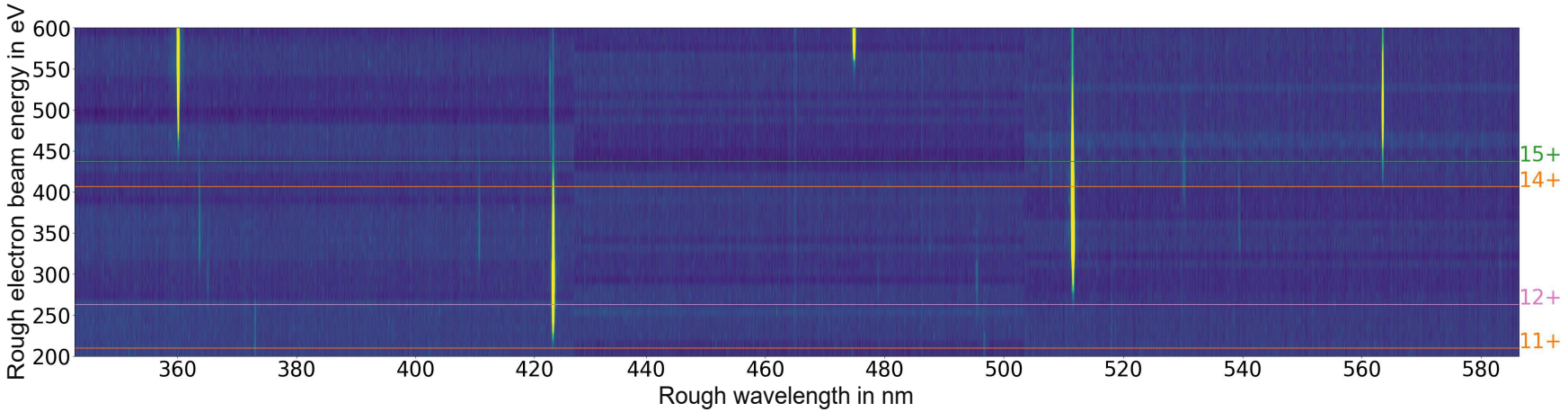

Figure 7.2.1: CCD image of highly charged nickel emission spectra for central wavelengths of 396 nm, 472 nm, and 548 nm using a rough wavelength scale, shown as a function of rough electron beam energy. Horizontal guide lines separate the regions corresponding to the dominant charge states (Ni^{11+}, Ni^{12+}, Ni^{14+}, and Ni^{15+}). Prominent lines are observed at 360.1 nm (Ni^{15+}), 423.1 nm (Ni^{11+}), 511 nm (Ni^{12+}) and 563 nm (second-order diffraction of the 281 nm transition in Ni^{14+}). An intense line near 474 nm could not be identified from the available calculations and may originate from a higher nickel charge state for which no transitions were calculated.

the applied cathode voltage. This is because when the beam energy is raised, sequential population of different ionic charge states occurs in the trap. The points at which each line emerges, reaches its strongest intensity, and eventually disappears are indicated by horizontal guide lines marking the dominant charge states (Ni^{11+}, Ni^{12+}, Ni^{14+}, and Ni^{15+}) (see figure 7.2.1).

Using these features, along with the known ionization energies and FAC calculations, the charge states can be identified and the observed spectral lines assigned accordingly. No emission line from Ni^{13+} is observed in the spectra, which is consistent with the fact that its ground state transition is an E2 transition with a very low transition rate (see Table 6.1.2), making it too weak to be detected under the present experimental conditions. In addition, the corresponding transition wavelength is about 264.7 nm, which lies in the ultraviolet range and outside the spectral range accessible with the grating and optical setup used here.

Once the relevant transitions were identified, high-resolution spectroscopy was performed on each line using either the 1800 gr/mm or 3600 gr/mm grating, depending on the wavelength region, over extended periods to resolve the Zeeman structure induced by the 8 T magnetic field of the Heidelberg EBIT. This allowed for more precise determination of both the transition wavelengths and the associated Landé g-factors. The full measurement sequence included ion spectra (i), calibration spectra (c), and dark images (d), recorded sequentially. The dark images serve as background frames for subtraction during data processing. The acquisition pattern varied but generally alternated among these types (e.g., cidcid, cicicid) to ensure accurate wavelength calibration and background correction. Each ion and dark spectrum was acquired over approximately one hour, while calibration exposures required 10 to 15 minutes. In total, an average of 15 hours of ion spectroscopy data was accumulated for each spectral line identified in the wavelength scans (see figure 7.2.1). As an example, the measurement procedure for Ni^{12+} at wavelength 511 nm is described here in detail.

7.2.1 Calibration

A hollow cathode lamp containing Fe and Ar was used as the calibration source. Figure 7.2.2 shows a typical raw calibration spectrum plotted as pixel number versus intensity where the characteristic emission lines are clearly visible. These lines are essential for establishing the pixel-wavelength mapping. Similarly, figure 7.2.3 presents the corresponding raw ion spectrum obtained under identical detector settings.

To identify the calibration peaks, the measured line positions were compared with

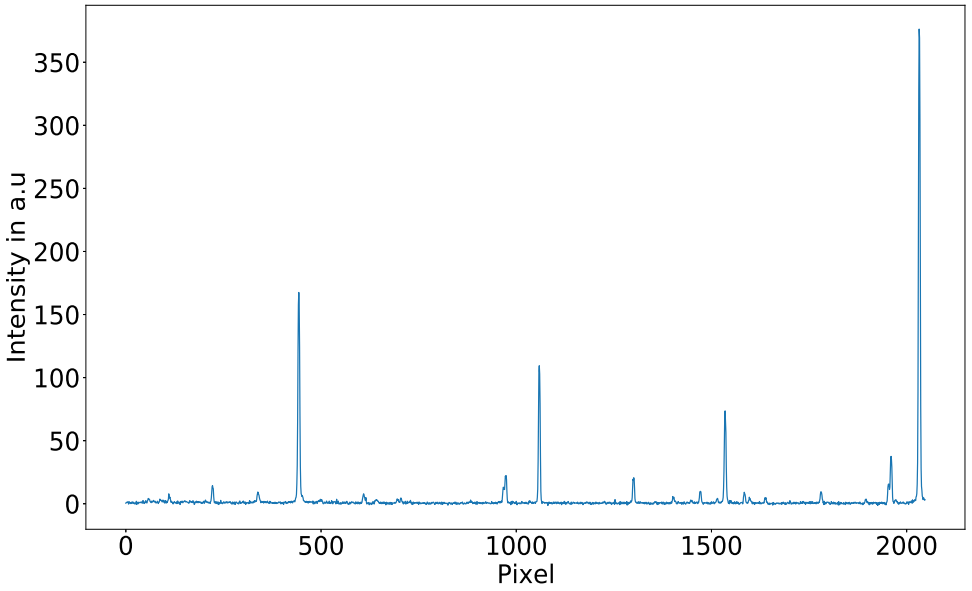

Figure 7.2.2: Example raw calibration spectrum from Fe-Ar lamp.

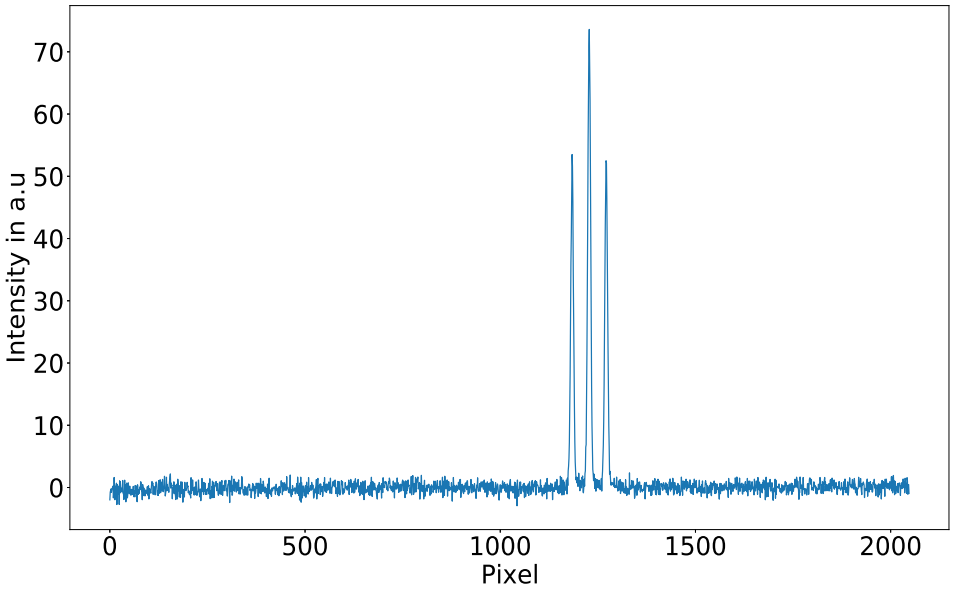

Figure 7.2.3: Example raw ion spectrum. The wavelength axis (Pixel) matches that of figure 7.2.2. The visible splitting of the spectral line arises from the Zeeman effect in the 8 T magnetic field.

Element	Wavelength (nm) in vacuum	Wavelength (nm) in air
Fe I	508.47551(8)	508.33382(8)
Ar II	509.19136(3)	509.04948(3)
Fe I	510.88705(8)	510.74471(8)
Fe I	510.90641(8)	510.76407(8)
Fe I	511.18369(8)	511.04128(8)
Fe I	512.51473(8)	512.37196(8)
Ar II	512.71945(7)	512.57663(7)
Fe I	513.51185(8)	513.36882(8)
Fe I	514.08944(8)	513.94625(8)
Ar II	514.32151(1)	514.17826(1)

Table 7.2.1: Table of Fe I and Ar II spectral lines from the NIST database [137]. Roman numerals indicate the ionization state. The number in parentheses after each wavelength represents the uncertainty in the last digits of the reported value in nanometers.

reference data from the National Institute of Standards and Technology (NIST) Atomic Spectra Database [137]. NIST provides wavelengths and transition data with high accuracy, making it a standard reference for spectroscopic calibration. By matching the observed peaks with the NIST wavelengths for Fe and Ar, each calibration line can be clearly assigned to the correct atomic transition. Table 7.2.1 lists all the calibration lines used, with a central wavelength of 511 nm. Figure 7.2.4 (top) shows the observed calibration spectrum, now with each emission line identified by matching it to the corresponding element in the NIST database.

7.2.2 Dispersion Function

The wavelengths obtained from the NIST database were then plotted against the corresponding pixel positions as shown in the middle panel of figure 7.2.4. The resulting residuals are presented in the bottom panel. To improve the signal-to-noise ratio and obtain a stable dispersion relation, all calibration lamp spectra recorded during a given measurement run were first summed, and a single wavelength calibration was then performed using this combined calibration spectrum. To convert pixel numbers into physical wavelengths, a quadratic polynomial was fitted to this calibration data. A quadratic fit is appropriate because the dispersion of the spectrometer is approximately linear over small regions but exhibits slight curvature across the detector due to optical aberrations and the grating geometry. The fitted polynomial function is given below:

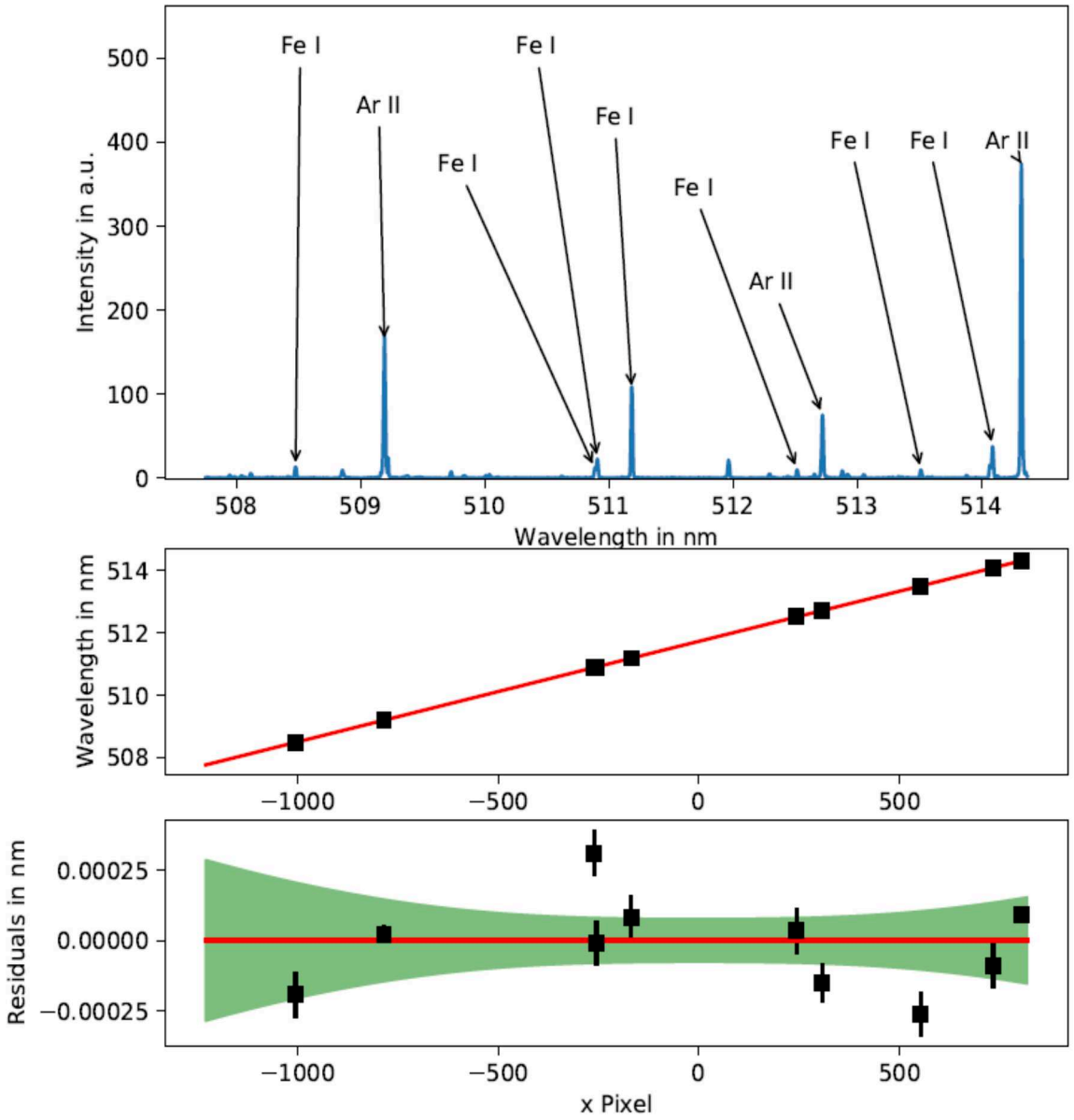

Figure 7.2.4: Wavelength calibration using NIST reference lines. Top: Recorded spectrum with spectral lines assigned to elements using reference wavelengths for Fe I and Ar II from the NIST database. Middle: Dispersion plot showing reference wavelengths as a function of measured pixel position. Bottom: Residuals illustrating the quality of the dispersion fit.

$$\begin{aligned}\lambda(x) = &-6.50(17) \times 10^{-9} \frac{\text{nm}}{\text{px}^2}(x - 819\ \text{px})^2 \\ &+ 3.22710(9) \times 10^{-3} \frac{\text{nm}}{\text{px}}(x - 819\ \text{px}) + 511.58649(8)\ \text{nm}\end{aligned} \tag{7.1}$$

The dispersion function was determined using an orthogonal distance regression (ODR) algorithm to account for uncertainties in both the wavelength and pixel position. In this calibration, each coefficient of the polynomial corresponds to a specific physical effect, and their magnitudes reveal the main contributors to the wavelength determination. The constant term is the wavelength evaluated directly at the line position ($x = 819$ px) and carries the smallest relative uncertainty because the polynomial is centered at this pixel. The dominant term is the linear coefficient which represents the primary dispersion of the grating and therefore contributes most strongly to changes in wavelength with pixel position. The quadratic coefficient accounts for the weak residual curvature of the dispersion relation across the detector.

7.2.3 Zeeman Fitting

The 8 T magnetic field of the HD-EBIT causes splitting of the spectral lines according to the Landé g-factor of the transition. To improve the signal-to-noise ratio, all dark-subtracted ion spectra recorded during a given measurement run were summed for each transition prior to further analysis. After calibrating the spectrometer and converting the pixel positions into physical wavelengths, the high-resolution ion spectra were analyzed to extract the Zeeman structure. The analysis of the Zeeman structure required expressing the spectral data in energy rather than wavelength, because Zeeman splittings are linear and symmetric in energy, so the nm values were converted to eV using the following equation:

$$E(\text{eV}) = \frac{hc}{\lambda_{\text{vacuum}}(\text{nm})} \tag{7.2}$$

As the spectrometer was not under vacuum, the measured wavelengths were in air, which were then converted to vacuum wavelengths with the equation [138]:

$$\lambda_{\text{air}} = \frac{\lambda_{\text{vacuum}}}{n_{\text{air}}} \tag{7.3}$$

$$n_{\text{air}} = 1 + \left(8060.51 + \frac{2480990}{132.274 - S^2} + \frac{17455.7}{39.32957 - S^2}\right) \times 10^{-8} \tag{7.4}$$

where

$$S = \frac{1000}{\lambda_{\text{air}}(\text{nm})} \tag{7.5}$$

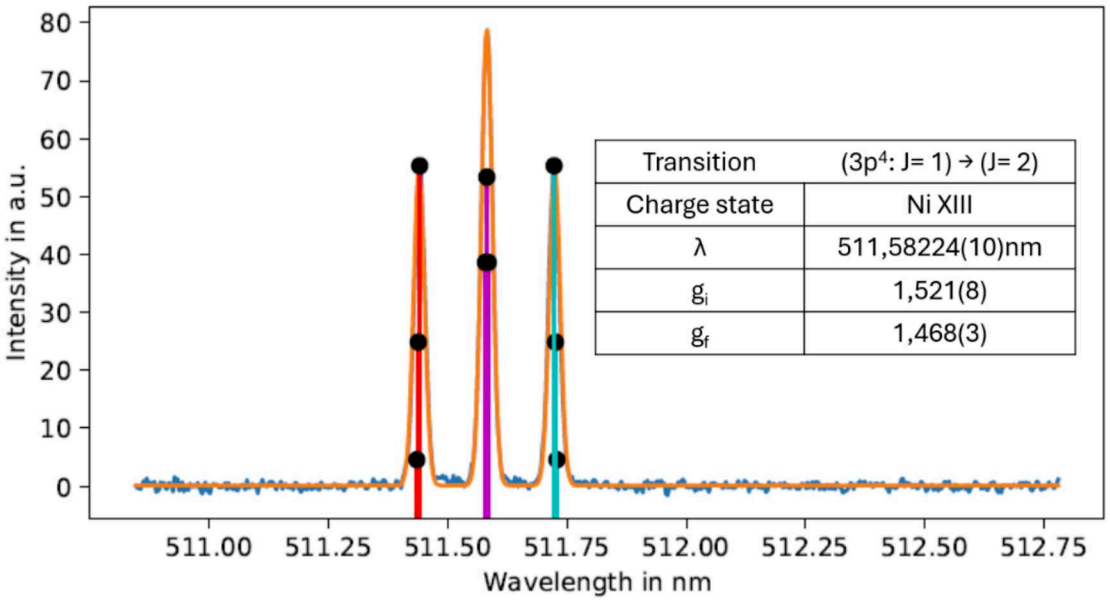

Figure 7.2.5: Zeeman fit (orange) for Ni^{12+} line at 511 nm. The different colored vertical lines show the individual components. The inset lists the central position μ in nm and the Landé g factors g_i and g_f.

The Zeeman effect produces multiple components $(\sigma^+, \sigma^-, \pi)$ for each spectral line and these were modeled by fitting a set of Gaussian functions to the individual Zeeman components [115].

$$I = \sum_{i,f} A_{\Delta m}\ CG(J_i, J_f, m_i, m_f)\ \exp\Big(- \frac{(\mu + \mu_B B(m_i g_i - m_f g_f))^2}{2\sigma^2} \Big) + c \qquad (7.6)$$

Here, $A_{\Delta m}$ is the amplitude of the Zeeman component where $\Delta m = 0, +1, -1$ for π, σ^+ and σ^- respectively, μ is the central wavelength offset, B is the magnetic field in the EBIT, g_i and g_f are the Landé g factors of the initial and the final states, σ is the Gaussian width and c is the background offset. These are the parameters that can be adjusted during the analysis. CG is the Clebsch-Gordan coefficient which represent the relative transition probability between the initial and final magnetic sublevels. To factor in the intensities of the individual peaks, the CG coefficients were multiplied by the amplitude for each polarization component.

The fitted function is shown in figure 7.2.5. The line clearly exhibits a central peak corresponding to the π (magenta) component and two symmetrically shifted σ components (red and cyan). From the fit, the final wavelength in air of the investigated transition

$$3s^2 3p^2\,{}^3P_1 \rightarrow {}^3P_2$$

of Ni^{12+} was measured to be

511.58224(10) nm.

The total uncertainty in the brackets was obtained by combining in quadrature the statistical uncertainty of the Zeeman line fit (0.00003 nm), the wavelength-calibration uncertainty (0.000077 nm) and the temperature correction uncertainty (0.000059 nm).

To check for consistency, the analysis was also performed using the vacuum wavelengths of the calibration lines from NIST instead of values in air (also listed in Table 7.2.1), yielding $\lambda_{vacuum} = 511.72481(10)$ nm. Using equation 7.3, the transition wavelength in air presented above can be converted to wavelength in vacuum, $\lambda_{vacuum} = 511.72477(10)$ nm, which agrees within the combined uncertainties. This demonstrates that the conversion from air to vacuum wavelengths is accurate within the experimental uncertainty and that the wavelength calibration is internally consistent.

7.2.4 Discussion

The measured value of the Ni^{12+} $3s^2 3p^2\,{}^3P_1 \rightarrow {}^3P_2$ transition is also in agreement with the measurement by the PTB, Germany, who reported 511.724603(10) nm [139] in vacuum. The difference between the two values corresponds to about 1.7 standard deviations. PTB determined this value using an off-resonant optical dipole force technique, which allows precise determination of the transition frequency without populating the electronically excited state. The agreement between the EBIT emission measurement and the PTB optical measurement, within the combined experimental uncertainties, with an absolute difference of 1.7×10^{-4} nm which corresponds to a relative difference of 3.3×10^{-7}, confirms the reliability of our result.

The Landé g factors can be computed using AMBiT (see 6.1.2) and can also be obtained from the experiment for well-resolved spectral lines. The inset of figure 7.2.5 presents the experimentally determined Landé g factors for both the initial and final states. A quantitative comparison with the AMBiT results is given in the Section 7.4.

Initially in this measurement campaign, the calibration was performed by a Cu-Fe-Mn-Ne lamp. In the latter part of the campaign, some additional measurements of

certain lines were performed using a Fe-Ar lamp for cross-checking. For the Ni^{12+} line at 511 nm, data were taken with both lamps, and during the later data analysis it was recognized that the Fe-Ar lamp likely provided a more reliable calibration. This may be because in the Cu-Fe-Mn-Ne lamp spectra, the usable calibration lines were not well distributed across the spectral range. Most strong lines were concentrated near the center of the detector, while only a couple of lines appeared toward the edges. Many other lines were too weak to reliably identify, limiting the number of usable calibration points. This uneven distribution may have caused the polynomial calibration model to poorly represent the wavelength scale, leading to systematic errors. Other possible contributing factors include misidentified lines or unresolved line blends, although the exact cause cannot be established. As a result, the wavelength obtained from the Cu-Fe-Mn-Ne calibration differed by several standard deviations from the PTB value, whereas the calibration using the Fe-Ar lamp yielded comparatively good agreement.

7.3 Additional Highly Charged Nickel Lines

In the following, additional spectral lines of highly charged nickel ions, measured in the same way as described above, will be discussed. For these charge states, only the total angular momentum quantum number J is available; therefore, the transitions are represented as J-only transitions. This is because the atomic structure calculations used here (FAC and AMBiT) provide reliable level energies and J values, but do not uniquely assign LS-term labels for these complex open-shell configurations. Consequently, a spectroscopic notation of the form $3s^2 3p^2\, {}^3P_1 \rightarrow {}^3P_2$, as used for Ni^{12+}, is not available for the other charge states.

The Zeeman fit for Ni^{11+} line at 423.1 nm is shown in figure 7.3.1. Ni^{11+} has five electrons in its p shell and for the transition

$$3p^5 : J = 1/2 \rightarrow J = 3/2$$

the wavelength was measured to be 423.10189(67)nm. This line was measured using the Cu-Fe-Mn-Ne lamp with the 1800 grooves/mm grating.

For Ni^{14+}, which has two electrons in the p shell, the transition

$$3p^2 : J = 2 \rightarrow J = 2$$

was measured in both first and second diffraction order. The first-order spectrum

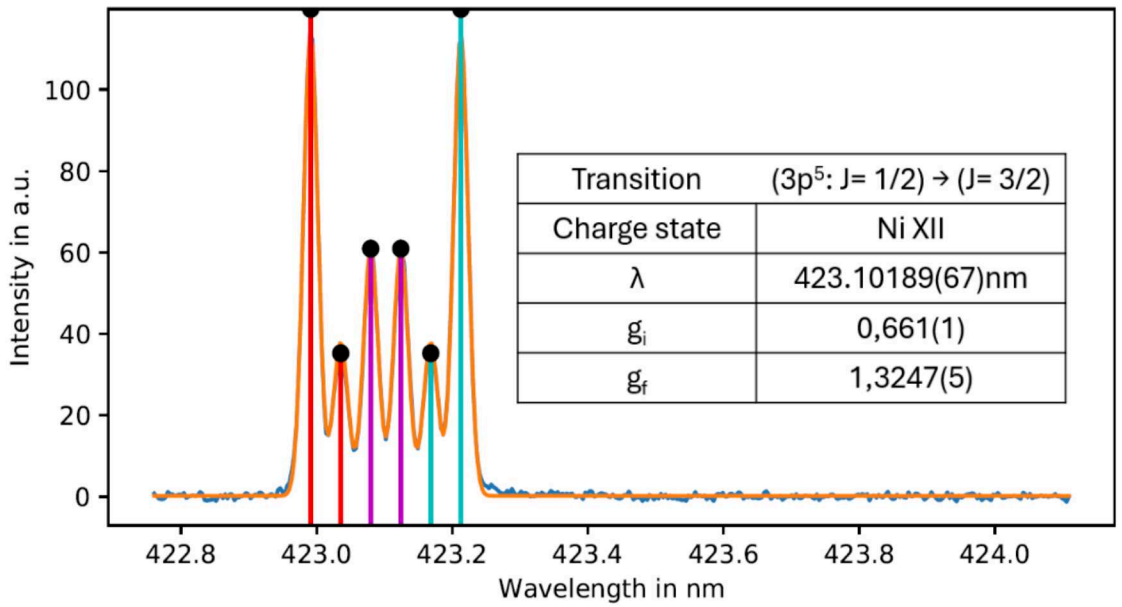

Figure 7.3.1: Zeeman fit for Ni^{11+} line at 423.1 nm using Cu-Fe-Mn-Ne as a calibration lamp and 1800 grooves/mm grating.

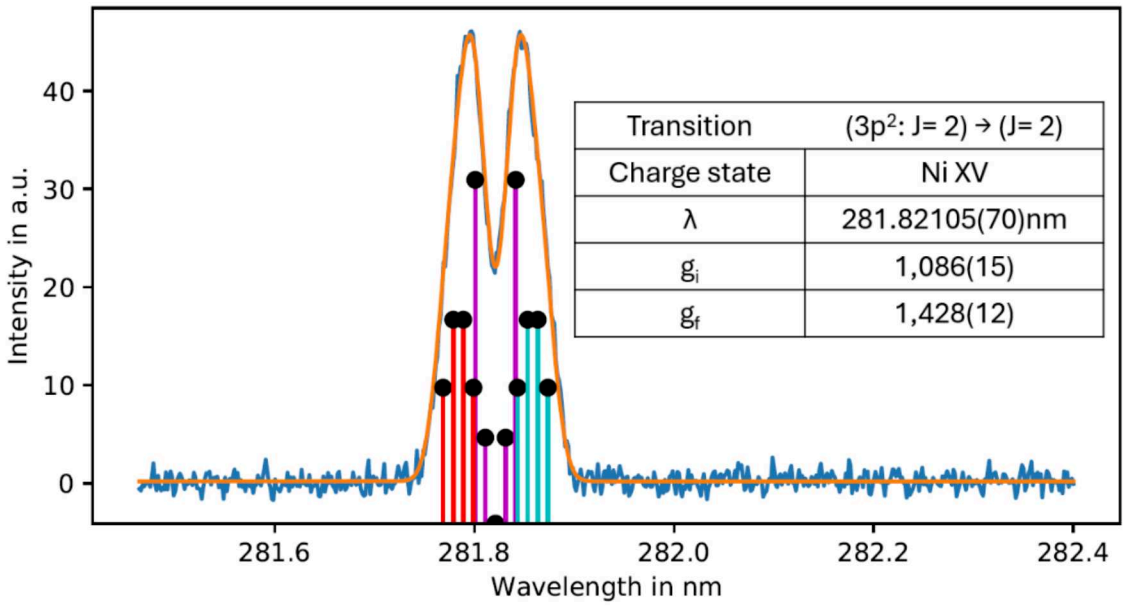

Figure 7.3.2: Zeeman fit (orange) for Ni^{14+} line at 281.8 nm using 3600 grooves/mm grating and Fe-Ar calibration.

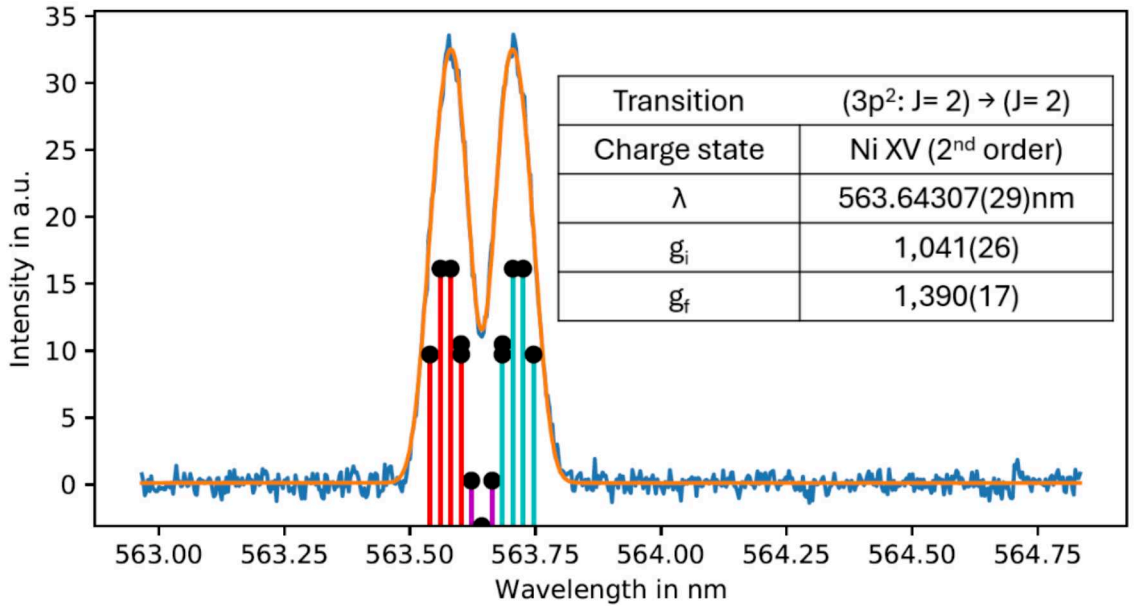

Figure 7.3.3: Zeeman fit (orange) for Ni^{14+} line at second order 563.6 nm using Cu-Fe-Mn lamp and 1800 grooves/mm grating.

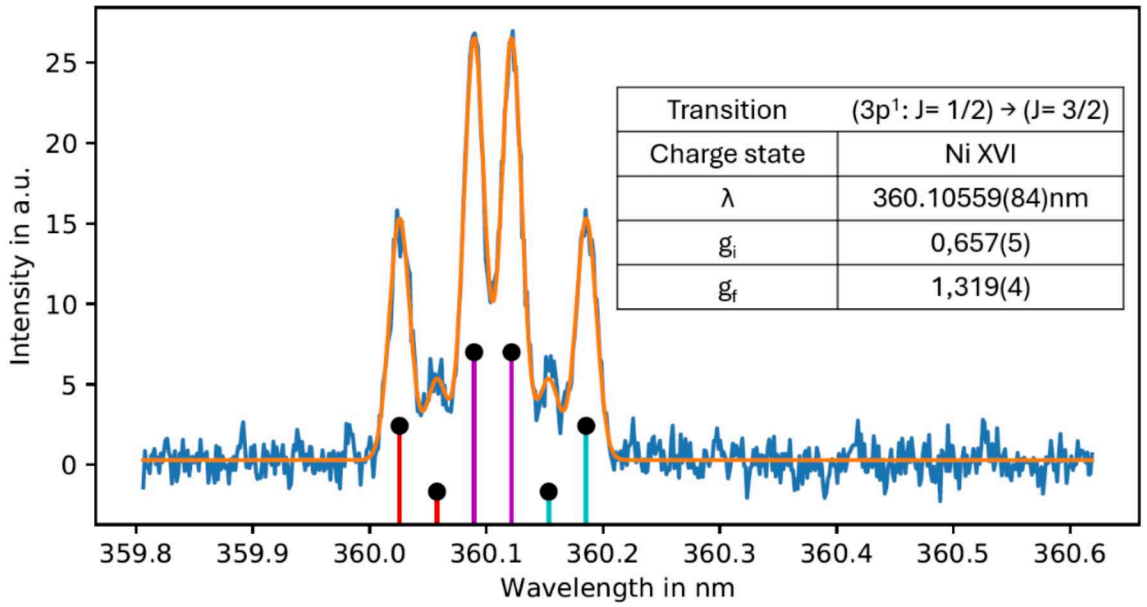

Figure 7.3.4: Zeeman fit (orange) for Ni^{15+} line at 360.1 nm using 3600 grooves/mm grating and Fe-Ar calibration.

was calibrated using the Fe-Ar lamp, whereas the second order spectrum was calibrated using the Cu-Fe-Mn-Ne lamp. The first-order wavelength was determined to be 281.82015(70) nm and the second order wavelength to be 563.64307(29) nm. Multiplying the first-order wavelength by 2 yields 563.64210(70) nm, which agrees with the directly measured second-order value within the combined uncertainties. However, despite this agreement in wavelength, the extracted Landé g-factors from the two datasets do not agree within their respective uncertainties. For the first-order spectrum, calibrated using the Fe-Ar lamp, we obtain

$$g_i = 1.086(15), \qquad g_f = 1.428(12)$$

For the second-order spectrum, calibrated using the Cu-Fe-Mn-Ne lamp, the corresponding values are

$$g_i = 1.041(26), \qquad g_f = 1.390(17)$$

Recording the spectrum with different gratings results in different dispersions and resolutions, which may have affected the detailed Zeeman line profile without significantly shifting the line centroid. Additionally, there is a possibility that one of the calibrations includes a small, unnoticed systematic effect at this wavelength.

Ni^{15+} has one electron remaining in the p shell and the transition

$$3p^1 : J = 3/2 \rightarrow J = 1/2$$

was measured to be at 360.10559(84)nm. This line was calibrated with the Fe-Ar lamp and there was no data taken with any other lamp for comparison.

7.4 Comparison of Measured and Calculated Transitions in Ni

The measured wavelengths and Landé g factors for the observed nickel charge states are listed in Table 7.4.1. The corresponding wavelengths calculated with FAC and AMBiT are given in Table 6.1.2. For easier readability, the calculated wavelengths from both codes as well as the Landé g factors obtained from AMBiT for the relevant transitions are included in Table 7.4.1. For all observed lines, a clear match can be made between experiment and theory using both the wavelength and the Landé g factors.

Ion	Transition	λ_{meas}	g factor	λ_{FAC}	λ_{AMBiT}	g factor$_{\text{AMBiT}}$	Type
Ni^{11+}	$3p^5 : J = 1/2 \rightarrow J = 3/2$	423.10189(67) nm	0.661(1), 1.3247(5)	418.1 nm	419.5 nm	0.67 , 1.33	M1
Ni^{12+}	$3s^2 3p^2\ {}^3P_1 \rightarrow {}^3P_2$	511.58224(10) nm	1.521(8), 1.468(3)	511.2 nm	512.4 nm	1.5 , 1.47	M1
$Ni^{14+}_{\text{F.O}}$	$3p^2 : J = 2 \rightarrow J = 2$	281.82015(70) nm	1.086(15), 1.428(12)	258.9 nm	267.2 nm	1.068 , 1.432	M1
$Ni^{14+}_{\text{S.O}}$	$3p^2 : J = 2 \rightarrow J = 2$	563.64307(29) nm	1.041(26), 1.390(17)	517.8 nm	534.4 nm	1.068 , 1.432	M1
Ni^{15+}	$3p^1 : J = 1/2 \rightarrow J = 3/2$	360.10559(84)	0.657(5), 1.319(4)	354 nm	353.6 nm	0.67 , 1.33	M1

Table 7.4.1: Measured transitions and Landé g factors for observed Ni charge states, together with corresponding FAC and AMBiT calculations.

For Ni^{11+}, Ni^{12+} and Ni^{15+}, the agreement between measured and calculated wavelengths is similar. The measured wavelengths differ from FAC and AMBiT values by about (0.1-1.8%), corresponding to absolute differences of roughly 0.4-6.5 nm. For Ni^{11+}, the line at 423.10189(67) nm is about 5.0 nm (1.2%) higher than the FAC value and 3.6 nm (0.9%) higher than the AMBiT value. For Ni^{12+}, the measured wavelength of 511.58224(10) nm differs from FAC and AMBiT by 0.38 nm (0.07%) and 0.82 nm (0.16%), respectively. For Ni^{15+}, the line at 360.10559(84) nm is about 6.1 nm (1.7%) higher than FAC value and 6.5 nm (1.8%) higher than the AMBiT value. For all three charge states, the measured Landé g factors differ from the calculated values by approximately 1-2% for both the initial and final levels.

For Ni^{14+}, larger wavelength differences are observed. The same $J = 2 \rightarrow 2$ transitions was measured in first and second diffraction order at 281.82105(70) nm and 563.64307(29) nm, respectively. FAC and AMBiT predict this transition at 258.9 nm and 267.2 nm. These values are lower than the measured wavelength by about 22.9 (8.1%) for FAC and 14.6 nm (5.2%) for AMBiT. Despite the larger wavelength offsets, the Landé g factors for Ni^{14+} still agree with the theoretical calculation. For the first order line, the measured values differ from the calculated values by about 2% and for the second order line the deviation is about 3%.

In summary, the level of agreement between the experiment and theory for the wavelengths and Landé g factors is consistent with earlier results for optical transitions in HCIs as reported by [115]. FAC and AMBiT are used here in a complementary way: FAC is mainly useful for predicting strong lines and their intensities, while AMBiT usually gives wavelengths closer to the measured values and provides reliable Landé g factors for the energy levels.

The same experimental procedures and calibration methods developed and tested with nickel are planned to be used for future californium spectroscopy measurements. In particular, the wavelength calibration based on reference lines from NIST and the use of Zeeman splitting to extract Landé g factors will follow the same approach. Since these methods give consistent and good results for several nickel charge states, a similar level of precision is expected for californium.

8 Conclusion and Outlook

The goal of this thesis was to move forward in the investigation of variation in fine-structure constant α. The fine-structure constant plays a fundamental role in atomic structure, determining the strength of the electromagnetic interaction and influencing atomic energy levels and transition frequencies. Any measurable temporal or spatial variation of α would have profound implications for our understanding of fundamental physics, potentially pointing toward physics beyond the Standard Model [12]. High-precision atomic clocks provide one of the most sensitive tools for probing such variations, as even extremely small changes in α can lead to detectable shifts in transition frequencies [1].

Highly charged ions are particularly attractive candidates for these investigations [54]. Due to their strong relativistic effects and enhanced sensitivity to electronic structure changes, certain transitions in HCIs exhibit large sensitivity coefficients with respect to variations in α. Among these candidates, Cf^{15+} and Cf^{17+} have been proposed as especially promising systems because of their exceptionally high sensitivity factor towards α [73].

The realization of such a clock requires precise knowledge of the relevant atomic transitions. Current theoretical predictions of the proposed clock transitions do not yet provide sufficient accuracy to directly implement a clock scheme. Experimental investigation is therefore essential to determine transition wavelengths, confirm level structures, and validate theoretical models. Optical emission spectroscopy of highly charged californium ions represents a crucial step toward this goal. EBITs provide an ideal environment for such measurements. In the trap center, HCIs are confined in a strong magnetic field, leading to Zeeman splitting of atomic levels. This splitting allows the extraction of Landé g factors from measured spectra and provides additional information about the underlying atomic structure. Moreover, relative wavelength accuracies on the order of 10^{-6} to 10^{-7} are achievable in EBIT-based spectroscopy [115, 134]. By combining precise spectroscopic measurements with theoretical calculations, it becomes possible to establish reliable level schemes for Cf^{15+} and Cf^{17+} and to identify transitions suitable for clock operation. These investigations form the experimental

basis for implementing highly charged californium ions in a precision optical clock and, ultimately, for performing competitive tests of possible variations of the fine-structure constant.

8.1 Injection system for Radioactive Elements

Owing to the radioactive nature of californium, a dedicated injection system was implemented in the Heidelberg EBIT where the optical spectroscopy of highly charged californium ions will be conducted in the future. The system is based on an adaptation of the laser desorption technique described in [64] for use in the HD-EBIT.

On account of the complexity of the HD-EBIT, arising from the presence of heat shields and the overall size, the laser-based injection system was divided into two parts: the target system and the optical setup. The target system consists of a target holder and additional rods which are attached to a manipulator. The rod assembly passes through the heat shields and extends into the trap region. The development of the injection system, including the successful insertion of the target holder into the center of the trap and the preliminary optical setup used to deliver laser beam to the target holder, is detailed in this thesis.

While the mechanical components of the injection system have been successfully implemented, the optical system remains under development. The current configuration establishes the technical feasibility of laser-based injection into the HD-EBIT, but further refinement of the beam delivery and imaging system is required. The completion of this optical setup will represent the final step toward enabling controlled injection of californium and subsequent spectroscopic investigations. Prior to introducing californium, it would be advantageous to test the injection system with well-characterized elements like lead or osmium. For this, Pb or Os can be mixed with polylactic acid on the target holder [140] which can then be used for testing.

8.2 Atomic structure calculations

Atomic structure calculations were performed using FAC and AMBiT to predict transition wavelengths, transition probabilities, and Landé g factors for highly charged nickel and californium ions. For nickel charge states ranging from Ni^{11+} to Ni^{15+}, the cal-

culated wavelengths from both methods show overall consistent predictions, typically agreeing within a few nanometers. This agreement confirms the reliability of the computational approach and supports its use for interpreting the experimentally measured nickel spectra.

The same methods were applied to californium charge states from Cf^{12+} to Cf^{19+} to identify optical transitions relevant for future spectroscopy and clock development. In particular, the magnetic dipole transitions in Cf^{15+} and Cf^{17+} were identified in the optical range, which are promising candidates for laser cooling and state detection [73]. The calculated wavelengths are overall in good agreement with previously published theoretical results, with differences on the order of a few nanometers. The calculated Landé g factors provide an important reference for comparison with experimentally measured Zeeman splittings, enabling clear identification of observed spectral lines.

8.3 Nickel Spectroscopy

In this work, optical emission spectroscopy of highly charged nickel ions was conducted as proof-of-principle for the planned californium measurements. The main focus was Ni^{12+} due to its M1 transition $3s^2 3p^2\,{}^3P_1 \rightarrow {}^3P_2$ which can be used as a logic transition for state detection of the E2 clock transition in the same charge state. The wavelength of the M1 transition was determined to be 511.58224 nm in air, corresponding to 511.72477 nm in vacuum, with an absolute uncertainty of 1.0×10^{-4} nm, which corresponds to a relative precision of about 2×10^{-7}. The result agrees, within the combined experimental uncertainties, with the PTB value obtained using a completely different technique. The data analysis of this transition can be further improved, as discrepancies in the measured wavelength were found when two different calibration lamps were used. It indicates a possible error in the analysis pipeline, most likely a misidentification of calibration lines within the dense spectrum produced by Cu-Fe-Mn-Ne lamp. Three other optical transitions in different charge states of nickel were also measured. For the second order transition in Ni^{14+}, the extracted Landé g factors deviate by up to approximately 3% from the calculated values, which is slightly larger than the deviations observed for the other transitions (up to about 2%).

The accuracy of the wavelength measurements was limited by the calibration procedure. Different calibration lamps (Fe-Ar and Cu-Fe-Mn-Ne) were used for different measurements preventing a direct cross-comparison of the wavelength. Moreover, two diffraction gratings with different grooves/mm (1800 and 3600) were used, depending

on the wavelength range accessible with each grating. As a result, it was not possible to fully assess the absolute accuracy of the measured wavelengths. Furthermore, other transitions at 670.2 nm and 802.5 nm have been measured. However, the data analysis for these transitions still remains to be carried out. Further improvements can be achieved by re-measuring nickel in HD-EBIT using multiple calibration lamps for the same transition for cross-reference. The same calibration and cross-referencing techniques will be applied to the californium measurements in order to improve their absolute wavelength accuracy.

A comparison between the measured and calculated transitions in Ni^{11+} to Ni^{15+} shows that the observed wavelengths are largely consistent with the predicted values, with differences of a few nanometers for most transitions. For Ni^{14+}, larger deviations of approximately 15-23 nm were observed between the measured and calculated wavelengths. The measured Landé g factors are also consistent with the calculated values within a few percent. The combined agreement of wavelength and Landé g factor supports the identification of the observed transitions.

8.4 Prospects for Spectroscopy of Cf ions

In addition to the planned optical spectroscopy of highly charged californium in HD-EBIT, EUV and VUV transitions (as discussed in Section 6.2.4) need to be measured to finally determine the clock transition. For the experimental investigation of the predicted EUV transitions which was shown in figures 6.2.1 and 6.2.2, a beamtime is planned at the Berliner Elektronenspeicherring-Gesellschaft für Synchrotronstrahlung (BESSY) II synchrotron facility. BESSY's advanced spectroscopic capabilities will allow for high-resolution measurements in the extreme ultraviolet range, providing critical data to validate theoretical predictions and support the identification of clock transitions in Cf^{17+}.

Atomic structure calculations of Cf^{15+} and Cf^{17+} for EUV transitions can be carried out in FAC and AMBiT, providing valuable support for the planned measurements at BESSY. In the longer term, there are plans to equip the HD-EBIT with an EUV spectrometer following the optical M1 transition campaign. This upgrade would enable in-house detection of EUV transitions in highly charged ions, expanding the experimental reach of the setup for future clock-relevant studies.

A successful spectroscopy of highly charged californium ions provides a promising path-

way towards investigations of other radioactive elements with enhanced sensitivity to variations in the fine-structure constant α such as Es^{16+} [34].

8.5 Highly Charged Cf Ion Clock

An overview of the planned clock setup was shown in Chapter 4. In an EBIT environment, the plasma temperatures are coronal which makes it difficult to do precision clock measurements. Owing to this, mini-EBITs are used as source of highly charged ion sources, which are subsequently extracted and transported to a Paul trap via a beam line. In the Paul trap, the ions are confined and cooled to millikelvin temperatures through sympathetic cooling with a co-trapped ion species. Such a system enables quantum logic spectroscopy where the internal state of the highly charged ion can be read out via its coupling to the co-trapped ion [125].

The mini-EBIT and beamline built in Heidelberg have been installed in Birmingham, where they are combined with a Paul trap provided by PTB, Germany. Highly charged ions have already been successfully retrapped in the Paul trap [120], confirming that the entire process from HCI production to trapping works as intended. This establishes the technical foundation for future clock measurements with highly charged Cf ions. A similar system is currently being prepared for Deutsches Elektronen-Synchrotron (DESY), Zeuthen. While this setup is still under construction, it follows the same concept and will provide a second location for clock experiments with highly charged ions.

In the long term, the Birmingham clock will be connected to other precision clocks in the UK network, and the DESY system will allow comparisons with optical clocks in Berlin via fiber links. Such frequency comparisons are essential for testing possible variations of the fine-structure constant and for advancing precision studies of fundamental physics.

Acknowledgments

A PhD can be an intense and demanding journey, and it is the support of the right people that makes it possible to persevere.

I would like to thank my supervisor, Steve, for giving me the opportunity to undertake this PhD and for the continued support throughout the project. Despite the geographical distance, your guidance, encouragement, and confidence in my abilities were invaluable, particularly during important stages of my research. I am grateful to José for the supervision in Heidelberg. Your expertise, insights, and willingness to engage in discussion, whether planned or spontaneous, greatly contributed to the development of this work. Many thanks to Cigdem for your valuable advice, encouragement and for sharing your experience and perspective. I would like to thank Thomas for his insights, practical tips, and encouragement whenever we spoke.

I would like to acknowledge Giovanni and his group for their important collaborative contributions. I particularly appreciate your support in sending students and postdocs to assist with our work in Heidelberg. I would like to thank Vera for your openness and willingness to share your expertise whenever I approached you with questions. My thanks also go to Julian and Mariana for your helpful explanations and for taking the time to clarify various theoretical aspects of this work during your visits.

Supportive colleagues are true gems, and I have been fortunate to be surrounded by many of them. Kostas, thank you for being a constant companion since the start of this journey. Being in the same boat, we faced many of the same challenges and supported each other through them. Our countless pep talks, shared frustrations, and small victories made the difficult days far more bearable. Yang, you have been an amazing lab and office mate. The memories we shared during both the good and challenging times are etched in my mind, reminding me to stay positive in the years ahead. Moto, you have been incredibly accommodating in matters of both science and sanity. I have learned so much from you, SOLIDWORKS, Python, physics, but most importantly, patience and a sense of calm. Elwin, much like the wonderful cakes you bring on your birthdays, your supervision has been exceptional. I truly believe there is

no one who could have guided me better throughout this PhD. Nils and Karl, working at the HD-EBIT would not have been possible without your HD-EBIT 101 lessons and continuous support. Nils, even after moving to London, you continued to help me with data analysis, for which I am especially grateful. Tobi, you will always remain the person who introduced me to the fascinating world of German politics. Christian, thank you for your help with many IT-related problems along the way. Andrea, thank you for your support with equipment and supplies, particularly for helping with the filaments for the gauge and many other practical matters. Kai, thank you for the help with the EBIT building and all the hot chocolate conversations. I would like to thank the frequency comb group for generously allowing me to borrow various optical components from their lab. I would like to thank Vera's group, especially, Melina, Finja, Magda, and Stepan, for the welcoming atmosphere and many relaxing moments on your sofa when I needed an escape from the intensity of the HD-EBIT. Before this turns into a full gratitude journal, let me say that all the students and former students of Jose and Vera have supported me in one way or another, and I am deeply grateful to each of them.

I would also like to thank the members of Steve's group in Berlin for their hospitality and the valuable interactions during my visits and conferences. Luis, thank you for the theory explanations regarding dark matter. A special thanks goes to Ulli for the wonderful Advent calendars he kindly sent to us each year.

I would also like to acknowledge the fantastic workshop at MPIK, which forms the backbone of our research by designing and manufacturing the equipment and components we rely on. The people at the main workshop, Frau Mork, Mr. Heldner, Jason, Mr. Spranz, Yannick, and Mr. Kaiser and his team, have always been incredibly helpful and patient with our requests, no matter how complicated or last-minute they were.

Special thanks to Steve, Elwin, and Moto for taking the time to proofread this thesis and for their thoughtful feedback, and to Marc and Yang for reviewing the abstract.

I would also like to thank the many teachers, mentors, and friends whose wisdom and kindness have guided me far beyond the boundaries of academia.

Finally, I would like to thank my family, my mum, my dad, my sister, and my partner for their immense emotional support. Their unwavering belief in me, their patience, and their love carried me through the most difficult moments of this PhD.

To everyone who has been part of this journey, in ways big or small, whether mentioned here or inadvertently left out: thank you for helping me push through the challenges.

Bibliography

[1] J. P. Uzan. Varying constants, gravitation and cosmology. *Living Rev. Relativ. 14, 2*, 2011.

[2] T. M. Fortier, N. Ashby, J. C. Bergquist, M. J. Delaney, S. A. Diddams, T. P. Heavner, L. Hollberg, W. M. Itano, S. R. Jefferts, K. Kim, F. Levi, L. Lorini, W. H. Oskay, T. E. Parker, J. Shirley, and J. E. Stalnaker. Precision atomic spectroscopy for improved limits on variation of the fine structure constant and local position invariance. *Phys. Rev. Lett., Vol. 98, Iss. 7, Pg. 070801*, 2007.

[3] Y. M. Yu, B. K. Sahoo, and B. B. Suo. Highly charged ion (HCI) clocks: Frontier candidates for testing variation of fine-structure constant. *Front. Phys. Vol. 11*, 2023.

[4] A. Derevianko, V. A. Dzuba, and V. V. Flambaum. Highly charged ions as a basis of optical atomic clockwork of exceptional accuracy. *Phys. Rev. Lett. 109, 180801*, 2012.

[5] M. S. Safronova, D. Budker, D. DeMille, D. F. J. Kimball, A. Derevianko, and C. W. Clark. Search for new physics with atoms and molecules. *Rev. Mod. Phys. 90, 025008*, 2018.

[6] C. P. Burgess and G. D. Moore. *The Standard Model: A Primer*. Cambridge University Press, 2006.

[7] T. Ferbel. *Techniques and Concepts of High Energy Physics X*. Springer, 1999.

[8] Wikimedia Commons. Standard model of elementary particles., 2019. `https://en.wikipedia.org/wiki/File:Standard_Model_of_Elementary_Particles.svg`.

[9] J. Ellis. Limits of the standard model. *`arXiv:hep-ph/0211168`*, 2002.

[10] J. Ellis. The superstring: theory of everything, or of nothing? *Nature 323, 595*, 1986.

[11] X. Calmet and H. Fritzsch. The cosmological evolution of the nucleon mass and the electroweak coupling constants. *Eur. Phys. J. C 24, 639*, 2002.

[12] J. P. Uzan. The fundamental constants and their variation: observational and theoretical status. *Rev. Mod. Phys., VOl 75*, 2003.

[13] E. Tiesinga, P. J. Mohr, D. B. Newell, and B. N. Taylor. CODATA recommended values of the fundamental physical constants: 2018. *Rev. Mod. Phys. 93, 025010*, 2021.

[14] A. Sommerfeld. Zur quantentheorie der spektrallinien. *Ann. Phys. 51*, 1916.

[15] D. Hanneke, S. Fogwell, and G. Gabrielse. New measurement of the electron magnetic moment and the fine structure constant. *Phys. Rev. Lett. 100, 120801*, 2008.

[16] R. Bouchendira, P. Cladé, S. Guellati-Khélifa, F. Nez, and F. Biraben. New determination of the fine structure constant and test of the quantum electrodynamics. *Phys. Rev. Lett. 106, 080801*, 2011.

[17] K. V. Klitzing, G. Dorda, and M. Pepper. New method for high-accuracy determination of the fine-structure constant based on quantized hall resistance. *Phys. Rev. Lett. 45, 494*, 1980.

[18] J. D. Bekenstein. Fine-structure constant: Is it really a constant? *Phys. Rev. D 25, 1527*, 1982.

[19] Y. V. Stadnik. New bounds on macroscopic scalar-field topological defects from nontransient signatures due to environmental dependence and spatial variations of the fundamental constants. *Phys. Rev. D 102, 115016*, 2020.

[20] M. Bartelmann. The dark universe. *Rev. Mod. Phys. Vol. 82, Iss.1*, 2010.

[21] Y. V. Stadnik and V. V. Flambaum. Can dark matter induce cosmological evolution of the fundamental constants of nature? *Phys. Rev. Lett. 115, 201301*, 2015.

[22] T Damour and J. F Donoghue. Phenomenology of the equivalence principle with light scalars. *Class. Quantum Grav. 27 202001*, 2010.

[23] T Damour and J. F Donoghue. Equivalence principle violations and couplings of a light dilaton. *Phys. Rev. D 82, 084033*, 2010.

[24] A. Arvanitaki, J. Huang, and K. V. Tilburg. Searching for dilaton dark matter with atomic clocks. *Phys. Rev. D 91, 015015*, 2015.

[25] R. Srianand, H. Chand, P. Petitjean, and B. Aracil. Limits on the time variation of the electromagnetic fine-structure constant in the low energy limit from absorption lines in the spectra of distant quasars. *Phys. Rev. Lett. 92, 121302*, 2004.

[26] M. T. Murphy, J. K. Webb, and V. V. Flambaum. Further evidence for a variable fine structure constant from Keck/HIRES QSO absorption spectra. *Mon. Not. Roy. Astron. Soc. 345*, 2003.

[27] J. A. King, J. K. Webb, M. T. Murphy, V. V. Flambaum, R. F. Carswell, M. B. Bainbridge, M. R. Wilczynska, and F. E. Koch. Spatial variation in the fine-structure constant - new results from vlt uves. *Mon. Not. Roy. Astron. Soc. Vol 422*, 2012.

[28] M. G. Kozlov, V. A. Korol, J. C. Berengut, V. A. Dzuba, and V. V. Flambaum. Space-time variation of the fine-structure constant and evolution of isotope abundances. *Phys. Rev. A 70, 062108*, 2004.

[29] P. O. Schmidt. Search for new physics with clocks. In *International Conference on Quantum Technologies for High-Energy Physics (QT4HEP22)*, 2022.

[30] A. D. Ludlow, M. M. Boyd, J. Ye, E. Peik, and P. O. Schmidt. Optical atomic clocks. *Rev. Mod. Phys. Vol 87, Issue 2*, 2015.

[31] M. G. Kozlov and D. Budker. Sensitivity coefficients to variation of fundamental constants. *https://arxiv.org/pdf/1807.08337*, 2018.

[32] Z. Tang, Y. Yu, B. K. Sahoo, C. Dong, Y. Yang, and Y. Zou. A new clock transition with the highest sensitivity to α variation and simultaneous magic trapping conditions with other clock transitions in Yb. *10.48550/arXiv.2208.09200*, 2022.

[33] G. Barontini, L. Blackburn, V. Boyer, F. Butuc-Mayer, X. Calmet, J. R. Crespo López-Urrutia, E. A. Curtis, B. Darquié, J. Dunningham, N. J. Fitch, E. M. Forgan, K. Georgiou, P. Gill, R. M. Godun, J. Goldwin, V. Guarrera, A. C. Harwood, I. R. Hill, R. J. Hendricks, M. Jeong, M. Y. H. Johnson, M. Keller, L. P. Kozhiparambil Sajith, F. Kuipers, H. S. Margolis, C. Mayo, P. Newman, A. O. Parsons, L. Prokhorov, B. I. Robertson, J. Rodewald, M. S. Safronova, B. E.

Sauer, M. Schioppo, N. Sherrill, Y. V. Stadnik, K. Szymaniec, M. R. Tarbutt, R. C. Thompson, A. Tofful, J. Tunesi, A. Vecchio, Y. Wang, and S. Worm. Measuring the stability of fundamental constants with a network of clocks. *EPJ Quantum Technol. 9, 12*, 2022.

[34] M. Safronova. The search for variation of fundamental constants with clocks. *Ann. Phys. (Berlin) 531, 1800364*, 2019.

[35] M. G. Kozlov, M. S. Safronova, J. R. Crespo López-Urrutia, and P. O. Schmidt. Highly charged ions: Optical clocks and applications in fundamental physics. *Rev. Mod. Phys., Vol 90*, 2018.

[36] T. Rosenband, D. B. Hume, P. O. Schmidt, C. W. Chou, A. Brusch, L. Lorini, W. H. Oskay, R. E. Drullinger, T. M. Fortier, J. E. Stalnaker, S. A. Diddams, W. C. Swann, N. R. Newbury, W. M. Itano, D. J. Wineland, and J. C. Bergquist. Frequency ratio of Al^+ and Hg^+ single-ion optical clocks; Metrology at the 17th decimal place. *Science Vol 319, Issue 5871*, 2008.

[37] M. Filzinger, S. Dörscher, R. Lange, J. Klose, M. Steinel, E. Benkler, E. Peik, C. Lisdat, and N. Huntemann. Improved limits on the coupling of ultralight bosonic dark matter to photons from optical atomic clock comparisons. *Phys. Rev. Lett. 130, 253001*, 2023.

[38] T. Bothwell, D. Kedar, E. Oelker, J. M. Robinson, S. L. Bromley, W. L. Tew, J. Ye, and C. J. Kennedy. Jila sri optical lattice clock with uncertainty of 2.0×10^{-18}. *Metrologia 56, 065004*, 2019.

[39] W. F.Mcgrew, X. Zhang, R. J. Fasano, S. A. Schäffer, K. Beloy, D. Nicolodi, R. C. Brown, N. Hinkley, G. Milani, M. Schioppo, T. H. Yoon, and A. D. Ludlow. Atomic clock performance enabling geodesy below the centimetre level. *Nature 564, 87*, 2018.

[40] N. Ohmae, M. Takamoto, Y. Takahashi, M. Kokubun, K. Araki, A. Hinton, I. Ushijima, T. Muramatsu, T. Furumiya, and Y. Sakai. Transportable strontium optical lattice clocks operated outside laboratory at the level of 10^{-18} uncertainty. *Adv. Quantum Technol. 4, 2100015*, 2021.

[41] S. M. Brewer, J.-S. Chen, A. M. Hankin, E. R. Clements, C. W. Chou, D. J. Wineland, D. B. Hume, and R. D. Leibrandt. $^{27}Al^+$ quantum-logic clock with a systematic uncertainty below 10^{-18}. *Phys. Rev. Lett. 123, 033201*, 2019.

[42] A. D. Ludlow, T. Zelevinsky, G. K. Campbell, S. Blatt, M. M. Boyd, M. H. G. de Miranda, M. J.Martin, J.W. Thomsen, S.M. Foreman, J. Ye, T.M. Fortier, J. E. Stalnaker, S. A. Diddams, Y. Le Coq, Z. W. Barber, N. Poli, N. D. Lemke, K. M. Beck, , and C.W. Oates. Sr lattice clock at 1×10^{-16} fractional uncertainty by remote optical evaluation with a ca clock. *Science 319, 1805*, 2008.

[43] T. E. Mehlstäubler, G. Grosche, C. Lisdat, P. O. Schmidt, and H. Denker. Atomic clocks for geodesy. *Reports on Progress in Physics, 81, 064401*, 2018.

[44] M. Takamoto, I. Ushijima, N. Ohmae, T. Yahagi, K. Kokado, H. Shinkai, and H. Katori. Test of general relativity by a pair of transportable optical lattice clocks,. *Nat. Photon. 14, 411*, 2020.

[45] B. Edlén. Die deutung der Emissionslinien im Spektrum der Sonnenkorona. *Z. Astrophys. 22, p. 30*, 1943.

[46] P. Beiersdorfer. Laboratory x-ray astrophysics. *Annu. Rev. Astron. Astrophys. 41, 343*, 2003.

[47] P. Beiersdorfer and G. V. Brown. Experimental study of the x-ray transitions in the heliumlike isoelectronic sequence: Updated results. *Phys. Rev. A 91, 032514*, 2015.

[48] Y. Zou, R. Hutton, F. Currell, I. Martinson, and S. Hagmann. *Handbook for Highly Charged Ion Spectroscopic Research.* CRC Press., 2012.

[49] I. Martinson. The spectroscopy of highly ionised atoms. *Rep. Prog. Phys. 52 157*, 1989.

[50] S. Sturm, M. Vogel, F. Köhler-Langes, W. Quint, K. Blaum, and G. Werth. High-precision measurements of the bound electron′s magnetic moment. *Atoms 5(1),4*, 2017.

[51] M. I. Eides, H. Grotch, and V. Shelyuto. Theory of light hydrogenlike atoms. *Phys. Rep. 342, 63*, 2001.

[52] J. C. Berengut, V. A. Dzuba, and V. V. Flambaum. Transitions in Zr, Hf, Ta, W, Re, Hg, Ac, and U ions with high sensitivity to variation of the fine-structure constant. *Phys. Rev. A 84, 054501*, 2011.

[53] J. C. Berengut, V. A. Dzuba, V. V. Flambaum, and A. Ong. Highly charged ions with E1, M1 and E2 transitions within laser range. *Phys. Rev. A 86, 022517*, 2012.

[54] J. C. Berengut, V. A. Dzuba, and V. V. Flambaum. Enhanced laboratory sensitivity to variation of the fine-structure constant using highly charged ions. *Phys. Rev. Lett. 105, 120801*, 2010.

[55] A. Derevianko and M. Pospelov. Hunting for topological dark matter with atomic clocks. *Nature Phys 10, 933*, 2014. https://doi.org/10.1038/nphys3137.

[56] M. A. Levine, R. E. Marrs, J. R. Henderson, D. A. Knapp, and M. B. Schneider. The electron beam ion trap: A new instrument for atomic physics measurements. *Phys. Scr. T 22 157*, 1988.

[57] R. Geller. *Electron Cyclotron Resonance Ion Sources and ECR Plasmas*. Routledge, 1996. https://doi.org/10.1201/9780203758663.

[58] A. Windberger, F. Torretti, A. Borschevsky, A. Ryabtsev, S. Dobrodey, H. Bekker, E. Eliav, U. Kaldor, and W. Ubachs. Analysis of the fine structure of $Sn^{11+} - Sn^{14+}$ ions by optical spectroscopy in an electron-beam ion trap. *Phys. Rev. A 94, 012506*, 2016.

[59] C. Biedermann, R. Radtke, G. Fußmann, J. L. Schwob, and P. Mandelbaum c. Euv spectroscopy of highly charged xenon ions. *Nucl. Instrum. Methods Phys. Res. B 235, 126*, 2005.

[60] M. Vilkas, Y. Ishikawa, and E. Träbert. Prominent soft x-ray lines of Sr-like Au^{41+} in low-energy ebit spectrum. *J. Phys.: Conf. Ser. 58 101*, 2007.

[61] S. C. Sanders, R. Silwal, B. H. Rudramadevi, A. C. Gall, and E. Takacs. High-resolution x-ray spectroscopy of highly charged tungsten ebit plasma. *Nucl. Instrum. Methods Phys. Res. B 431, 47*, 2018.

[62] S. W. Epp, J. R. Crespo López-Urrutia, G. Brenner, V. Mäckel, P. H. Mokler, R. Treusch, M. Kuhlmann, M. V. Yurkov, J. Feldhaus, and J. R. Schneider. Laser spectroscopy on trapped highly-charged ions using soft x-rays from flash. *J. Phys.: Conf. Ser. 88 012059*, 2007.

[63] D. Schneider, D. A. Church, G. Weinberg, J. Steiger, B. Beck, J. McDonald, E. Magee, and D. Knapp. Confinement in a cryogenic penning trap of highest charge state ions from EBIT. *Rev. Sci. Instrum. 65, 3472*, 1994.

[64] L. Schmöger, M. Schwarz, T. M. Baumann, O. O. Versolato, B. Piest, T. Pfeifer, J. Ullrich, P. O. Schmidt, and J. R. Crespo López-Urrutia. Deceleration, precooling, and multi-pass stopping of highly charged ions in Be^+ coulomb crystals. *Rev. Sci. Instrum. 86, 103111*, 2015.

[65] W. H. Baldwin. The story of nickel. I. How "Old Nick's" gnomes were outwitted. *Jour. Chem. Ed. Vol8 Iss 9*, 1931.

[66] Y. M. Yu and B. K. Sahoo. Selected highly charged ions as prospective candidates for optical clocks with quality factors larger than 10^{15}. *Phy.Rev. A 97, 041403(R)*, 2018.

[67] J. Prochaska, J. Howk, and A. Wolfe. The elemental abundance pattern in a galaxy at z = 2.626. *Nature 423, 57*, 2003.

[68] J. K. Webb, J. A. King, M. T. Murphy, V. V. Flambaum, R. F. Carswell, and M. B. Bainbridge. Indications of a spatial variation of the fine structure constant. *Phys. Rev. Lett. 107, 191101*, 2011.

[69] S. G. Thompson, Jr. K. Street, A. Ghiorso, and G. T. Seaborg. The new element californium (atomic number 98). *Phys. Rev. Vol 80, Number 5*, 1950.

[70] K. Street Jr., S. G. Thompson, and G. T. Seaborg. Chemical properties of californium. *J. Am. Chem. Soc. 72(10)*, 1950.

[71] E. K. Hulet, S. G. Thompson, and A. Ghiorso. Isotopes of curium, berkelium, and californium. *Phys. Rev. 95, 1703*, 1954. `https://doi.org/10.1103/PhysRev.95.1703`.

[72] R. G. Haire. *The Chemistry of the Actinide and Transactinide Elements.* Springer, 2008.

[73] S. G. Porsev, U. I. Safronova, M. S. Safronova, P. O. Schmidt, A. I. Bondarev, M. G. Kozlov, I. I. Tupitsyn, and C. Cheung. Optical clocks based on the Cf^{15+} and Cf^{17+} ions. *Phys. Rev. A 102, 012802*, 2020.

[74] R. M. Godun, P. B. R. Nisbet-Jones, J. M. Jones, S. A. King, L. A. M. Johnson, H. S. Margolis, K. Szymaniec, S. N. Lea, and K. Bongs. Frequency ratio of two optical clock transitions in $^{171}Yb^+$ and constraints on the time variation of fundamental constants. *Phys. Rev. Lett. 113, 210801*, 2014. `https://doi.org/10.1103/PhysRevLett.113.210801`.

[75] P. Wcisło, P. Morzyński, M. Bober, A. Cygan, D. Lisak, R. Ciuryło, and M. Zawada. Experimental constraint on dark matter detection with optical atomic clocks. *Nat Astron 1, 0009*, 2017.

[76] A. Hees, J. Guéna, M. Abgrall, S. Bize, and P. Wolf. Searching for an oscillating massive scalar field as a dark matter candidate using atomic hyperfine frequency comparisons. *Phys. Rev. Lett. 117, 061301*, 2016.

[77] T. M. Fortier, A. N. Luiten, and H. S. Margolis. Optical atomic clocks: defining the future of time and frequency metrology. *Optica 13, 143−163*, 2026.

[78] O. Lopez, F. Kéfélian, H. Jiang, A. Haboucha, A. Bercy, F. Stefani, B. Chanteau, A. Kanj, D. Rovera, J. Achkar, C. Chardonnet, P. E. Pottie, A. Amy-Klein, and G. Santarell. Frequency and time transfer for metrology and beyond using telecommunication network fibres. *C. r., Phys., Vol 16, Iss. 5, Pg 531*, 2015.

[79] F. Meng, Y. Lin, Z. Fang, and Z. Zhang. Remote Sr optical clock comparison with 10^{-17} fractional instability through a 54 km urban fiber link. *Opt. Commun. Vol. 583, 131712*, 2025.

[80] A. Derevianko. Detecting dark-matter waves with a network of precision-measurement tools. *Phys. Rev. A 97, 042506*, 2018.

[81] S. Pustelny, D. F. Jackson Kimball, C. Pankow, M. P. Ledbetter, P. Wlodarczyk, P. Wcislo, M. Pospelov, J. R. Smith, J. Read, W. Gawlik, and D. Budker. The global network of optical magnetometers for exotic physics (gnome): A novel scheme to search for physics beyond the standard model. *Annalen der Physik 525(8 − 9), 659*, 2013. https://doi.org/10.1002/andp.201300061.

[82] P. Kómár, E. M. Kessler, M. Bishof, L. Jiang, A. S. Sørensen, J. Ye, and M. D. Lukin. A quantum network of clocks. *Nat. Phys. 10, 582*, 2014. https://doi.org/10.1038/nphys3000.

[83] B. M. Roberts, P. Delva, A. Al-Masoudi, A. Amy-Klein, C. Bærentsen, C. F. A. Baynham, E. Benkler, S. Bilicki, S. Bize, W. Bowden, J. Calvert, V. Cambier, E. Cantin, E. A. Curtis, S. Dörscher, M. Favier, F. Frank, P. Gill, R. M. Godun, G. Grosche, C. Guo, A. Hees, I. R. Hill, R. Hobson, N. Huntemann, J. Kronjäger, S. Koke, A. Kuhl, R. Lange, T. Legero, B. Lipphardt, C. Lisdat, J. Lodewyck, O. Lopez, H. S. Margolis, H. Álvarez-Martínez, F. Meynadier, F. Ozimek, E. Peik, P.-E. Pottie, N. Quintin, C. Sanner, L. De Sarlo, M. Schioppo, R. Schwarz, A. Silva, U. Sterr, Chr. Tamm, R. Le Targat, P. Tuckey, G. Vallet, T. Waterholter,

D. Xu, and P. Wolf. Search for transient variations of the fine structure constant and dark matter using fiber-linked optical atomic clocks. *New J. Phys. 22 093010*, 2020. https://doi.org/10.1088/1367-2630/abaace.

[84] F. Riehle. Optical clock networks. *Nat. Photon. 11, 25–31*, 2017.

[85] T. Lindvall, M. Pizzocaro, R. M. Godun, M. Abgrall, D. Akamatsu, A. Amy-Klein, E. Benkler, N. M. Bhatt, D. Calonico, E. Cantin, E. Cantoni, G. Cerretto, C. Chardonnet, M. A. C. Marin, C. Clivati, S. Condio, E. A. Curtis, H. Denker, S. Donadello, S. Dörscher, C.-H. Feng, M. Filzinger, T. Fordell, I. Goti, K. Hanhijärvi, H. N. Hausser, I. R. Hill, K. Hosaka, N. Huntemann, M. Y. H. Johnson, J. Keller, J. Klose, T. Kobayashi, S. Koke, A. Kuhl, R. Le Targat, T. Legero, F. Levi, B. Lipphardt, C. Lisdat, H. Liu, J. Lodewyck, O. Lopez, M. M-Laurol, T. E. MehlstÃ¤ubler, A. Mura, A. Nishiyama, T. Nordmann, A. O. Parsons, G. Petit, B. Pointard, P.-E. Pottie, M. Risaro, B. I. Robertson, M. Schioppo, H. Shang, K. Stahl, M. Steinel, U. Sterr, A. Tofful, M. Tønnes, D.-B.-A. Tran, J. Tunesi, A. E. Wallin, and H. S. Margolis. Coordinated international comparisons between optical clocks connected via fiber and satellite links. *Optica 12, No. 6*, 2025.

[86] G. Barontini, V. Boyer, X. Calmet, N. J. Fitch, E. M. Forgan, R. M. Godun, J. Goldwin, V. Guarrera, I. R. Hill, M. Jeong, M. Keller, F. Kuipers, H. S. Margolis, P. Newman, L. Prokhorov, J. Rodewald, B. E. Sauer, M. Schioppo, N. Sherrill, M. R. Tarbutt, A. Vecchio, and S. Worm. Qsnet, a network of clocks for measuring the stability of fundamental constants. *Proc. SPIE*, 11881:118810K, 2021. https://doi.org/10.1117/12.2600493.

[87] C. Foot. *Atomic Physics*. Oxford University Press, USA, 2005.

[88] D. J. Griffiths and D. F. Schroeter. *Introduction to Quantum Mechanics*. Cambridge University Press, 2018.

[89] D. J. Griffiths. *Introduction to elementary particles*. Wiley, 2008.

[90] H. E. White. *Introduction to Atomic Spectra*. McGraw-Hill Book Company Inc, 1934.

[91] P. A. M. Dirac. The quantum theory of the electron. *Proc. R. Soc. Lond. A Vol.117*, 1928.

[92] B. H. Bransden and C. J. Joachain. *Physics of atoms and molecules*. Longman Group Limited, 1983.

[93] J. D. Gillaspy. Highly charged ions. *J. Phys. B: At. Mol. Opt. Phys. 34 R93*, 2001.

[94] H. F. Beyer and V. P. Shevelko. *Introduction to the Physics of Highly Charged Ions (1st ed.)*. CRC Press, 2002. https://doi.org/10.1201/9781420034097.

[95] G. W. F. Drake. *Springer Handbook of Atomic, Molecular, and Optical Physics*. Springer, 1996.

[96] W. C. Martin and W. L. Wiese. Atomic spectroscopy. https://www.nist.gov/system/files/documents/2016/10/03/atspec.pdf.

[97] J. C. Berengut, V. A. Dzuba, V. V. Flambaum, and A. Ong. Electron-hole transitions in multiply charged ions for precision laser spectroscopy and searching for variations in α. *Phys. Rev. Lett.*, 106:210802, 2011. https://doi.org/10.1103/PhysRevLett.106.210802.

[98] J. C. Berengut, V. A. Dzuba, V. V. Flambaum, and A. Ong. Optical transitions in highly charged californium ions with high sensitivity to variation of the fine-structure constant. *Phys. Rev. Lett. 109, 070802*, 2012.

[99] W. Quint and M. Vogel. *Fundamental Physics in Particle Traps*. Springer, 2014.

[100] W. Lotz. An empirical formula for the electron-impact ionization cross-section. *Z. Physik 206, 205*, 1967. https://doi.org/10.1007/BF01325928.

[101] Y. S. Kim and R. H. Pratt. Direct radiative recombination of electrons with atomic ions: Cross sections and rate coefficients. *Phys. Rev. A 27, 2913*, 1983.

[102] M. F. Gu. The flexible atomic code. *Can. J. Phys. Vol. 86. no. 5*, 2008.

[103] E. V. Kahl and J. C. Berengut. Ambit: A programme for high-precision relativistic atomic structure calculations. *Comput. Phys. Commun. Vol. 238, p. 232*, 2019.

[104] C. D. Sherrill. An introduction to configuration interaction theory, 1995. https://api.semanticscholar.org/CorpusID:36966081.

[105] B. O. Roos. *Lecture Notes in Quantum Chemistry*. Springer, 1992.

[106] E. D. Donets. Ussr inventor's certificate no. 248860. Byull. OIPOTZ No. 23 (1969) 65, 1967. USSR Inventor's Certificate.

[107] J. R. Crespo López-Urrutia, A. Dorn, R. Moshammer, and J. Ullrich. The freiburg electron beam ion trap/source project FreEBIT. *Phys. Scr. 1999 502*, 1999.

[108] J. R. Crespo López-Urrutia, J. Braun, G. Brenner, H. Bruhns, C. Dimopoulou, I. N. Draganic; D. Fischer, A. J. Gonzaĺez Martińez, A. Lapierre, and V. Mironov. Progress at the Heidelberg EBIT. *J. Phys.: Conf. Ser. 2 42*, 2004.

[109] J. R. Crespo López-Urrutia, B. Bapat, I. Draganić, B. Feuerstein, D. Fischer, H. Lorch, R. Moshammer, and J. Ullrich. Physics with highly-charged ions in an ebit. *Hyperfine Interact. 149, 109 − 113*, 2003.

[110] G. Hermann. Optical theory of thermal velocity effects in cylindrical electron beams. *J. Appl. Phys. 29, 127*, 1958.

[111] G. Zschornacka, M. Schmidt, and A. Thorn. Electron beam ion sources, 2014.

[112] H. Bekker. *Optical and EUV spectroscopy of highly charged ions near the 4f to 5s level crossing*. PhD thesis, Ruperto-Carola-University of Heidelberg, Germany, 2016.

[113] R. E. Marrs, P. Beiersdorfer, and D. Schneider. The electron beam ion trap. *Phys Today 47 (10), 27*, 1994.

[114] M. A. Levine, R. E. Marrs, C. L. Bennett, J. R. Henderson, D. A. Knapp, and M. B. Schneider. Ebit: Electron beam ion trap. *AIP Conf. Proc. 188, 82*, 1989.

[115] N. Rehbehn. *Measurement of highly chargedCa and Xe ions and their sensitivity to a hypothetical fifth force beyond the Standard Model*. PhD thesis, University of Heidelberg, Germany, 2023.

[116] ChemBK. Powerful online chemical database for pc, pad and phone. Available from `https://www.chembk.com/en/chem/41749-92-2`.

[117] E. Popov. *Introduction to Diffraction Gratings Summary of Applications*. AMU (PUP), 2012. `https://hal.science/hal-00765101v1`.

[118] P. Micke, S. Kühn, L. Buchauer, J. R. Harries, T. M. Bücking, K. Blaum, A. Cieluch, A. Egl, D. Hollain, S. Kraemer, T. Pfeifer, P. O. Schmidt, R. X. Schüssler, C.Schweiger, T. Stöhlker, S. Sturm, R. N. Wolf, S. Bernitt, and J. R. Crespo López-Urrutia. The heidelberg compact electron beam ion traps. *Rev. Sci. Instrum. 89, 063109*, 2018.

[119] H. Khodja and J. P. Briand. A warm electron beam ion trap: the micro-EBIT. *Phys. Scr. Vol. T71, 113-116*, 1997.

[120] L Prokhorov, A. A. Smith, M. Xu, K. Georgiou, V. Guarrera, L. P. Kozhiparambil Sajith, E. A. Dijck, C. Warnecke, M. Wehrheim, A. Wilzewski, L. Blackburn, M. Keller, V. Boyer, T. Pfeifer, U. Schwanke, C. Issever, S. Worm, P. O. Schmidt, J. R. Crespo Lopez-Urrutia, and G. Barontini. Coulomb crystallization of xenon highly charged ions in a laser-cooled Ca^+ matrix. *arXiv*, 12 2025. `https://doi.org/10.48550/arXiv.2512.12266`.

[121] H. Kreckel, H. Bruhns, K. A. Miller, E. Wåhlin, A. Davis, S. Höckh, and D. W. Savin. A simple double-focusing electrostatic ion beam deflector. *Rev. Sci. Instrum., vol. 81, no. 6, p. 063304*, 2010.

[122] M. Wehrheim. Characterization of be^+ and highly charged ion dynamics in a cryogenic paul trap. Master's thesis, University of Heidelberg, Germany, 2022.

[123] J. Stark. *An Ultralow-Noise Superconducting Radio-Frequency Ion Trap for Frequency Metrology with Highly Charged Ions.* PhD thesis, Ruperto-Carola-University of Heidelberg, Germany, 2020.

[124] P. O. Schmidt, T. Rosenband, J. C. J. Koelemeij, D. B. Hume, W. M. Itano, J. C. Bergquist, and D. J. Wineland. Spectroscopy of atomic and molecular ions using quantum logic. *AIP Conf. Proc. 862, 305−312*, 2006.

[125] T. Leopold, S. A. King, P. Micke, A. Bautista-Salvador, J. C. Heip, C. Ospelkaus, J. R. Crespo L/'opez-Urrutia, and P. O. Schmidt. A cryogenic radio-frequency ion trap for quantum logic spectroscopy of highly charged ions. *arXiv:1901.03082*, 2019.

[126] S. M. Brewer, J.-S. Chen, A. M. Hankin, E. R. Clements, C. W. Chou, D. J. Wineland, D. B. Hume, and D. R. Leibrandt. $^{27}Al^+$ Quantum-Logic Clock with a Systematic Uncertainty below 10^{-18}. *Phys. Rev. Lett. 123, 033201*, 2023.

[127] S. Chen, Z. Zhou, J. Li, T. Zhang, C. Li, T. Shi, Y. Huang, K. Gao, and H. Guan. Precision measurement of m1 optical clock transition in Ni^{12+}. *Phys. Rev. Res. 6, 013030*, 2024.

[128] Ch. Schweiger, C. M. König, J. R. Crespo López-Urrutia, M. Door, H. Dorrer, Ch. E. Düllmann, S. Eliseev, P. Filianin, W. Huang, K. Kromer, P. Micke, M. Müller, D. Renisch, A. Rischka, Z. X. Schüssler, and K. Blaum. Production of

highly charged ions of rare species by laser-induced desorption inside an electron beam ion trap. *Rev. Sci. Instrum. 90, 123201)*, 2019.

[129] D. Renisch, C. E. Düllmann, R. Abrosimov, K. Eberhardt, B. Kindler, B. Lommel, J. Lukacova, C. Mokry, S. Oberstedt, I. Pohjalainen, J. Runke, T. Schwab, and C. Sirleaf. Actinide and lanthanide thin-layer developments using a drop-on-demand printing system. *EPJ Web of Conferences 285, 04001*, 2023.

[130] R. Haas, S. Lohse, Ch. E. Düllmann, K. Eberhardt, C. Mokry, and J. Runke. Development and characterization of a Drop-on-Demand inkjet printing system for nuclear target fabrication. *Nucl. Instrum. Methods Phys. Res. A 874, 43–49*, 2017.

[131] M. B. Schneider, M. A. Levine, C. L. Bennett, J. R. Henderson, D. A. Knapp, and R. E. Marrs. Evaporative cooling of highly charged ions in ebit: An experimental realization. *AIP Conf. Proc. 188, 158*, 1989.

[132] J. S. Lilley. *Nuclear Physics Principles and Applications.* John Wiley and Sons Ltd, 2001.

[133] Radioactive human body. `https://sciencedemonstrations.fas.harvard.edu/`.

[134] M. Rosner. *Electronic energy level determination in the 4f-subshell in highly charged lead and the 5d-subshell in highly charged bismuth by atomic structure calculation-assisted optical spectroscopy.* PhD thesis, University of Heidelberg, Germany, 2024.

[135] B. E. Saleh and M. C. Teich. *Fundamentals of photonics.* Wiley Online Library, 1991.

[136] I. L. Rusakova, Y. Y. Rusakov, and L. B. Krivdin. Theoretical grounds of relativistic methods for calculation of spin spin coupling constants in nuclear magnetic resonance spectra. *Russ. Chem. Rev. 85, p.356*, 2016.

[137] A. Kramida, Y. Ralchenko, J. Reader, and NIST ASD Team. Nist atomic spectra database.

[138] E. R. Peck and K. Reeder. Dispersion of air. *J. Opt. Soc. Am. 62,* 958 – 962, 1972.

[139] C. Cheung, S. G. Porsev, D. Filin, M. S. Safronova, M. Wehrheim, L. J. Spieß, S. Chen, A. Wilzewski, and J. R. Crespo López-Urrutia. Finding the Ultranarrow $^3P_2 \rightarrow {}^3P_0$ Electric Quadrupole Transition in Ni^{12+} Ion for an Optical Clock. *Phys. Rev. Lett. 135, 093002*, 2025.

[140] Ch. Schweiger. *High-Precision Penning-Trap Determination of the Electron Capture Q-Value in ^{163}Ho for the Determination of the Electron Neutrino Mass*. PhD thesis, University of Heidelberg, Germany, 2024.

A Appendix

A.1 FAC Input Configurations for Ni and Cf

This section lists the specific configurations used in the FAC calculations for Ni^{11+} to Ni^{15+}.

Charge state	Ground state	Excited states
Ni^{11+}	`Config('g0', '3p5')`	`Config('e1', '3p4 3d1')`
		`Config('e2', '3p3 3d2')`
		`Config('e3', '3p2 3d3')`
		`Config('e4', '3p1 3d4')`
Ni^{13+}	`Config('g0', '3p3')`	`Config('e1', '3p2 3d1')`
		`Config('e2', '3p1 3d2')`
Ni^{14+}	`Config('g0', '3p2')`	`Config('e1', '3p1 3d1')`
Ni^{15+}	`Config('g0', '3s2 3p1')`	`Config('e1', '3s1 3p2')`
		`Config('e2', '3s1 3d2')`
		`Config('e3', '3s2 3d1')`
		`Config('e4', '3s1 3p1 3d1')`

Table A.1.1: The closed-shell configuration from Ni^{11+} to Ni^{14+} is `Closed('1s', '2s', '2p', '3s')`. However, the 3s shell is opened in the case of Ni^{15+}.

Table A.1.2 lists the electronic configurations associated with the ground and selected excited states of Cf^{12+} to Cf^{19+}.

Charge state	Ground state	Excited states
Cf^{12+}	Config('g0', '6p4 5f2')	Config('e1', '6p4 6d1 5f1')
		Config('e2', '6p4 7s1 5f1')
Cf^{13+}	Config('g0', '6p3 5f2')	Config('e1', '6p3 6d1 5f1')
		Config('e2', '6p3 7s1 5f1')
Cf^{14+}	Config('g0', '5f2 6p2')	Config('e1', '5f3 6d1')
		Config('e2', '5f3 6p1')
		Config('e3', '5f2 6p1 6d1')
		Config('e4', '5f2 6p1 7s1')
Cf^{15+}	Config('g0', '6p2 5f1')	Config('e1', '6p1 5[f,g]2')
		Config('e2', '6p2 5g1')
		Config('e3', '6p3')
		Config('e4', '6[p,d,f,g]3')
		Config('e5', '6p2 7*1')
		Config('e6', '6p2 8*1')
Cf^{16+}	Config('g0', '6s2 6p1 5f1')	Config('e1', '6s2 6p1 5g1')
		Config('e2', '6s2 6[p,d,f,g,h]2')
		Config('e3', '6s2 6p1 7s1')
		Config('e4', '6s2 5[f,g]2')
		Config('e5', '6s2 7[s,p,d,f,g,h,i]2')
Cf^{17+}	Config('g0', '6s2 5f1')	Config('e1', '6s2 6[p,d,f,g,h]1')
		Config('e2', '6s2 5[g]1')
		Config('e3', '6s2 7[s,p,d,f]1')
		Config('e4', '6s2 8[s,p]1')
		Config('e5', '6s1 6[p,d,f,g,h]2')
		Config('e6', '6s1 5[f,g]2')
		Config('e7', '6s1 7[s,p,d,f,g,h]2')
		Config('e8', '6s1 8[s,p,d,f,g,h]2')
		Config('e9', '6s1 6p1 5f1')
		Config('e10', '6s1 6p1 7s1')
		Config('e11', '6s1 5f1 7s1')
		Config('e12', '6s1 7s1 8s1')
Cf^{18+}	Config('g0', '6s2')	Config('e1', '5[f,g]2')
		Config('e2', '6[p,d,f,g,h]2')
		Config('e3', '7[s,p,d,f,g,h,i]2')
		Config('e4', '6s1 5[f,g]1')
		Config('e5', '6s1 6[p,d,f,g,h]1')
		Config('e6', '6s1 7[s,p,d,f,g,h,i]1')
Cf^{19+}	Config('g0', '6s1')	Config('e1', '5[f,g]1')
		Config('e2', '6[p,d,f,g,h]1')
		Config('e3', '7[s,p,d,f,g,h,i]1')

Table A.1.2: Overview of the electronic configurations corresponding to the ground and selected excited states of Cf^{12+} to Cf^{19+} ions. Excited configurations highlight possible transitions involving 6p, 5f, 6d, 7s, and higher orbitals.

A.2 AMBiT Ni^{12+} Input File

Below is the AMBiT input file used for the calculation:

```
ID = NiXIII

Z = 28

-s123

[Lattice]
NumPoints = 1000
StartPoint = 1.0e-6
EndPoint = 20.0

[HF]
--breit


N = 16
Configuration = '1s2 2s2 2p6 3s2: 3p1.33 3p+2.67'

[Basis]
--bspline-basis
BSpline/N = 40
BSpline/K = 9
ValenceBasis = 6spdfgh
IncludeValence = 3s

[CI]
LeadingConfigurations = '3p4'
ElectronExcitations = 2
EvenParityTwoJ = '0, 2, 4, 6, 8, 10, 12'
OddParityTwoJ = '0, 2, 4, 6, 8, 10, 12'
NumSolutions = 8

[MBPT]
Basis = 30spdfgh

[Transitions]
M1/AllBelow = -0.2
M2/AllBelow = -0.2
E2/AllBelow = -0.2
E1/AllBelow = -0.2
```

The valence-shell configurations employed in the AMBiT calculations for californium ions in charge states Cf^{12+} to Cf^{19+} are listed in Table A.2.1.

Charge state	Valence configuration
Cf^{12+}	6p2 6p+4
Cf^{13+}	6p1.67 6p+3.33
Cf^{14+}	6p1.33 6p+2.67
Cf^{15+}	6p1 6p+2
Cf^{16+}	6p0.67 6p+1.33
Cf^{17+}	6p0.33 6p+0.67
Cf^{18+}	6s2
Cf^{19+}	6s1

Table A.2.1: Valence shell configurations used in AMBiT calculations for californium ions in charge states Cf^{12+} to Cf^{19+}. Fractional occupation numbers are taken from relativistic shell calculations.

B Appendix

B.1 HD-EBIT pictures

Different views of the CAD model of the HD-EBIT injection system are shown here.

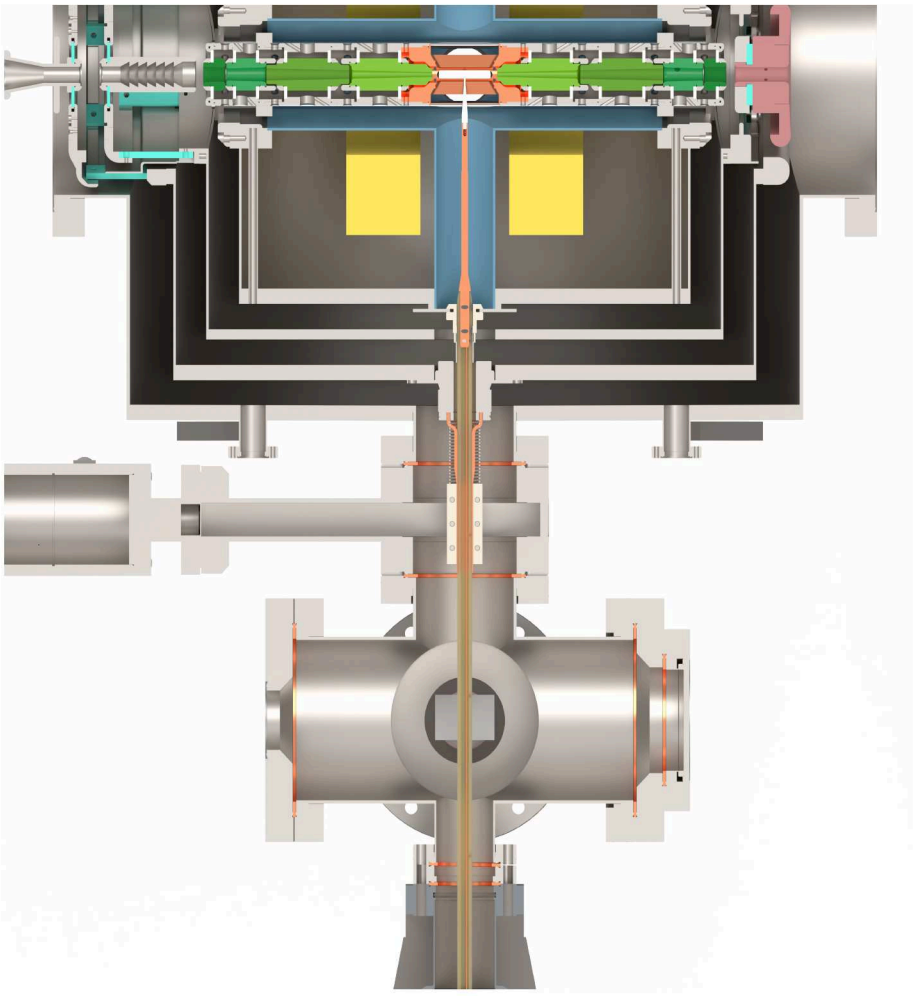

Figure B.1.1: Cross sectional view of the manipulator-target system

Figure B.1.2: Cross sectional view of the lens assembly in the HD-EBIT

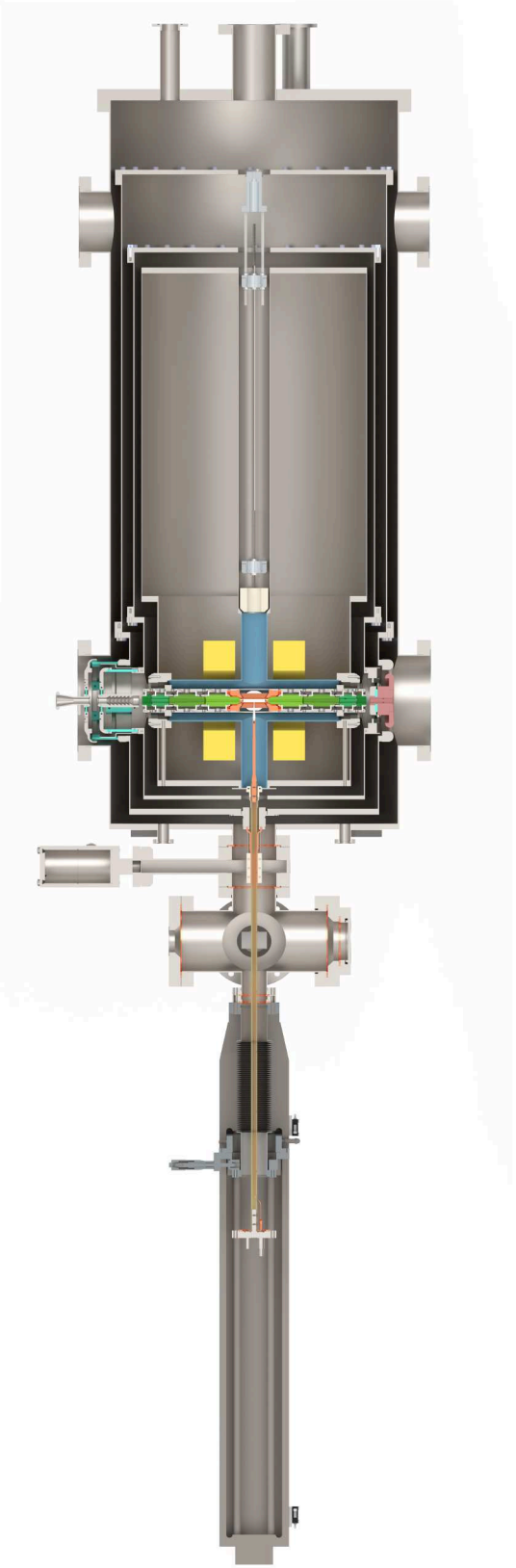

Figure B.1.3: HD-EBIT with the laser injection system

Selbstständigkeitserklärung

Ich erkläre, dass ich die Dissertation selbständig und nur unter Verwendung der von mir gemäß § 7 Abs. 3 der Promotionsordnung der Mathematisch-Naturwissenschaftlichen Fakultät, veröffentlicht im Amtlichen Mitteilungsblatt der Humboldt-Universität zu Berlin Nr. 42/2018 am 11.07.2018 angegebenen Hilfsmittel angefertigt habe. Für Übersetzungen ins Deutsche sowie für sprachliche und stilistische Überarbeitungen habe ich KI-basierte Werkzeuge genutzt.

Lakshmi Priya Kozhiparambil Sajith